

Development of metal oxide thin films as carrier selective contacts for silicon heterojunction solar cells

vorgelegt von

M.Sc.

Ganna Chistiakova

ORCID: 0000-0002-6391-3400

von der Fakultät IV – Elektrotechnik und Informatik
der Technischen Universität Berlin
zur Erlangung des akademischen Grades

Doktor der Naturwissenschaften

- Dr. rer. nat. -

genehmigte Dissertation

Promotionsausschuss:

Vorsitzender: Prof. Dr. Steve Albrecht

Gutachter: Prof. Dr. Klaus Lips

Prof. Dr. Uwe Rau

Prof. Dr. Bernd Rech

Tag der wissenschaftlichen Aussprache: 17.03.2020

Berlin 2020

Contents

1. Introduction	6
2. Materials, interfaces and devices	10
2.1 Materials	10
2.1.1 Amorphous silicon	10
2.1.2 Tin oxide	11
2.1.3 Magnesium oxide	13
2.2 Interfaces and devices	14
2.2.1 Heterojunction interfaces	14
2.2.2 Recombination	16
2.2.3 Solar cells	17
2.2.4 Silicon heterojunction solar cells	19
2.2.5 Si-based solar cells with dopant-free carrier-selective layers	22
3. Deposition methods and characterization	24
3.1 Sample preparation and layer deposition	24
3.1.1 Pre-treatments of samples	24
3.1.2 Plasma-enhanced chemical vapor deposition	24
3.1.3 Atomic layer deposition	25
3.1.4 Silicon heterojunction solar cells fabrication and IV measurements	29
3.2. Characterization	30
3.2.1 Photoelectron spectroscopy	30
3.2.1.1 X-ray photoelectron spectroscopy	30
3.2.1.2 Ultraviolet photoelectron spectroscopy	31
3.2.1.3 Determination of intermediate silicon oxide thickness	32
3.2.1.4 The band offset at heterojunctions	34
3.2.2 Surface photovoltage	35
3.2.3 Minority carrier lifetime measurements	36
3.2.4 Suns-Voc measurements	38
3.2.5 Photoluminescence measurements	39
3.2.6 Mercury probe measurements	39
3.2.7 Contact resistivity measurements	40

3.2.7.1. Transfer Length Method.....	40
3.2.7.2 Cox and Strack method	41
3.2.8 Spectroscopic ellipsometry	42
4. Tin oxide as an electron-selective contact	45
4.1 Introduction	45
4.2 SnO ₂ PEALD process optimization.....	46
4.2.1 Optimization of the oxygen plasma pulse step	46
4.2.2 Optimization of the plasma power	47
4.2.3 Influence of argon addition on the electrical and optical properties of SnO ₂ layers.....	48
4.3 Optical and electrical properties of SnO ₂ as a function of deposition temperature.....	50
4.3.1 Optical properties of PEALD SnO ₂ layers.....	50
4.3.2 Electrical properties of PEALD SnO ₂ layers	51
4.3.3 XPS analysis of SnO ₂ layers with varied deposition temperature	53
4.3.3.1 Evaluation of carbon and nitrogen signals	55
4.3.3.2 Evaluation of the oxygen signal	59
4.3.3.3 Evaluation of the tin signal and layer stoichiometry.....	60
4.4 Band offset between SnO ₂ layers and hydrogenated amorphous silicon	62
4.4.1 XPS analysis of SnO ₂ layers with increasing thickness.....	64
4.4.1.1 Si 2p analysis and intermediate oxide thickness estimation	64
4.4.1.2 Changes in main core level signals with increasing SnO ₂ layer thickness	66
4.4.2 UPS analysis of SnO ₂ layers	69
4.4.3 Band offset between SnO ₂ and n-aSi:H layers	71
4.5 Implementation of PEALD SnO ₂ layers in SHJ devices	75
4.6 Tin oxide layers for perovskite solar cells.....	77
4.6.1 Introduction.....	77
4.6.2 Oxygen plasma post-treatments for spin-coated SnO ₂ layers.....	79
4.7 Chapter summary.....	89
5. Magnesium oxide as a passivating electron-selective contact for silicon heterojunction solar cells	92
5.1 Introduction	92
5.2 Optimization of the ALD process and MgO layer properties	93
5.2.1 Optimization of the ALD cycle.....	93
5.2.2 Growth of MgO layers on c-Si and i-aSi:H/c-Si substrates.....	94

5.2.3 Changes in layer composition with air exposure	95
5.3 MgO layer thickness variation.....	97
5.3.1 Passivation properties	97
5.3.2 Contact resistivity of MgO layers	100
5.3.3 Devices with varying MgO thickness	102
5.4 Magnesium oxide layers at varied deposition temperatures.....	106
5.4.1 Dependence of MgO layers passivation quality on deposition temperature.....	106
5.4.2 XPS analysis of MgO layers deposited at different temperatures	108
5.4.3 SHJ solar cells with MgO layers at varied deposition temperatures.....	111
5.5 Magnesium oxide-metal contacts for silicon heterojunction solar cells.....	114
5.5.1 Comparison between Al and Ti-Ag metallization	114
5.5.2 Annealing of solar cells with different metallization.....	116
5.6 Chapter summary.....	119
6. Prospects and challenges for carrier-selective contacts for solar cells.....	122
6.1 Introduction	122
6.2 Carrier-selective contacts for SHJ solar cells	123
6.2.1 Silicon-based carrier-selective contacts	123
6.2.2 Metal oxide layers as electron-selective contacts	124
6.2.3 TMO layers as hole-selective contacts	125
6.3 Prospects for ALD for carrier-selective contacts	128
6.3.1 ALD for c-Si based solar cells	128
6.3.2 ALD for perovskite solar cells	129
7. Conclusions and outlook.....	133
8. Appendix	136
8.1 Abbreviations and symbols	136
8.2 Publications	138
8.3 Acknowledgments	140

Chapter 1

Introduction

In the last decades, global photovoltaic (PV) production has taken a huge step forward towards becoming competitive with conventional energy sources. At the beginning of 2019, the global PV installed capacity exceeded 500 GW, with an annual increase of around 100 GW [1]. Projections estimate that by 2022 the total installed capacity will surpass 1 TW [2]. However, despite such an optimistic prognosis, further reductions in the levelized cost of electricity (LCOE) are needed to ensure the achievement of such growth rate and to surpass it. Therefore, increase in cell efficiency and reduction in production costs are necessary.

Currently, 95 % of the global PV production is based on crystalline silicon (c-Si) [3], thus it can be regarded as the most relevant technology for further improvements in this field. In the development of c-Si solar cells, improving surface passivation and selective carrier extraction have become increasingly important topics and have proven to be key in achieving higher energy conversion efficiencies. For homojunction cells, which have carrier-selective contacts based on highly *p*- and *n*-doped Si regions, the implementation of surface passivation schemes has been pivotal in achieving higher efficiencies. A prime example is the introduction of Al₂O₃-based passivation layers at the rear side of the wafer in the passivated emitter and rear cell (PERC), which is now becoming the industry standard [4].

For silicon solar cells based on heterojunctions (SHJ solar cells), thin films provide not only surface passivation, but should also allow for selective extraction of carriers. A conventional heterojunction approach involves the deposition of an intrinsic hydrogenated amorphous silicon (i-aSi:H) passivation layer, followed by an *n*- or *p*-doped aSi:H layer for carrier selectivity. More recently, carrier-selective contacts based on a passivating ultrathin (~1.5 nm) SiO₂ layer followed by *n*- or *p*-doped poly-Si layers has been shown to yield excellent solar cell performance [5].

However, doped layers cause additional losses in the device, such as heavy parasitic absorption, which decreases the current of the solar cell, thus limits the efficiency. Therefore, besides these heterojunctions based on doped silicon layers, there has also been an increasing interest in dopant-free metal oxide layers, which feature higher transparency, while maintaining the

desired functionality of the doped layers, as carrier collection. Rather than on doping, these layers rely on induced band-bending with optimized valence- and conduction band offsets at the oxide/c-Si interface to achieve strong asymmetry in the carrier densities of holes and electrons, and thus in conductivity [6], [7]. This approach can have some potential benefits, such as the mentioned enhanced transparency and lower absorption losses, no need for dopants, and additionally ease-of-processing, as some of these selective layers do not require a dedicated passivation layer and can serve as passivation layers themselves (so-called passivating contacts) [8]. Although solar cells using dopant-free selective contacts have not yet reached the >25 % efficiency level of doped silicon layers [9], silicon-based solar cells with metal oxide layers have in a span of a few years already demonstrated efficiencies in excess of 22 % [10]. Additionally, further carrier-selective materials based on metal oxides (TiO_2 [10], Nb_2O_5 [11], MO_3 [12]), metal nitrides (TaN [13]) and metal fluorides (LiF [14]) are being developed for device applications. Further optimization and also further exploration of novel carrier-selective contacts therefore remains of importance to chart the potential of this dopant-free approach.

Within the development of these new materials, control over layer properties and layer thickness has become increasingly more important [15]. Additionally, layers should be deposited in a cost-effective way, which is scalable to high-volume manufacturing. Therefore, it is crucial to look not only at the material properties themselves, but to also consider deposition techniques that would be relevant to industry. Atomic layer deposition (ALD) can be a useful tool for depositing high quality layers. This deposition technique was adopted in the PV field relatively recently, initially in 2004 for the deposition of Al_2O_3 layers [16]. The main competing deposition technique is plasma enhanced chemical vapor deposition (PECVD), which has an advantage of being already widely implemented in industrial processes for a long time, where ALD has only recently started its growth for PV manufacturing. Therefore, for the further implementation of ALD in the industry, additional benefits should be provided. The main advantage of ALD for high quality devices is an excellent control over film properties, such as thickness homogeneity and doping level. Additionally, ALD processes can provide, in comparison to PECVD, more efficient precursor usage and low-temperature processing [17]. The decrease of precursor consumption would allow a significant reduction in operational costs.

The work presented in this thesis is focused on the investigation of metal oxide layers as electron-selective contacts for solar cells: tin oxide (SnO_2) in chapter 4 and magnesium oxide (MgO) in chapter 5 with ALD as a main deposition technique. These chapters discuss the process optimization, layer and interface properties of layers with subsequent implementation

in solar cell devices. Additionally, chapter 6 reviews the potential for dopant-free materials as carrier-selective contacts for silicon-based solar cells, and the potential of ALD as a way to deposit high quality carrier-selective layers for SHJ and perovskite solar cells.

Structure of this thesis

The first two chapters of this thesis contain the necessary theoretical and practical background for the following experimental results. Subsequent chapters present and discuss experimental results considering metal oxide layers (SnO_2 and MgO) as electron-selective contacts for SHJ solar cells. The final chapter presents a broader overview on carrier-selective contacts for Si-based solar cells. Furthermore, considerations for further development of ALD for c-Si based and for perovskite solar cells is presented.

Chapter 2 presents a brief summary of the materials, interfaces and device concepts used in this thesis.

Chapter 3 gives an overview of the deposition methods and characterization techniques used in this thesis.

Chapter 4 consists of three parts. The first part presents the plasma enhanced ALD (PEALD) process optimization for SnO_2 layers and correlates deposition parameters to opto-electrical properties of SnO_2 . This section is based on the publication [18]. The second part elaborates on the interface between SnO_2 layer and amorphous silicon, with increasing SnO_2 layer thickness, which allows monitoring the formation of an intermediate layer at the interface. The final section discusses SnO_2 as an electron-selective contact for perovskite solar cells. It presents and examines surface treatments for device improvement, based on the oxygen plasma treatment of spin-coated SnO_2 layers.

Chapter 5 encompasses the study of MgO layers as passivating electron-selective contacts for SHJ solar cells. The main focus of the chapter is the analysis of $\text{MgO}/\text{c-Si}$ and $\text{MgO}/\text{i-aSi:H}$ interfaces. The chapter also covers the dependence of solar cell performance on MgO layer thickness and deposition temperature. Additionally, it discusses possible metallization schemes at the interface to the MgO layer.

Chapter 6 presents a discussion on the possibilities and issues of implementing high work function transition metal oxide materials into c-Si based solar cells. Moreover, the results of the

thesis are put into a broader context via a general discussion of metal oxide layers used as carrier-selective contacts for SHJ solar cells. The final part of the chapter focuses on perspectives for ALD as a deposition method for carrier-selective layers for SHJ and perovskite solar cells.

The thesis closes with a discussion on the achieved results and a general outlook on future research of ALD for metal oxide layers, and for their implementation in SHJ solar cells in particular.

Chapter 2

Materials, interfaces and devices

2.1 Materials

2.1.1 Amorphous silicon

Hydrogenated amorphous silicon (aSi:H) is a disordered semiconductor, whose optoelectronic properties are governed by the large number of defects present in its structure. The main difference between the crystalline silicon (c-Si) and amorphous layers, is that c-Si, as a crystalline material, displays long-range order, while amorphous materials shows only short-range order [19], thus the random nature of the network determines the material properties. The main structural defects present in amorphous silicon are dangling bonds, which are created deep in the band gap. They arise, when some bonds are unsaturated in the amorphous network. In order to passivate these defects, hydrogen is introduced into the layer. This allows to fill microvoids [20] and to substitute weak Si-Si bonds, which constitute dangling bonds, with more stable Si-H bonds. Hydrogen can be incorporated in different configurations (SiH, SiH₂, and (SiH₂)_n) [21], [22], depending on the hydrogen content. The creation of SiH and SiH₂ bonds occur, when the hydrogen content is below 10 %, whereas the formation of ((SiH₂)_n) appears at higher concentrations [23]. Additionally, at hydrogen concentration above 14 %, layers contain microscopic voids that can be attributed to the formation of dihydride groups (SiH₂) [22]. However, not all hydrogen in the layer is atomically bonded to the Si-H bond and can be present as hydrogen molecules [24]. Undoped i-aSi:H layers provide excellent chemical passivation and favorable properties as heterojunction contact. Hydrogenation to a level of around 10% reduces the defect density by 4-5 orders of magnitude [25]. Additionally, by controlling the level of hydrogen in the layer, it is possible to increase the band gap [26]. The widening of the band gap with increased hydrogen content is induced due to a retreat of the valence band edge, while the conduction band remains relatively constant [27].

Undoped i-aSi:H layers present a high level of passivation. However, these layers have low doping densities and, thus, are poorly conductive. Therefore, in order to build a p-n junction, doping for layers has to be considered. In comparison to crystalline semiconductors, where atomic positions are well-defined, doping in amorphous semiconductors, due to the random

network, is more complicated. In the case of crystalline semiconductors, the dopant can either substitute an atom of the host lattice, or occupy a position not in the lattice, forming a defect. In the case of amorphous materials, there is no defined long-range order. Thus, dopants can create their own bonding configurations, while being part of the host atomic network. Generally speaking, the doping of amorphous silicon should be impossible by the 8-N rule for chemical bonding, by which each atom adopts the coordination that results in no occupied anti-bonding states, but with fully occupied bonding and lone pair states [19]. However, the possibility of doping has been shown experimentally [28]. The majority of dopant atoms, such as boron or phosphor, are, indeed, threefold coordinated and thus inactive. However, it is possible to have them fourfold coordinated [29], which allows to make a-Si:H electronically controllable [19]. Nonetheless, the efficiency of such doping is low. Doping becomes possible, due to the introduction of hydrogen in the layer. In not hydrogenated a-Si, the Fermi level cannot be moved by doping, due to the high density of defects. With the hydrogenation dangling bonds are passivated, and charged dangling bonds obey the 8-N rule, so are favored energetically [29]. Most of the excess charge carriers that are introduced by doping are trapped in compensating dangling-bond defects [30]. As a result of doping, the density of shallow defect states increases, which act as recombination centers, and thus the passivation of a-Si:H layers deteriorates. The n-doping is considered to be less detrimental in comparison to p-type, which introduces more structural defects and lowers the bandgap [31]. Additionally, in case of p type doping, exposure of the surface simultaneously to silane and diborane gases may cause the growth of highly defect-rich a-SiB_x:H layers [32]. Therefore, it is beneficial for high quality devices to consider dopant-free layers for p-n junction formation.

2.1.2 Tin oxide

Tin oxide (SnO₂) is a transparent wide-band gap n-type semiconductor that is used for a variety of different applications, such as sensors [33], lithium-ion batteries [34], oxidation catalysts [35] and photovoltaics [36]. It belongs to transparent conductive oxide materials, which combine high electrical conductivity with optical transparency [37]. However, the properties of SnO₂ layers strongly depend on stoichiometry, concentration of dopants and impurities, and microstructure.

Elemental tin forms oxides that can vary in stoichiometry, due to its cation dual valence: Sn²⁺ and Sn⁴⁺ that form stannic or stannous oxide [38]. SnO material is thermodynamically less

stable than SnO_2 and can exhibit p-type semiconductor behaviour [39]. Furthermore, it has a lower band gap ($\approx 2.5\text{-}2.8\text{ eV}$) in comparison to SnO_2 ($\approx 3\text{-}4\text{ eV}$) [38]. The main deposition method for SnO_2 layers in this thesis is ALD, which will be discussed in chapter 3. Therefore, it is important to understand, what is a dominant oxidation state is achievable with the deposition process. When tin is exposed to an oxygen source, the dominant deposited oxidation state is Sn^{4+} . However, if the oxidizer, or the tin precursor are not reactive enough to fully oxidize or to have full reaction at the surface, it is possible to have a combination of both oxidation states in the layer, or even dominant Sn^{2+} [40].

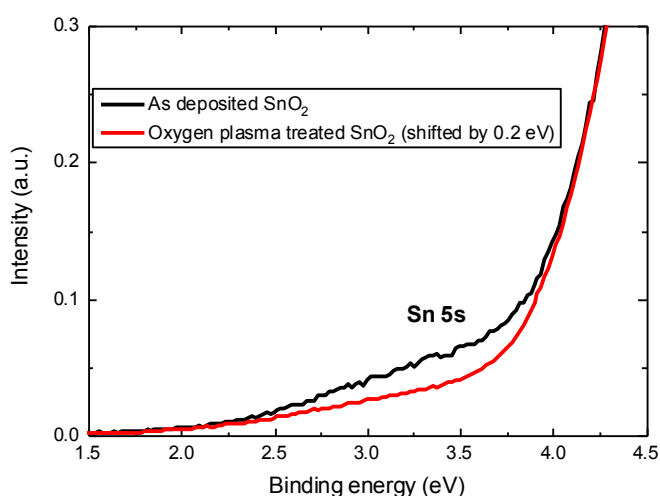


Figure 2.1: He I UPS spectra of spin-coated tin oxide after the satellite intensity extraction (see chapter 3.2.1.2), showing the valence band region vs. normalized intensity. Films were deposited on crystalline silicon wafers. Shown are curves for as-deposited films (in black) and oxygen plasma treated films (in red), with the latter shifted by 0.2 eV towards the Fermi level for better comparability.

In general, depending on the oxygen chemical potential of the system, the surface oxidation of SnO_x can reversibly transform from stoichiometric Sn^{4+} cations into reduced Sn^{2+} . The reduction of the surface modifies the surface electronic structure by forming Sn 5s derived surface states that lie deep within the band gap and cause the lowering of the work function [38]. These states can be detected by UPS measurements, as an additional signal intensity at a binding energy of 2-4 eV [41], [42], as is illustrated in fig. 2.1. However, it is possible to remove these surface states, e.g with an oxygen plasma treatment of the surface.

Furthermore, oxygen plays an important role for layer conductivity. Pure stannous oxide layers exhibit reduced conductivity. This is because the native defect in SnO₂ is a doubly ionizable oxygen vacancy, which is one of the main contributors to layer conductivity [43]. For non-stoichiometric layers, oxygen vacancies lie just 50 and 100-150 meV below the conduction band. Thus, at room temperature, charge carriers can be thermally excited from these states. Additionally, interstitial Sn, which has low formation energy, produces a donor level inside the conduction band, leading to instant donor ionization and conductivity [37]. Another important donor level at just 50 meV below conduction band, slightly deeper than the first oxygen vacancy level, can arise due to the presence of hydrogen [44]. The formation of this donor level occurs due to the diffusion of hydrogen in the layer, and interstitial hydrogen acts as a shallow mobile donor [45].

Additionally, tin oxide layers can be doped using a number of different elements. Tin cations can be substituted by Sb⁵⁺ or Ta⁵⁺. Otherwise, oxygen cations can be substituted by F⁻ [46] or Cl⁻. In photovoltaics, the most common usage of SnO₂ is in an alloy with InO_x to form indium-tin-oxide (ITO) [47], which is used in solar cells as a transparent conductive oxide (TCO) and anti-reflection layer. Pure SnO₂ can be used as a transparent conductive oxide itself, but is usually substituted with other materials, due to the lower charge carrier mobility and higher resistivity in comparison to other oxides, such as ITO or zinc oxide (ZnO) [48]. However, with the further development of perovskite solar cells, the usage of pure SnO₂ has recently become more prominent, due to its high transparency and suitable energy alignment with perovskites [49]. Therefore, SnO₂ can be used as an electron transport layer in perovskite solar cells [49]–[52], or in tandem devices like perovskite-silicon heterojunction solar cells [53], [54] In this thesis, SnO₂ layers are considered as part of the electron-selective contact for SHJ and perovskite solar cells.

2.1.3 Magnesium oxide

Magnesium oxide (MgO) is an ionic material, which is widely used in various applications, such as AC-plasma display panels [55], magnetic tunnel junctions [56], or as a passivation layer in various material systems. The main properties of magnesium oxide are its behaviour as a diffusion barrier, n-type conduction and wide bandgap, which, depending on the deposition method and temperature, is in the range of 4.5-8.9 eV [57].

In PV MgO was first used in dye-sensitized solar cells, as a barrier layer for SnO₂, in order to prevent interfacial charge recombination [58], [59]. In perovskite solar cells, it was implemented as a nanolayer coating for TiO₂ to block charge recombination at the TiO₂/CH₃NH₃PbI₃ interface. Recently, the successful implementation of MgO thin layers as stand-alone passivating electron transport layers for n-type c-Si wafers [12], [60], [61], and in alloy with aluminum oxide (Al_xMg_{1-x}O_y) as a passivation layer for p-type c-Si wafers has been shown [62].

In general, MgO layers show improvement in passivation and are stable towards high temperatures up to 300 °C in solar cells [60]. However, MgO layers have demonstrated chemical instability upon air exposure. It was shown that with air exposure, MgO films exhibit formation of -CO and CO₂ at defect sites. [63]. Additionally, it was reported that water molecularly adsorbs to the magnesium oxide surface, which leads to the formation of surface hydroxyl groups [64], [65]. The hydration reaction occurs at defect sites at the surface, but can also happen in the inner MgO film. The main factors affecting the hydration region are the density and grain sizes of the MgO layers [66].

2.2 Interfaces and devices

2.2.1 Heterojunction interfaces

A heterojunction interface is formed between two different semiconductors with unequal band gaps that are brought in contact [67]. Semiconductor heterojunctions can provide the asymmetry required for the effective separation and collection of photo-generated charge carriers. When carriers migrate across the junction interface, their movement is greatly affected by the junction barrier, which is determined by the band offsets and built-in potential (band bending) at the interface.

In fig. 2.2 schematic example of a heterojunction contact of two materials is shown. The energy band alignment at semiconductor interfaces is determined by the valence and conduction band discontinuities at the semiconductor hetero-interface, and by the Schottky barrier heights at semiconductor/metal interfaces. Small barriers enable charge transport across the interface and are a prerequisite for Ohmic contacts [68], which would ensure a minimized voltage drop across the interface. Therefore, the main task, while forming such, is to achieve proper band alignment

for corresponding carrier transport between the materials, which largely determines the functionality of the final devices [69].

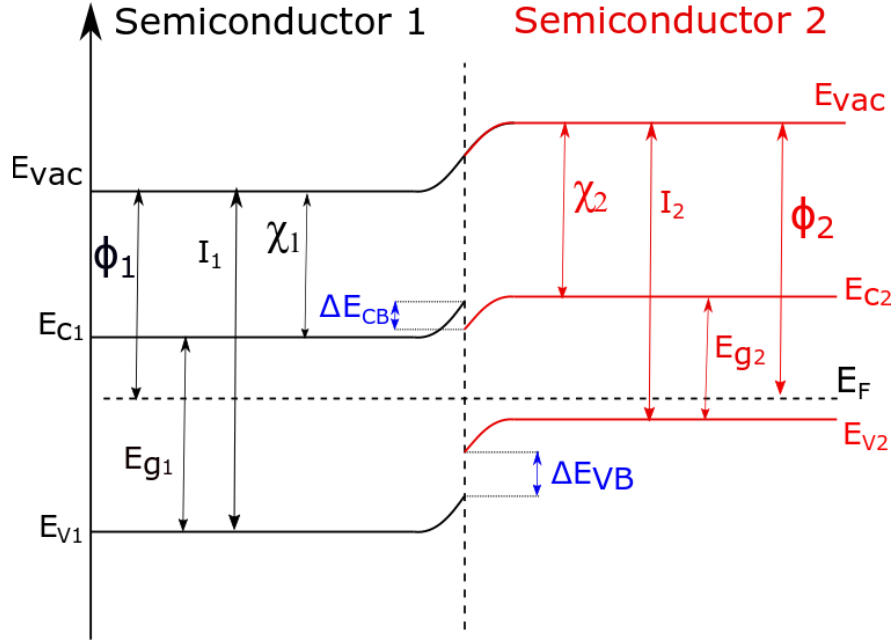


Figure 2.2: Two different semiconductors in a hetero-contact, E_{vi} – valence band, E_{ci} – conduction band, E_F – Fermi level, E_{gi} – bandgap, E_{vac} – vacuum level, ϕ_i – work function, I_i – ionization potential, χ_i – electron affinity.

The simplest approach (Schockley-Anderson model) to assess the band alignment is by using the ionization potentials (I) and electron affinities (χ) for the offset assessment:

$$\Delta E_{CB} = \chi_2 - \chi_1 \quad (2.1)$$

$$\Delta E_{VB} = I_2 - I_1 \quad (2.2)$$

Any change in doping of the semiconductor will change the band bending, but not the band offsets (barrier heights), if electron affinity and bandgap are not functions of doping [70]. The electron affinity is strongly influenced by surface dipoles, which are given by the local atomic structure and charge distribution at the surface. Thus, such approach can be valid only if the changes in the dipoles at the interface are equal for both semiconductors [71]. Another widely used model was derived by Tersoff, which suggests the interface dipole associated with gap states induced by band discontinuities is the dominant factor in determining band line-up. Any

difference in the work functions of two materials results in charge transfer, hence a dipole. This dipole depends on the band offset and tends to drive the band lineup towards the value that corresponds to zero dipole. The equilibrium occurs, when the midgap energy of both materials characteristic for the bulk, lines up. Thus, the offset can be assumed from the difference of the midgap energy [72], [73]. The further models are based on the concept of charge transfer due to the tunneling of the bulk mass electrons into each side across the junction interface. A stationary dipole is induced by the net charge transfer from the material with the higher valence band into the material with lower [74]. For more polar bonded semiconductors the density of interface states is lower, which results in a lower Fermi level pinning [68].

In addition to the induced states, extrinsic interface states can influence the band alignment of the two semiconductors. These states can arise from defect formation, or interface contamination. The states and bulk properties of the material can be modified by post-treatments of the interface, such as annealing [75] or plasma treatment [76].

2.2.2 Recombination

Recombination is a process that leads to the elimination of excited charge carriers. Therefore, recombination properties of semiconductors strongly affect their electrical performance and, thus, recombination rate is an important characteristic for any semiconductor device, including solar cells. It is possible to classify the different types of recombination as being of intrinsic or extrinsic origin [77].

Intrinsic recombination is present even in the ideal, undisturbed crystal. Two fundamental intrinsic recombination processes can be distinguished: radiative and Auger recombination. Radiative recombination occurs, when an electron in the conduction band recombines with a hole in the valence band and the excess energy is shed by emitting a photon with an energy approximately equal to that of the bandgap. Such recombination is most pronounced for direct-bandgap materials. However, due to silicon being an indirect-bandgap semiconductor, the probability of such recombination for silicon-based devices is low, in comparison to other recombination processes. This occurs due to the necessity to have the simultaneous emission of a photon and phonon in order to conserve both momentum and energy. Thus, the involvement of the third particle in the recombination process decreases the probability of radiative recombination. Auger recombination occurs, if the excess energy is transferred to a third charge

carrier, which releases it as phonons to the crystal. The Auger lifetime is proportional to the inverse square of the carrier density, and at high injection levels, it is the dominant mode of recombination in silicon.

For cases of extrinsic recombination, the electron-hole recombination occurs via defect center in the bandgap (Shockley-Read-Hall (SRH) recombination) [67]. It can be represented as a two-step capture mechanism, whereby the free electron from the conduction band and a free hole from the valence band are annihilating each other in the defect level. This type of recombination can occur either through bulk defects, induced by impurities or dislocations, or at surface states.

The different recombination processes occur in the parallel to each other and the total recombination rate in semiconductor is the sum of all the rates, each of which is characterized by a lifetime, which can be divided into surface and bulk lifetimes [67]:

$$\frac{1}{\tau_{eff}} = \frac{\Delta n}{R(\Delta n, n_0)} = \left(\frac{1}{\tau_{SRH}} + \frac{1}{\tau_{Auger}} + \frac{1}{\tau_{rad}} \right) + \frac{1}{\tau_{surface}} = \frac{1}{\tau_{bulk}} + \frac{1}{\tau_{surface}} \quad (2.3)$$

This parameter is valuable for estimating solar cell performance. At low injection level, when the equilibrium majority charge carriers outnumber the light generated excess carriers, SRH is dominant recombination. At high injection level, excess carrier outnumber equilibrium majority charge carriers, Auger recombination is dominant.

2.2.3 Solar cells

Simplistically, a solar cell can be thought as a diode under illumination. The basic silicon solar cell consists of a silicon absorber layer and doped layers of the opposite polarity. Under incident illumination, light-generated carriers are separated, according to their polarity and then being collected at the appropriate contact.

In a simple equivalent circuit a solar cell can be represented as a diode, with an external photocurrent j_{ph} , the series (R_s) and parallel (R_p) resistances. These resistances represent the ohmic losses within the device. R_s arises from the resistance of the layers and contacts to current flow. R_p (shunt resistance) represents current paths bypassing the p-n junction in the form of shunts between the two contacts. The major part of shunt resistance can be assigned to leakage currents at the edges of a solar cell. The IV curve of such circuit can be described as:

$$j(V) = j_0 \left(\exp\left(\frac{q(V - jR_s)}{mkT}\right) - 1 \right) + \frac{V - jR_s}{R_p} - j_{ph}, \quad (2.4)$$

Where j_0 is the reverse bias saturation current, q is the elementary charge, V is external voltage, m is the ideality factor that accounts for the deviation from the ideal diode equation where $m = 1$, k is the Boltzmann constant and T is the temperature [78]. When assuming the real device, where recombination is governed by different mechanisms that do not necessarily obey this relation, parameters j_0 and m are needed to be adjusted accordingly.

The IV curve for solar cell can be characterized by using four parameters:

The short circuit current density (J_{sc}) is the current through the solar cell per unit area, when the voltage across the cell is zero. For an ideal solar cell with zero series resistance, the short circuit current is equal to the photogenerated current. The practical limit for a c-Si based single junction solar cell under standard illumination conditions, 1-sun illumination (AM 1.5G) at 25 °C is 43.7 mA/cm² [79]. The main decrease in J_{sc} in the device can be attributed to the reflection, parasitic absorption and recombination losses at the contact, or during the lateral carrier transport [80].

Another important parameter is the open circuit voltage (V_{oc}), which is the voltage generated by the illuminated diode at open circuit conditions. The maximum V_{oc} can be achieved, when recombination rates throughout the cell are minimized and can be described as a measure of the amount of the recombination in a device. Auger recombination is the main recombination mechanism for silicon, thus is the main limitation for V_{oc} in c-Si based solar cell devices [81].

The next one is fill factor (FF), which is calculated as:

$$FF = \frac{V_{MPP}J_{MPP}}{V_{OC}J_{sc}}, \quad (2.5)$$

where V_{MPP} and J_{MPP} are the voltage and current density at the maximum power point, which corresponds to the highest power output. The FF is a measure for the transport and recombination losses, thus it is highly impacted by both R_s and R_p resistances. High R_s and low R_p reduce the fill factor of the device and their optimization is one of the main challenges of the solar cell development. For a heterojunction solar cell, the presence of the hetero-interface itself can be regarded as a barrier for photo-generated carriers. In n-type absorber SHJ cells a large valence band offset at the a-Si:H/c-Si interface can result in a field effect, which improves the passivation, and thus increases the V_{oc} . On the other hand, this offset limits carrier collection and reduces the FF of the solar cell [82]. In the case of mismatched interfaces in a solar cell, where transport barrier can form, making it possible to observe an s-shaped IV curve for the device [83].

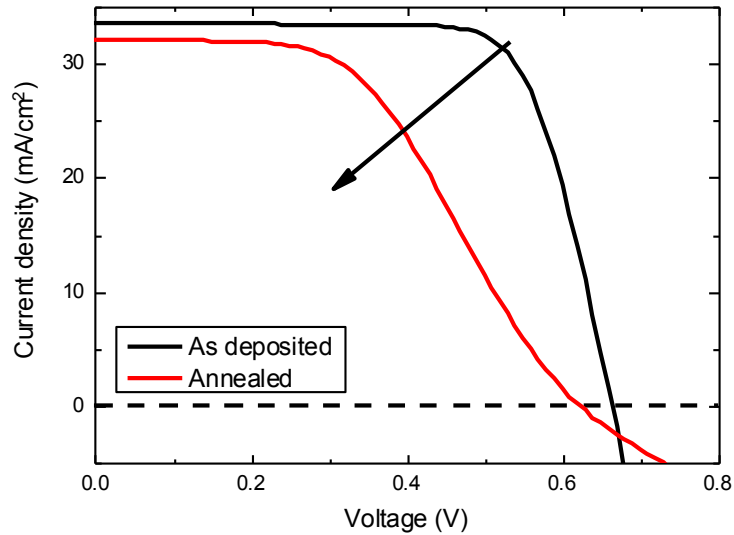


Figure 2.3: Illuminated IV curves for SHJ solar cell with MgO layer as electron-selective contact measured on a deposited device, and after 3 minutes annealing at 150 °C.

As an example, fig 2.3 shows the IV curve of the SHJ solar cell with MgO layer, as electron-selective contact for as-deposited and annealed device. It can be seen that after the annealing step the shape of the IV curve became s-shaped, which leads to drastically decreased FF and V_{OC} . Mitigation of the s-shape can be achieved by using different work function materials [84], by doping the contact materials, or by decreasing the thickness of the passivating buffer layers. FF is strongly dependent on V_{OC} , therefore, the FF should be estimated while including V_{OC} as a parameter. The maximum achievable FF of 89% can be accomplished with at V_{OC} of 769 mV [85].

The final important parameter for the device analysis is the efficiency of the solar cell, which is calculated by dividing the power output by power of the incident light. From the calculations for the limiting efficiency of the solar cell, the maximum estimated theoretical efficiency that can be achieved for a single junction solar cell is of 29.43% for a 110 μm thick wafer [79].

2.2.4 Silicon heterojunction solar cells

Most reported silicon heterojunction solar cells are based on n-type c-Si wafers as absorbers. This is due to their lower sensitivity towards impurities, which results in superior charge carrier lifetimes, in comparison to p-type wafers [86], [87]. SHJ solar cells include thin intrinsic

amorphous silicon layers and p-n junction formed by the deposition of the following corresponding doped layers: p-aSi:H as a hole contact (minority carrier contact) and n-aSi:H as an electron contact (majority carrier contact). SHJ cells with assuming n-type c-Si wafer as an absorber, can be built in a front junction configuration, with the hole-selective contact at the front side of the solar cell absorber, or as a rear side junction device, with the electron-selective contact at the front side and hole-selective contact at the rear. Both configurations function well in SHJ solar cells. The most widely used configuration is the front side emitter. In this case, minority charge carriers are generated close to their collecting contact, which enables higher short circuit current density. However, for high charge-carrier lifetime absorbers, minority charge carriers can efficiently reach the collecting contact, regardless of the hole contact position [88]. Therefore, excellent passivation is one of the main prerequisites for high quality devices. Thus, a thin layer of i-aSi:H is added on top of the c-Si substrate to passivate the wafer surface. The i-aSi:H/c-Si interface is crucial for both sides of the c-Si wafer and has to be atomically sharp, without epitaxial growth. By inserting an i-aSi:H layer, the interface recombination velocity can be decreased, and further increase in V_{OC} can be achieved [89]. Therefore, in order to achieve high V_{OC} , the insertion of i-aSi:H layers for passivation is crucial. However, the conductivity of i-aSi:H layers is very low, and parasitic optical absorption increases with layer thickness. Therefore, with thick i-aSi:H layer, J_{sc} and fill factor of the solar cell are reduced, and s-shaped IV curves are often observed [90]. Consequently, the layer thickness should be as thin as possible, but thick enough to provide sufficient surface passivation. Similarly, the thickness of the p-aSi:H layer should be as low as possible in order to reduce parasitic optical absorption, but at the same time thick enough to enable the proper formation of the p-n junction[47], [91].

Additionally, the main issue with p-aSi:H layers is their comparatively low conductivity. Therefore to provide lateral conductivity, on top of the p-aSi:H layer an additional transparent conductive oxide (TCO) layer is deposited, commonly ITO [92]. Additionally, this layer serves as an anti-reflection layer. At the rear side, an additional TCO layer is deposited on top of n-aSi:H layer to reduce contact resistance and to enhance the optical response, by suppressing plasmonic absorption that would occur at the metal contact [93].

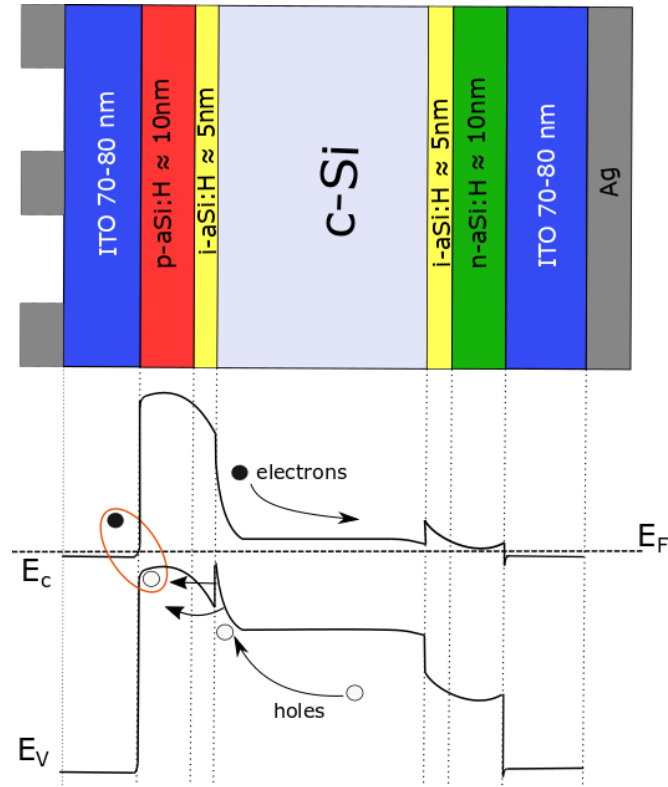


Figure 2.4: The top part represents the schematic structure of a front-side emitter SHJ solar cell. Light comes from the left (yellow arrow). The bottom part shows the band line-up of this cell. Top solid lines are conduction band (E_c), bottom solid lines are valence band (E_v). The dashed line is the Fermi energy (E_F). The direction of the carrier flow is shown with arrows. The tunnel recombination at the p-aSi:H/ITO interface is marked in orange.

The SHJ solar cell is completed by the deposition of metal contacts. The front side is contacted by a grid, and the back side can be fully metalized, or also contacted by a grid to form a bifacial solar cell [94]. A schematic representation of a SHJ solar cell and its band diagram is presented in fig. 2.4. Carrier excitation happens mainly in the c-Si wafer. Electrons diffuse through rear side i-aSi:H, n-aSi:H and TCO layers and are afterwards collected at the metal contact. The highest barrier on this path for electrons is created by the conduction band offset between i-aSi:H and c-Si substrate, which is approximately 0.2-0.3 eV [27], thus can be overcome by thermionic emission. Similarly, holes diffuse to the front side through i-aSi:H and p-aSi:H layers. However, the main difference here is that the p-aSi:H/TCO interface includes a tunnel-recombination contact [91]. The mismatch in band alignment at this interface limits the current extraction of the solar cell and leads to the creation of the depletion region, which reduces the band bending in the a-Si:H/c-Si heterojunction and this decreasing the field passivation. Thus,

it can lead to the decrease of the V_{OC} and FF of the solar cell. Therefore, proper interface engineering is required [84].

2.2.5 Si-based solar cells with dopant-free carrier-selective layers

Fundamentally, there are two key parameters for highly efficient solar cells: efficient carrier-selective contacts and excellent surface passivation. The main goal for a good carrier contact is to selectively block the flow of either electrons via conduction band barriers, or holes via valence band offsets, and at the same time allow the other type of carrier to pass through. Therefore, for further device improvements, there is a need to be able to maintain a low band offset for the corresponding carrier, while simultaneously reducing the optical absorption, in the contact layers. Unfortunately, doped amorphous silicon layers do not give such flexibility, due to the doping limitations and thickness restrictions mentioned before. Therefore, there is a need to substitute these layers with alternatives. One way is to use passivating contacts, such as metal oxide layers.

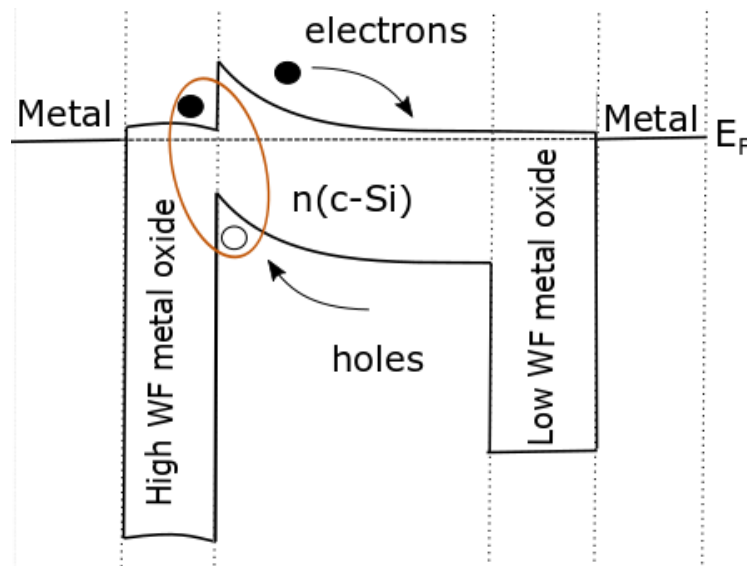


Figure 2.5: Schematic band lineup for silicon solar cell with metal oxide layers as carrier-selective contacts. The tunnel recombination at the c-Si/ high work function material interface is marked in orange.

In this case, suitable electron affinity and band gap of the material are especially important for the band alignment with the silicon wafer. For the minority carrier contact, transition metal oxide materials with higher work function than the ionization energy of c-Si, such as WO_3 [95], or MO_3 [96], can be considered. In this case, a large conduction band offset is formed, leading to a strong inversion layer with an accumulation of holes, despite these semiconductors being n-type. Materials with low work function which are lower or close to the electron affinity of c-Si, such as titanium oxide (TiO_2), are suitable as electron selective contact, due to a low conduction band offset [97]. A simplified band lineup of such solar cell device with metal oxides, as carrier-selective contacts is presented in fig. 2.5. The use of these undoped alternatives to amorphous silicon enables the fabrication process of SHJ solar cells to be more robust and cost-effective. However, such an approach also demands higher attention to the interfaces of these layers with either TCOs or metals, in order to prevent the formation of Schottky barrier.

Chapter 3

Deposition methods and characterization

3.1 Sample preparation and layer deposition

3.1.1 Pre-treatments of samples

In this thesis, polished n-type c-Si wafers, float zone, with <100> surface orientation, resistivity of $\sim 1\text{-}5\ \Omega\text{cm}$, and $280\ \mu\text{m}$ thickness were used as substrates. Prior to the depositions, wafers were cleaned with a standard process developed by Radio Company of America (RCA) [98]. This cleaning procedure involves two baths containing ammonium hydroxide and hydrogen peroxide in the first one, and hydrochloric acid with hydrogen peroxide in the second one. The first bath leads to the formation of a thin silicon dioxide layer with incorporating and etching organic residues and surface particles. The second bath removes metallic contaminants and forms a thin silicon dioxide layer. After this cleaning, samples are dipped in 1% HF for 2 minutes in order to remove the wet-chemical oxide grown on the surface. Flat wafers were used in order to make it more accessible for measurement techniques like ellipsometry, where surface quality is important for further analysis. Additionally, such wafers were used for the fabrication of solar cell devices. While textured wafers would produce higher cell efficiencies, devices on flat wafers simplify the production process and have better reproducibility. Therefore, the sources of experimental errors can be decreased.

Corning glass substrates were used for resistivity and optical measurements on SnO_2 layers. Prior to the deposition processes, they were cleaned with the alkaline cleaner.

3.1.2 Plasma-enhanced chemical vapor deposition

Plasma-enhanced chemical vapor deposition (PECVD) is the most common deposition method for the fabrication of aSi:H layers. In this thesis, all aSi:H layers were produced in AltaCVD parallel-plate PECVD reactors from Altatech with 13.56 MHz frequency, RF power source for plasma excitation. During the PECVD process, a plasma discharge is created, which ionizes molecules and atoms of gases in the chamber. Afterwards, the dissociation products are transported on heated substrates and form a layer [25]. For the deposition of i-aSi:H layers, a

mix of Silane (SiH_4), as the silicon precursor, and Hydrogen (H_2) is used. Depending on the ratio between these gases, layer properties can differ drastically [23]. The best passivation quality can be achieved in the transition from amorphous to nano-crystalline [99] state, while avoiding epitaxial growth, which is detrimental to passivation [100]. Therefore, the amount of hydrogen during the layer deposition should be limited. However, as was discussed in chapter 2.1, hydrogen at the c-Si interface plays a crucial role for passivation quality of i-aSi:H layers. Thus, the post-deposition inclusion of hydrogen through a plasma treatment can be beneficial for layer quality [101], [102]. By optimizing plasma parameters, it is possible to achieve an improved passivation quality for i-aSi:H layers. For doped layers, the addition of precursor gases of diborane (B_2H_6) for p-aSi:H layers, or phosphine (PH_3) for n-aSi:H layers during the deposition process is needed. The standard deposition parameters for the different a-Si:H layers in this thesis are described in table 3.1.

Layer	SiH_4 (sccm)	H_2 (sccm)	Dopant gas (sccm)	Pressure (mbar)	Temperature (°C)	Power (mW/cm²)
<i>i-aSi:H</i>	13	7	0	0.8	185	45
<i>n-aSi:H</i>	15	40	4 (PH_3)	2	210	100
<i>p-aSi:H</i>	33	25	18 (B_2H_6)	2.5	142	50
<i>Hydrogen plasma post- treatment</i>	0	30	0	1.25	185	75

Table 3.1: Main PECVD parameters for the various aSi:H layers and for the hydrogen plasma post-treatment of the i-aSi:H layers.

3.1.3 Atomic layer deposition

Atomic layer deposition (ALD) is a surface-limited thin film deposition technique, which is similar to a CVD process. However, contrary to CVD, gas phase precursors are not applied simultaneously in the process, but by the exposure of the substrate surface to the precursors in alternating exposure steps. Consequently, the sample surface is exposed to only one precursor at a time, and no gas phase reactions between precursors can occur. Each surface reaction during the process occurs between a gas-phase reactant and a surface functional group [103]. These reactions stop, when all available surface groups have reacted. Each of these steps has to be

optimized to exclude sub-saturated growth, or growth with a parasitic CVD growth component within too short precursor or purge steps [104].

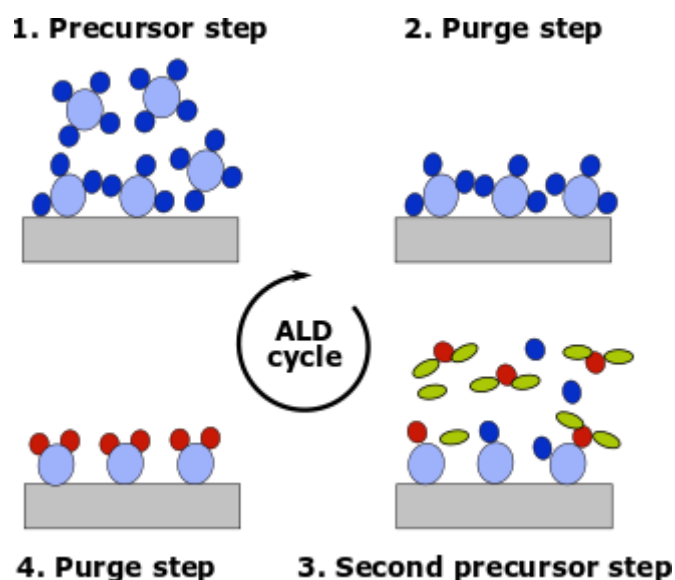


Figure 3.1: A schematic representation of ALD cycle consisting of two half reactions. The exposure in the first half cycle (Step 1) of precursor and in the second half cycle (Step 3) of co-reactant are self-limiting and process stops, when all available surface site are saturated. Steps 2 and 4 are purge steps that are required between half-cycles to remove unreacted precursor.

Each ALD cycle involves two reactants with the following sequence, as shown in fig. 3.1: 1) Self-terminating reaction of the first precursor, 2) a purge step to remove unreacted precursor and volatile reaction by-products, 3) self-terminating reaction of the second precursor through new surface groups, 4) another purge step. The cycle is then repeated, until the desired layer thickness is achieved [105].

Therefore, a standard ALD process consists of reaction cycles, each of which results in a constant increase in film thickness. Thus, the deposition rate is usually referred to as growth per cycle (GPC) [106]. For an ideal ALD process, with known GPC, the film thickness can be controlled precisely through the number of deposition cycles.

Depending on the precursor, with ALD it is possible to grow a wide range of materials, such as oxides, nitrides, sulfides, or pure metals [107]. This deposition technique produces high quality layers with accurate thickness control. The important factor is to have a suitable precursor-

surface chemistry: the ALD reactants must adsorb to the surface, and the adsorption has to be irreversible and self-terminating [103], [108]. In order to have surface reactions, the presence of reactive surface sites is required, such as -OH groups for oxides [105]. Otherwise, no binding to the surface can occur. Therefore, the initial substrate surface state can lead to the delayed or absent nucleation and film growth.

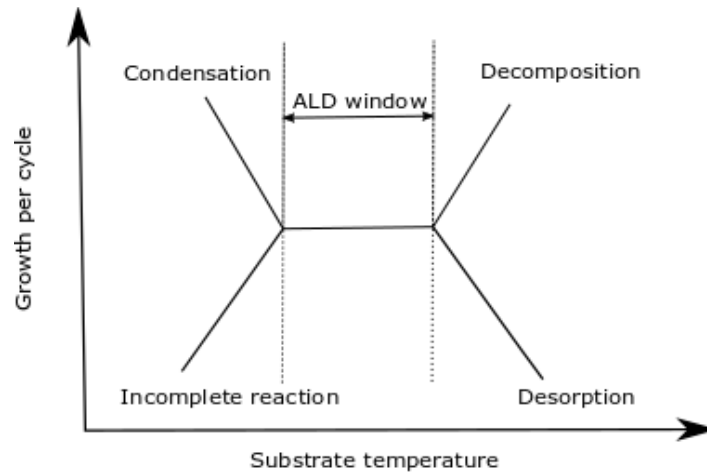


Figure 3.2: schematic representation of possible layer growth behaviour during ALD with varying substrate temperature [107].

Another important parameter for high quality ALD processes is the deposition temperature. The region of temperatures, where an ALD process can be described as ideal is called the “temperature window” [106]. This concept is applicable to most ALD processes [109]. However, there are also exceptions with no well-defined range of temperatures with a constant GPC [110]. A schematic representation of the effects of temperature on ALD processes is shown in fig. 3.2. Outside the temperature window, the growth per cycle changes significantly. At lower temperature, reactants can condense on the surface, or the surface reactants may not have enough energy to complete the reaction. At higher temperature, the surface species can decompose and allow additional reactant adsorption, which can resemble the behaviour of CVD with increased surface reactions that are no longer self-limiting. Otherwise, if the film material is volatile, it may evaporate, which would lead to a decreased GPC.

ALD is defined by chemical reactions, so there is always a risk of residues left from the precursors. The impurity contents of the film bulk and its surface strongly depend on the

completeness of the reactions [111]. Due to this, ALD layer properties can strongly vary compared to same material layers deposited by other techniques, such as physical vapor deposition (PVD) or PECVD.

The main focus of this work is on metal oxide layer growth by ALD. For oxide layers, the second precursor is an oxidizing agent (water, hydrogen peroxide, ozone, or oxygen plasma). Depending on the oxidizer, the deposition process and layer properties can differ drastically. In this thesis, the following ALD processes are investigated: SnO₂ layer deposition with oxygen plasma as an oxidizer, and MgO layer deposition with water as an oxidizer. Both types of ALD processes are briefly described below.

ALD processes involving non-plasma oxidizing sources, are usually referred to as thermal ALD. Water is commonly used for thermal ALD processes, and works well as an oxidizer. Moreover, water-based ALD can be considered a “soft” deposition process, as there is no damage at the substrate surface during the oxidation step. However, there are several drawbacks for such deposition. Firstly, the process has to include long purge times, due to the slow desorption of excess water [112], which drastically increases the total deposition time. Secondly, water reactivity is reduced with decreasing deposition temperature. Therefore, at lower temperatures water is not reactive enough to remove ligands from the surface, limiting the GPC or exhibiting absence of the layer growth [113].

The other possibility is to use oxygen plasma as an oxidizer, so called plasma enhanced atomic layer deposition (PEALD). During the PEALD process, the reactive species are created in the gas-phase, which causes a higher reactivity with the surface [114]. This can also lead to shorter nucleation times [115] and higher GPC, in comparison to water-based ALD [116]. Additionally, the process requires lower deposition temperatures, therefore allowing a higher degree of freedom when choosing substrates, or precursors. In this thesis, a remote plasma source (RPS) is used for the PEALD process. The RPS is located away from the substrate stage, such that the substrate is not affected in the generation of the plasma species. This permits separate tuning of the substrate and plasma parameters, while having high reactivity with low ion energies [117]. Therefore, such deposition processes are flexible and produce high quality layers at higher deposition rates than for thermal ALD processes. Additionally, the utilization of plasma allows a higher flexibility in tuning the process, due to a higher number of tunable deposition parameters, such as plasma power [118], plasma exposure time [119], or the addition of gases during the plasma step [120]. However, PEALD has its own drawbacks that have to be

considered. During the plasma step, the deposition surface is exposed to reactive species from the plasma that can induce undesired reactions, leading to surface contamination and poor uniformity of the film. Another issue is plasma damage that can promote the formation of defects in the material, or at the surface [114], [121]. Plasma-induced damage can be partially or fully mitigated by tuning the deposition parameters, such as gas pressure, or plasma power [122].

3.1.4 Silicon heterojunction solar cells fabrication and IV measurements

The general structure of SHJ solar cells was already described in section 2.2.4. Devices built for this thesis have a front junction configuration, with hole-selective contact at the front. The deposition of aSi:H layers is described in section 3.1. Additionally, TCO layers and metal contacts were deposited on all devices. ITO, which was deposited by physical vapor deposition (PVD) at 50 °C deposition temperature, was utilized as the TCO layer at the front and rear side of the solar cell. The required thickness of ITO is 75-80 nm, which was optimized, in order to get the best electrical and optical output from the device [47]. The front side ITO was deposited through a shadow mask to define a solar cell area of 1 cm². Each wafer contained 3-6 solar cells. After the sputtering step, samples were annealed for 5 minutes at 200 °C to remove sputter damage and to crystallize the ITO layers [123]. Metallization was done by thermal evaporation. The front grid consisted of a metal stack of 10 nm titanium and 1500 nm silver (Ti-Ag) and was defined by using a shadow mask. The back contact consisted of a blanket layer of 10 nm titanium and 500 nm silver for the standard SHJ solar cells.

In order to determine parameters of the final device, IV measurements were performed at a solar simulator. These measurements were carried out at Wavelabs Sinus-70 Class AAA sun simulator that simulates the terrestrial solar spectrum AM 1.5G. The simulator was calibrated using calibrated silicon reference diode. During the measurements, the samples were maintained at a temperature of 25 °C and fully masked, except the measured cell area.

3.2. Characterization

3.2.1 Photoelectron spectroscopy

3.2.1.1 X-ray photoelectron spectroscopy

X-ray photoelectron spectroscopy (XPS) is a powerful technique, which allows to extract surface and bulk information, such as type, chemical state and concentration of elements with a penetration depth of 1-10 nm [124]–[126], depending on the material. As an example, fig 3.3 shows the survey spectra for thin SnO₂ layer (2 nm) deposited on top of n-aSi:H substrate. In this case it is possible to get information not only about the SnO₂ overlayer material, but also about n-aSi:H substrate.

The technique involves irradiating the sample with soft X-rays and analyzing the energy of detected outgoing electrons. X-rays interact with atoms in material and cause electrons to be emitted via the photoelectric effect. The kinetic energy of these electrons is measured. Afterwards, this value can be converted to the binding energy by using the formula:

$$E_k = h\nu - E_b - \Phi, \quad (3.1)$$

where $h\nu$ is the energy of the incident photon, E_b is the binding energy of the atomic orbital, from which the emitted electron originates, and Φ is the work function of the spectrometer, which is an instrument parameter. The latter is obtained by setting the Fermi edge emission of a clean metallic sample to zero binding energy.

Because of unique sets of binding energies for different elements, it is possible to identify the type, chemical state and concentration of elements in the measured depth of the material [127]. Depending on the X-ray source and measured material, it is possible to identify the species present in the material in the range of 0.1-1% [128]. Additionally, it is feasible to get valuable information from the shifts in binding energy. These chemical shifts arise from the differences in the chemical potential and polarizability of the compounds.

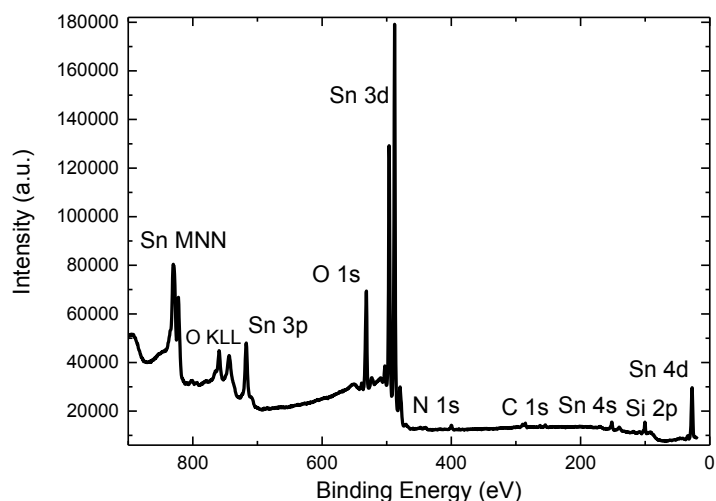


Figure 3.3: XPS survey of a 2 nm SnO₂ layer deposited on top of an n-aSi:H layer on c-Si substrate.

In this work, a non-monochromatized Al K_α (1486.6 eV) and Mg K_α (1253.6 eV) sources are used for global survey measurements. For region specific measurements Mg K_α source is used, due to its higher resolution [125] in comparison to Al K_α. Analysis of the XPS elemental core level spectra was conducted using the software fityk [129]. The fitting of the each spectra region was done, using Voigt profiles with full-width-half-maximum (FWHM) coupled to the same value and with the inclusion of a linear background, all of which were fitted simultaneously. The Voigt function incorporates the convolution of Gaussian and Lorentzian functions in the lineshape of the curve. The Gaussian component simulates peak broadening due to experimental origins. The Lorentzian component describes broadening from the transitional principle. Number of employed fit peaks was minimized, additional peaks for region fitting were only used, if a physical reason is could be invoked, such as the presence of other chemical species.

3.2.1.2 Ultraviolet photoelectron spectroscopy

The main difference between XPS and ultraviolet photoelectron spectroscopy (UPS) is the excitation energy. UV radiation is provided by inertial high purity gas, such as neon, or helium discharge. This gas discharge produces a number of emission lines with different intensities. In this work, the He I line with an energy of 21.2 eV is used. Due to the low excitation energy, it

is feasible to detect only valence electron states. This measurement technique is very surface-sensitive and is used in this thesis to determine valence band edges, and to measure the secondary electron cutoff to determine the work function.

The valence band edge was extracted from a linear fit of the leading edge of the spectrum [130] after subtracting the He I β -excited replica of the spectrum, which produced the satellite shift of 1.87 eV and relative intensity of 1.2 %. Afterwards, calculated values are converted to the binding energy, using formula 3.1. The secondary electron cutoff region was measured with the applied bias voltage of 10 V and was fitted using a Boltzmann-Sigmoid function in order to determine the work function [131] with extracted afterwards value for bias voltage. The example measurements and fits for He I-UPS spectra are shown in fig. 3.4.

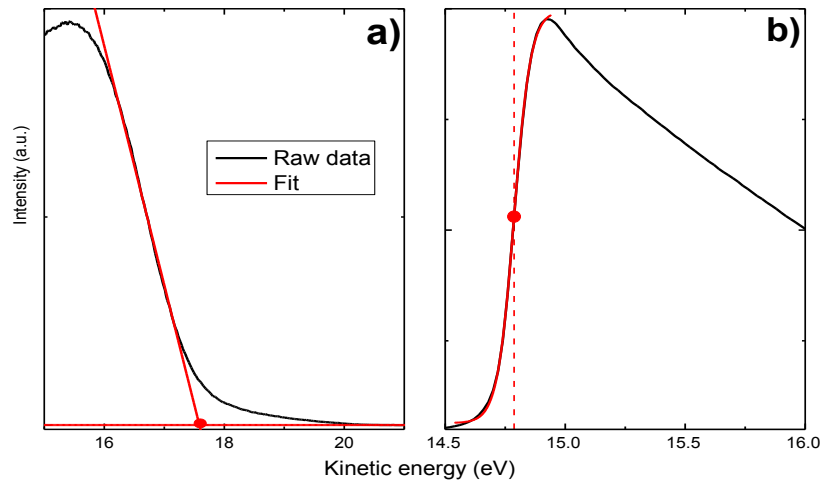


Figure 3.4: Raw data and example fit of He I-UPS spectra for SnO₂ layer: a) valence band edge fitting using linear fit, b) secondary cutoff region fit, using the center point of Sigmoid-Boltzmann function.

3.2.1.3 Determination of intermediate silicon oxide thickness

The interface between silicon and a metal oxide is crucial for the solar cell device. Thus, it is important to understand the changes that occur at the interface upon the metal oxide layer deposition. One of the important issues is the exposure of silicon surface to oxygen, or metal oxide itself. This can lead towards oxidation of the silicon surface itself, if the resulting negative Gibbs formation energy is lower for Si, than for considered metal. Therefore, intermediate SiO_x

layer can be formed at the interface. Depending on metal oxide and deposition method, the thickness of this intermediate layer can be up to 3 nm [132]. The band gap of SiO₂ layers is ~ 9 eV [133], which means that by depositing a metal oxide layer, the additional dielectric barrier is created. This barrier, by possibly being highly defective and not stoichiometric, or thicker than the threshold for charge carrier tunneling (~ 2 nm) [134], can lead to the degradation of the solar cell performance. Therefore, by analyzing interface and device performance, it is important to have an idea of not only about the structure of this layer, but also to be able to estimate its thickness.

With XPS it is possible to not only identify chemical bonds at the surface and in the material's bulk, but to also evaluate the thickness of a thin layer on a substrate. Unfortunately, XPS is powerful for qualitative analysis, but not so precise, when it comes to quantification of species in absolute values. There are a lot parameters that influence precision, from the type of measured materials themselves to the tool parameters, such as the transmission function of the spectrometer, or the efficiency of the detector. These uncertainties can give an accuracy of up to 10% by trying to quantify the presence of species in the absolute values [135]. Despite this, it is still important to have an estimate for the intermediate SiO_x layer thickness, which is formed between the silicon substrate and metal oxides (SnO₂ in this thesis). Oxide thickness can be determined from the formula [136]:

$$d_{oxide} = L_{SiO_2} \cos\theta \ln\left(1 + \frac{R_{expt}}{R_0}\right), \quad (3.2)$$

where L_{SiO_2} is the attenuation length for Si 2p photoelectrons in the pure SiO₂ overlayer, θ is the angle of emission of photoelectrons relative to the surface normal, R_{expt} is the measured ratio between the intensity of the substrate and oxide, and R_0 indicates the relative intensities of pure silicon oxide on top of silicon. Both of these factors can be extracted from the Si 2p core level. In the case of formation of understoichiometric SiO_x at silicon surface, all five chemical states of silicon, which include four oxidation states and Si⁰ have to be taken into account, when calculating the thickness of SiO_x [136], and R_{expt} can be calculated as:

$$R_{expt} = \frac{(I_{SiO_2} + 0.75I_{Si_2O_3} + 0.5I_{SiO} + 0.25I_{Si_2O})}{(I_{Si} + 0.75I_{Si_2O} + 0.5I_{SiO} + 0.25I_{Si_2O_3})}, \quad (3.3)$$

where $I_{Si_xO_y}$ are intensities of the corresponding chemical states of silicon.

3.2.1.4 The band offset at heterojunctions

By combining XPS and UPS measurements, it is feasible to determine the offset for the heterojunction system by the method derived by Kraut [137], [138]. Near to the interface, the local charge-density distribution may differ from the bulk. It can be assumed that the bandgap does not change from the bulk to the interface, thus varying electrostatic potential which bends all energy level depends only on the distance from the interface. In general, valence band offset between the over layer and the bulk can be described, as:

$$\Delta E_v = E_v^{over} - E_v^{sub} - qV_{BB}^{over} + qV_{BB}^{sub} \quad (3.4)$$

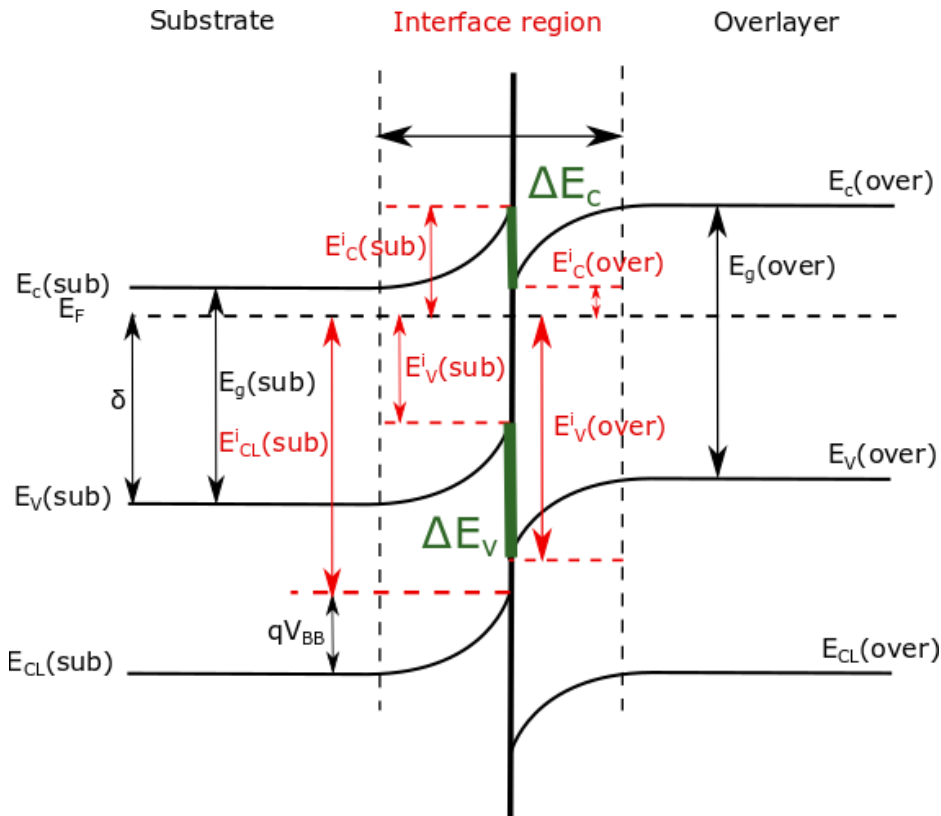


Figure 3.5: Generalized energy-band diagram of an semiconductor-semiconductor interface [137], [138], E_v is the valence-band maximum, E_{CL} is the energy of core level, E_C is the conduction band minimum, E_g the bandgap of the material and δ is the position of the Fermi level in the bulk relative to E_v .

Fig. 3.5 shows the representation of the interface between two semiconductors. It is possible to estimate the band bending potential at the interface as:

$$qV_{BB} = (E_{CL}(b) - E_v(b)) + \delta - E_{CL}(i) \quad (3.5)$$

Consequently, when shifting to the interface between two materials with an overlayer thin enough to observe the XPS signal of the substrate, it is possible to determine the valence band offset only by XPS and UPS measurements:

$$\Delta E_v = (E_{CL}^{Over} - E_V^{Over}) - (E_{CL}^{Sub} - E_V^{Sub}) - (E_{CL}^{Over}(i) - E_V^{Sub}(i)) \quad (3.6)$$

The effect of interface states is to shift the potential within the sampled region on both sides of an interface. Thus, any potential shift, due to interface states or other sources of band bending cancel [138]. Therefore, it is feasible to estimate the offset independently of potential variations across the interface, such as band bending, or electric fields.

3.2.2 Surface photovoltage

The Surface photovoltage (SPV) is the illumination-induced change in the surface potential [139]. SPV measurement technique is an efficient tool to measure surface band bending [140] at the heterojunction, or to obtain a qualitative estimate of the surface passivation [141]. The SPV setup, used in this thesis, was developed at HZB [27].

The setup configuration can be represented metal-insulator-semiconductor contact. This structure consists of TCO layer as a front contact, which is deposited on quartz window and thick mica foil that insulates sample from the TCO. On top of the foil the top electrode is located that enables capacity measurement. The back side of the sample is grounded, or bias voltage can be applied, depending on the measurement. The basic principle is to measure the surface potential before and after a short light pulse, which in this case is produced by laser pulse with wavelength of 905 nm. The light pulse is directed through the top electrode to the sample surface. The sample structure consists of a c-Si substrate and a semiconductor layer on top. The pulse with the chosen wavelength would prevent strong absorption in the most coatings on top of c-Si substrate. Thus, the photogeneration takes place in the c-Si substrate, which leads to a splitting of the Fermi level into the quasi-Fermi levels for electrons and holes [142]. Additionally, the homogenizer and system of lenses is used to make the laser beam as homogeneous as possible in the active area. The variation in surface potential measured as a photovoltage pulse corresponds to a change in band bending at the substrate/semiconductor interface and is extracted after a correction for the Dember voltage resulting from the difference in mobility's of electrons and holes [27]. If the illumination intensity is high enough that the

conduction and valence band will flatten at the surface right after the excitation, thus the system is in a steady state condition. Therefore, the maximum value of Dember-corrected SPV after the light pulse directly corresponds to the dark band bending in c-Si.

3.2.3 Minority carrier lifetime measurements

A widely applied experimental method to measure injection-dependent carrier lifetimes in samples is from measurements of transient and quasi-steady state photoconductance (TRPCD and QSSPC, respectively). In this thesis, a WCT-100 setup from Sinton Consulting was used [143]. The setup consists of a photographic flash lamp, as a generation source of free charge carriers in the sample. The sample is inductively coupled at the back side by a coil to a radio-frequency bridge, which detects changes in the permeability of the sample and therefore its conductance. The TRPCD mode uses a short illumination pulse that is rapidly turned off. Afterwards, the decay of excess carrier density over time is determined without illumination [77]. This approach is commonly used to measure high carrier lifetimes, if the flash decay time is a few orders of the magnitude shorter than the carrier lifetime. In the case of low lifetimes, where the effective lifetime of the sample is comparable to the duration of the light flash, the QSSPC mode is used. In this case, the illumination is slowly reduced to zero over several milliseconds [143]. Therefore, the decay is slow enough to ensure that the sample is in a steady state in terms of recombination.

Samples for such type of measurement need to be symmetrically processed. The requirement is necessarily due to PCD method being sensitive towards all recombination in the sample, which means that the bulk of the sample has to be high quality to be able to exclude its influence. Thus, the opposite side has to be passivated as well, such that the investigated surface is the limiting one. Additionally, samples require absence of the metal coverage, in order to have inductive coupling.

The described measurement technique allows to obtain minority carrier lifetime curves as a function of excess carrier density. A widely applied evaluation is to compare the effective lifetime data at a certain excess carrier concentration, usually at 10^{15} cm^{-3} , or to calculate the implied V_{OC} (iV_{OC}) directly from the data. iV_{OC} is equal to the splitting of the electron and hole-quasi-Fermi level and indicates the maximum achievable V_{OC} for a structure. Another important output result that can be calculated from lifetime measurements is the implied JV curve based

on passivation properties and assumed photogenerated current density. From this curve it is possible to determine the implied fill factor (iFF). This parameter does not include series resistive losses and represents the limit for the achievable FF of the device on provided passivation quality [144].

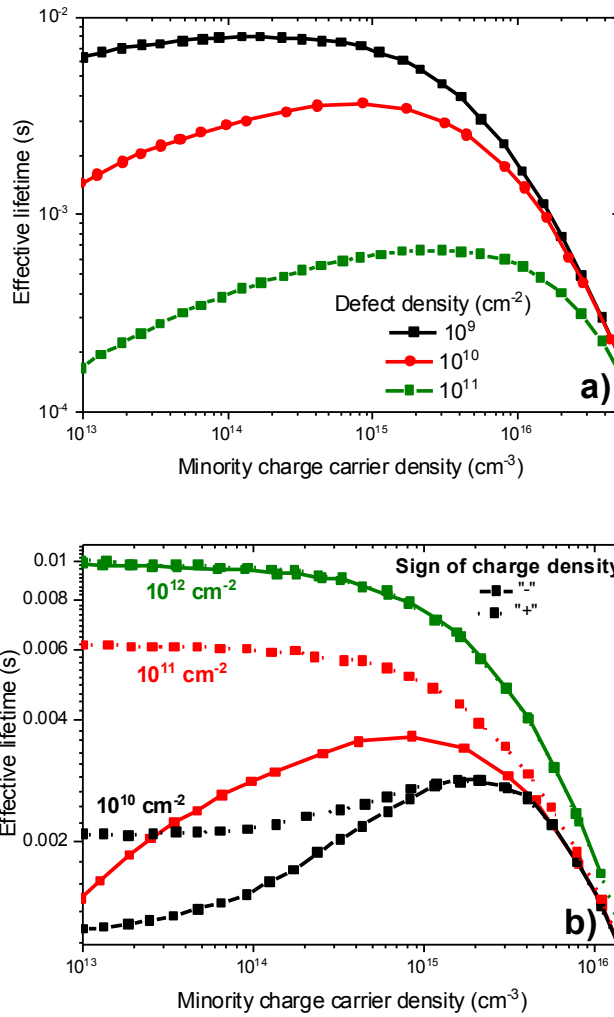


Figure. 3.6: modelled injection-dependent curves for the effective lifetime for a-Si:H/c-Si structure a) for varying D_{it} with the Q_i fixed at -10^{11} cm^{-2} , b) for varying Q_i with the D_{it} fixed at 10^{10} cm^{-2} .

A more advanced assessment of the data requires theoretical models [145]. The recombination velocity at the interface is determined by the defect density (D_{it}) and by the carrier concentration at the interface (Q_i). By applying a semi-analytical model developed by Leendertz [146], [147],

it is feasible to deduce both of these parameters at the interface. This model is using D_{it} and Q_i as the fitting parameters. The Q_i determines the field-effect passivation. At the same time, D_{it} determines the defect passivation. The model is fitting both these parameters in the whole range of the experimental data of the obtained lifetime curve, using the sum of the residuals squared as a norm [147].

In fig. 3.6 a,b the variation of the simulated with the model lifetime curve shapes, while fixing D_{it} or Q_i , is shown. Depending on the features of the lifetime curve, it is possible to discern between D_{it} and Q_i . D_{it} shifts the curve upwards or downwards, while maintaining the shape of the curve (fig 3.6 a). At the same time, changes in fixed charge density have a strong impact on the curve shape, influencing carrier lifetimes mostly at low excess carrier density, since field effect passivation (due to high Q_i) is only effective in low injection (fig 3.6 b).

3.2.4 Suns-Voc measurements

The V_{OC} of the solar cell strongly depends on the illumination intensity. The Suns-Voc method involves measurement of the V_{OC} of the solar cell at monotonically varying illumination from a flash lamp. Assuming the superposition principle, an implied IV curve one-sun (AM 1.5G) illumination can be constructed from the measured data. By measuring the solar cell at V_{OC} conditions at different incident light intensities, it is possible to exclude series and shunt resistance related losses [148]. Therefore, it is feasible by comparison of measured current-voltage curve for the device at one-sun (AM 1.5G) illumination and pseudo curve calculated from Suns-Voc measurements to extract series resistance of the solar cell as:

$$R_s = \frac{\Delta V}{J_{mpp}}, \quad (3.7)$$

where ΔV is the voltage difference between both pseudo and measured curves at the maximum power point, which is divided by the current density at this point [149].

Therefore, this measurement is a valuable method for estimating the series resistance of the device, if the IV curve of the solar cell device is not limited by an S-shape, which is caused by non-linear transport barriers. In this thesis, Suns-Voc measurements were done at the Suns-Voc accessory station to the WCT-100 lifetime tool from Sinton Consulting.

3.2.5 Photoluminescence measurements

Photoluminescence (PL) imaging is a fast and convenient optical technique to get an overview of the spatial distribution of the minority carrier lifetime in the sample. In this technique, the passivated wafer is excited by a light source with an energy greater than the wafer's bandgap to generate charge carriers. These charge carriers can then recombine radiatively and produce luminescence, which can be detected by the camera. Intensity of the emitted light relates to the passivation quality of the investigated sample, where areas with low intensity correspond to increased amount of defects and SRH recombination. The setup used in this thesis includes a silicon CCD camera and an optical filter that blocks wavelengths below 800 nm, which allows ideally only the PL signal from silicon to pass through. However, the measured PL signal strongly depends on the optical properties of the sample. Additionally, it is not possible to differentiate between bulk and surface recombination. Therefore, in order, to make a quantitative conclusion about the lifetime, calibration is needed in order to know the absolute emission [150]. The PL data presented in this thesis does not have calibration, thus the obtained results are discussed only from a qualitative point of view. All investigated samples were produced on high quality float c-Si wafer, which allows to exclude the influence of the bulk, thus PL intensity changes are caused by the surface passivation. Samples with different material stacks were not compared between each other, due to the different optical properties. However, by measuring samples with the same optical properties, it is possible to estimate the changes in the surface passivation.

3.2.6 Mercury probe measurements

Mercury probe measurements are fast and convenient way to estimate the resistivity of thin and not highly conductive layers, but in which resistivity is too high to measure with the standard four-point probe. This method involves the contacting of the investigated layer with a mercury drop defined area electrode under the vacuum and IV curve is measured [151]. Films for these measurements were deposited on top of dielectric materials (corning glass substrates). Additionally, film thickness was measured via ellipsometry, in order to compute the resistivity of the investigated layers [152]. For conductive materials this method gives values similar to those obtained, with a standard four-point probe. Therefore, it can be used for a wide-range of materials.

3.2.7 Contact resistivity measurements

Contact resistivity is one of the important parameters for contact characterization and optimization. Depending on the contact resistance value, it is possible to determine the eventual existence of transport barriers at the contact. For low values, below $100 \text{ m}\Omega\text{cm}^2$, no drastic influence on device efficiency for c-Si based devices can be observed. However, with increasing contact resistivity, the losses at the contact are no longer negligible. If contact resistivity exceeds values of around $250 \text{ m}\Omega\text{cm}^2$, the additional loss of V_{oc} , due to the contact, is around 10 mV [7]. The specific contact resistivity can be defined as the product of contact resistance (R_c) and contact area A . It is derived from the R_c [153], and includes various parasitic contributions, depending on the measurement method of R_c [154]. The most common techniques for contact resistivity measurement are the Transfer Length Method (TLM) and the Cox and Strack method (CSM).

3.2.7.1. Transfer Length Method

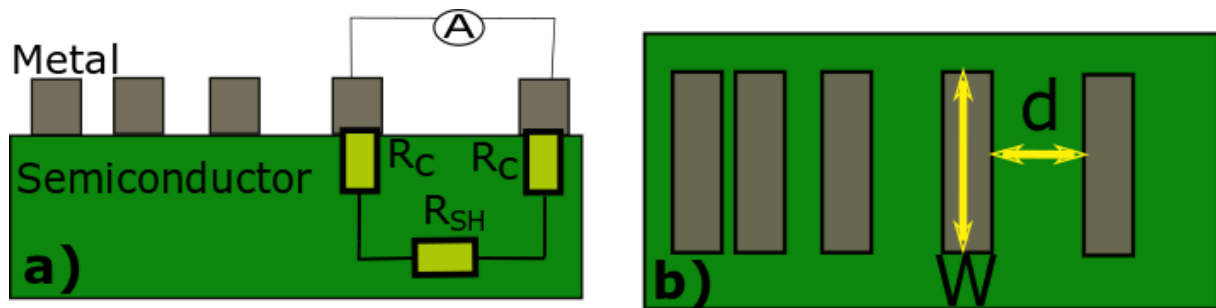


Figure 3.7: a schematic a) side, b) top view of the TLM structure.

TLM allows to determine the contact resistivity at the contact and to separate the contact resistivity from the semiconductor sheet resistance of the layer beneath the contact [155]. The basic sample structure, as shown in fig. 3.7 a,b, is an array of the metal stripes of width W and length l , deposited on top of another conductive material. These stripes should have the same width and length, but differ in their spacing distance. Current-voltage measurements are then performed on adjacent stripes at each distance. The total resistance R_T between two contacts is

afterwards plotted as a function of the distance between the stripes, which is a linear equation. It is possible to extract contact and sheet resistance R_c and R_{SH} accordingly:

$$R_T = 2R_c + \left(\frac{R_{SH}}{W}\right)d \quad (3.8)$$

By taking into the account the geometry of the stripes, it is feasible to obtain the contact resistivity ρ_c through transfer length parameter L_T , which is the intersection of the total resistance function at $R_T = 0$, divided by two and can be calculated as [156]:

$$L_T = \sqrt{\frac{\rho_c}{R_{SH}}} \quad (3.9)$$

Hence, ρ_c can be calculated, as

$$\rho_c = R_c L_T \frac{1}{\coth(l/L_T)} \quad (3.10)$$

3.2.7.2 Cox and Strack method

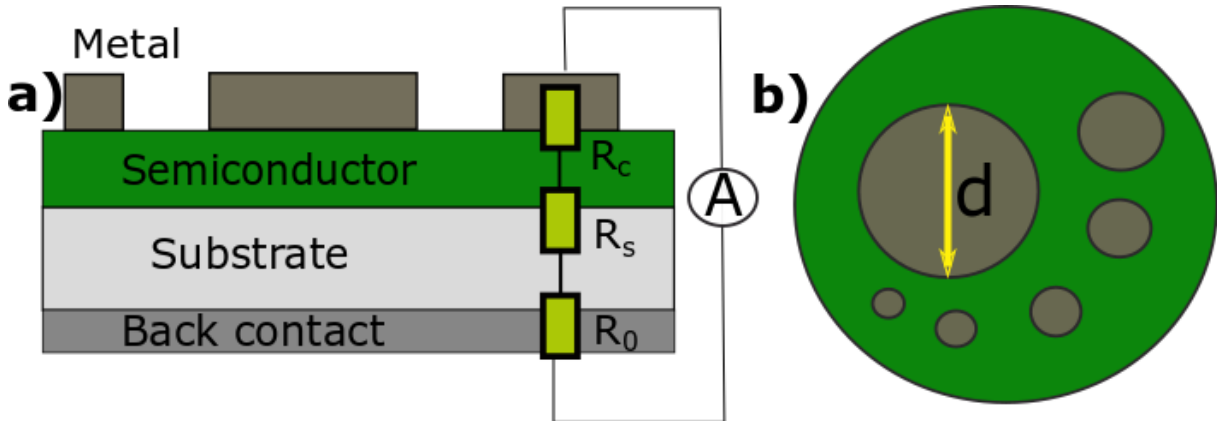


Figure 3.8: a schematic a) side, b) top view of a test structure for the Cox & Strack method.

The TLM is suitable for investigating moderately conductive materials. However, due to the inclusion of lateral resistance in the total output, it is difficult to estimate contact resistivity for the lowly conductive materials. Therefore, a different test structure is needed. One of the most common ways to extract contact resistivity for lowly conductive materials is the Cox & Strack method (CSM) [157]. The schematic structure for CSM is shown in fig.3.8. The top of the structure consists of an array of circular pads with varying diameters deposited on top of

investigated material. The current-voltage output is measured through the whole structure at different pads, hence, so a back contact to the substrate is required. In this thesis, Ti-Ag metallization is used at the rear side, which forms an Ohmic contact with the silicon wafer, used as a substrate. The total measured resistance can then be plotted as a function of the pad area, where d is the diameter of the pad:

$$R_T = R_s + R_c + R_0 = \frac{\rho}{d\pi} \arctan \frac{4}{d/t} + \frac{4R_c}{\pi d^2} + R_0, \quad (3.11)$$

where the first part describes the spreading resistance R_s , in which ρ and t are layer resistivity and thickness, respectively. The second term denotes the specific contact resistance, which includes the interface and bulk resistances. Furthermore, R_0 denotes the back side resistance and is independent of the contact diameter.

3.2.8 Spectroscopic ellipsometry

Ellipsometry is a non-destructive measurement technique for obtaining optical properties of materials by probing with an obliquely reflected or transmitted light beam. Ellipsometry is most commonly used in reflection mode for the determination of film thickness and optical constants over a wide photon energy range. The main working principle of the technique is that linearly polarized light incident at an oblique angle to a surface changes polarization state when it is reflected, and that this change in polarization is strongly sensitive to dispersion and interference effects [158]. The polarization change is determined for a set of wavelengths in a certain photon energy range, usually by using a CCD array or scanning monochromator. The main ellipsometric parameters are the amplitude ratio ψ between incoming and outgoing beam and their phase angle Δ . These parameters are related to the Fresnel amplitude reflection coefficients for light polarized parallel and perpendicularly to the plane of incidence, ρ_π and ρ_σ , respectively. These are themselves strongly dependent on the complex refractive index of the material. These parameters can be described as:

$$\frac{\rho_\pi}{\rho_\sigma} = \tan\psi e^{i\Delta} \quad (3.12)$$

In order to get information for the specific layer, such layer thickness, it is necessary to fit appropriate dispersion models for the complex refractive index to the data. In this thesis, the following models are used [159]:

1. Tauc-Lorentz oscillator. It combines Tauc's model for the absorption edge of amorphous semiconductors with a Lorentz oscillator for high energy absorption. Thus, it considers the bandgap of the material as the absorption onset and three oscillator parameters (center value, width and oscillator strength). This model was used for the description of amorphous silicon layers.
2. Drude-Lorentz oscillator. It is based on Drude's classical AC conductivity model and describes the optical absorption due to free charge carriers. When bound charge carriers are considered, it is known as the Lorentz oscillator model, which can describe absorption bands in metals. This model was used in conjunction with Tauc-Lorentz to describe TCOs, such as tin oxide, or ITO.
3. Cauchy dispersion model. It is an approximation of a Lorentz oscillator, which is used for transparent materials. The model consists of three Cauchy parameters, which describe the dispersion of the refractive index. This model is used for the description of MgO layers, which have wide bandgaps and are thus transparent in the entire measured range.

In this thesis, all ellipsometry measurements were performed in the wavelength range of 190-850 nm. Additionally, all ex-situ measurements were performed under three different incident angles (50, 60, 70 °) for increased accuracy.

In this thesis, in-situ ellipsometry is used for growth monitoring during the PEALD process of tin oxide layers. This is a powerful tool for layer analysis during the deposition process, which is especially valuable during the first cycles. Generally, ellipsometry is sensitive to changes in the nominal thickness of the layer down to 0.01 monolayer [160]. Therefore, this is a robust tool to monitor the thickness changes during the ALD process. The incidence angle for these measurements was fixed at 70 °.

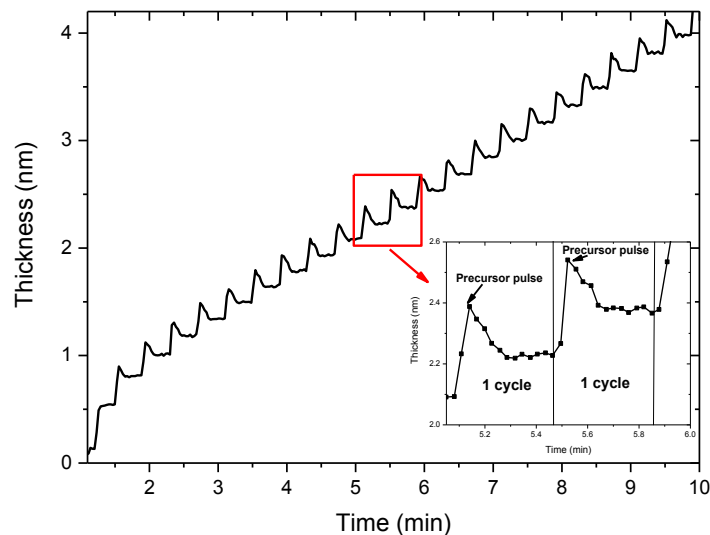


Figure 3.9. Thickness of PEALD SnO₂ vs. the deposition time. The data extracted from in-situ ellipsometry measurement. The inset graph shows at detailed view of the thickness variation over a cycle time scale.

An example of layer thickness evolution by time, using in-situ ellipsometry measurements for the first deposition cycles of SnO₂ is shown in fig. 3.9. From these measurements, it is possible to obtain the following information [160]:

1. The nucleation behaviour, by observing the delay in layer growth, or the increased growth during the first cycle. This can indicate the formation of a layer with different morphology, or composition, which can be an intermediate oxide.
2. By monitoring thickness, as a function of deposition time, it is feasible to obtain the growth per cycle and saturation curves in a quick and with reduced material use. The amount of cycles needed for higher precision is dependent on the measurement time, in order to decrease signal/noise ratio.
3. From measurements during different stages of the deposition cycle, it is possible to distinguish sub-monolayer changes. As can be seen from the fig. 3.9, after the precursor step the measured thickness is higher than at the end of the cycle. This can be related to chemisorption of the precursor for SnO₂ and corresponds to changes in refractive index. However, within the model all layer parameters fixed, thus the change in the thickness is observed. After the plasma step the organic surface groups are removed [161], which corresponds to a decrease in the thickness.

Chapter 4

Tin oxide as an electron-selective contact

4.1 Introduction

The following chapter outlines the optimization process of PEALD SnO₂ layers and provides an analysis of the interface between n-aSi:H and SnO₂, as a function of SnO₂ layer thickness. Due to SnO₂ being an n-type semiconductor [38], it can be combined with n-aSi:H layers to form an electron selective contact, as a bilayer, or it is conceivable to deposit it on an undoped passivation layer as a stand-alone electron-selective contact. Thus, it is important to investigate this interface. Additionally, this chapter presents the post-treatment of spin-coated SnO₂ layers for the perovskite solar cells with a focus on properties of the layer surface and interface to the perovskite layer.

The first section of this chapter focuses on an investigation of the optical and electrical properties of PEALD SnO₂ layers, depending on the process parameters. These properties are then related to chemical information gathered from in-system photoelectron spectroscopy. Three main parameters were varied for each optimization series: deposition temperature, oxygen step duration and oxygen plasma power. This part of the chapter is based on the publication in Ref. [18].

The second section of this chapter discusses how the interface between n-aSi:H and SnO₂ changes with increasing SnO₂ layer thickness, which is controlled by the number of PEALD cycles. In-system ultraviolet photoelectron spectroscopy and X-ray photoelectron spectroscopy measurements were used to monitor shifts in the core levels and the valence band edge positions in the silicon substrate and in the SnO₂ film. Additionally, spectroscopic ellipsometry was used to extract the band gaps of both the SnO₂ and underlying n-aSi:H layers. This combination of PEALD, in-system XPS/UPS and ellipsometry allows for a detailed characterization of the n-aSi:H/SnO₂ heterojunction with increasing SnO₂ layer thicknesses. The valence and conduction band offsets are then calculated, as outlined in chapter 3.2.1.4. With this, the band-lineup for this interface can be constructed. Finally, the implications of these findings for the prospective application of this interface in silicon heterojunction solar cells are discussed.

The last section of this chapter focuses on spin-coated SnO₂ layers for implementation in perovskite solar cells. With the recent development of perovskite solar cells, the pure tin oxide material has received more attention as a prominent electron transport layer for perovskite solar cells, because of its suitable valence band offset to perovskite layers [51]. This section presents and investigates the post-treatment oxygen plasma procedure as an option to improve layer surface properties and band alignment to the perovskite layer and thus improving efficiency of the device.

4.2 SnO₂ PEALD process optimization

SnO₂ films were grown by PEALD at a deposition temperature of 90-210 °C using an oxygen plasma produced by a remote plasma source, with an oxygen flow of 100 sccm. The tin precursor was Tetrakis(dimethylamino)tin (TDMASn) (Sigma Aldrich 99.99% purity), which was held at 40 °C in a stainless steel canister. The precursor was fed in using an injector held at 60 °C and helium was used as a carrier gas. The line temperature was kept at 90 °C to prevent condensation of the precursor in the line. 100 sccm of N₂ was used as a purge gas.

Each PEALD sequence consisted of: a TDMASn pulse (1.5 s) - N₂ purge (5 s) - Oxygen plasma pulse (varied duration and power) - N₂ purge (5 s). The pressure was set by a pressure control valve and kept at 0.5 mbar throughout the whole process. All deposited SnO₂ layers for the cycle optimization investigation had thicknesses in the range of 20-30 nm after 200 PEALD cycles, as derived from ex-situ ellipsometry measurements. GPC for different cycle parameters was derived from in-situ ellipsometry measurements.

4.2.1 Optimization of the oxygen plasma pulse step

The TDMASn and N₂ pulses were optimized to yield a saturation in the film growth per cycle. However, the saturation point for the plasma step in PEALD cannot be adjusted in the same way as for thermal ALD, mostly due to plasma kinetics. If the reaction kinetics are slow and the plasma species are distributed isotropically, better quality layers can be obtained before the saturation point is reached [114], [117]. Therefore, the oxidation step parameters (pulse time, plasma power) were optimized with regard to SnO₂ layer conductivity and not step saturation.

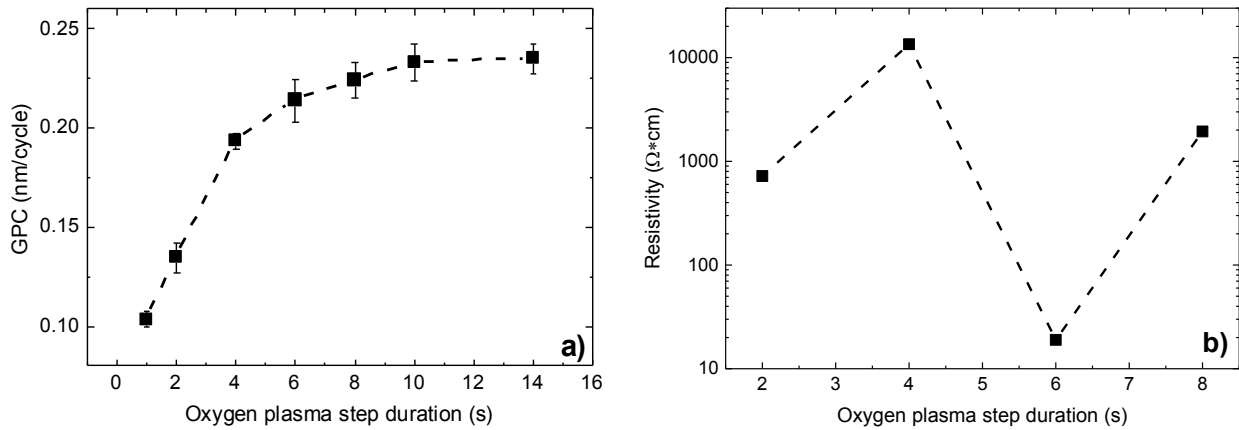


Figure 4.1: a) GPC, and b) resistivity of SnO₂ layer as a function of oxygen plasma step duration.

Therefore, the saturation point of the GPC and layer resistivity were investigated simultaneously. For this variation, the initial deposition temperature was set at 120 °C, and RPS power at 150 W. Fig. 4.1.a shows the GPC for SnO₂ layers for varying oxygen plasma step durations. For short pulses below 4 seconds, layer growth is greatly reduced, which indicates that not all active sites are saturated and the pulse duration is insufficient. For longer pulses of 8-10 seconds, the changes in the GPC are minor and the process can be considered saturated. However, as seen in fig 4.1 b, the minimal resistivity of the layer is achieved for oxygen plasma pulse duration of 6 seconds, which lies before the saturation point for the deposition process. Thus, this pulse length was used for the deposition process.

4.2.2 Optimization of the plasma power

The next important parameter for the PEALD process optimization is the oxygen plasma power. For this variation, the initial deposition temperature was set at 120 °C, and oxygen plasma step duration of 6 seconds. In fig. 4.2 a, the GPC for the SnO₂ layers with increasing RPS power is presented. It can be seen that the saturation of growth is achieved at a plasma power of approximately 500 W. However, as shown in fig. 4.2 b, minimum layer resistivity is achieved at 300 W. With further increases in plasma power, there is an increase in the resistivity of up to 3-4 orders of magnitude. This increase can be caused by plasma damage of the surface, due to the higher power output. Therefore, the optimal RPS power of 300 W was used for the SnO₂ PEALD cycle.

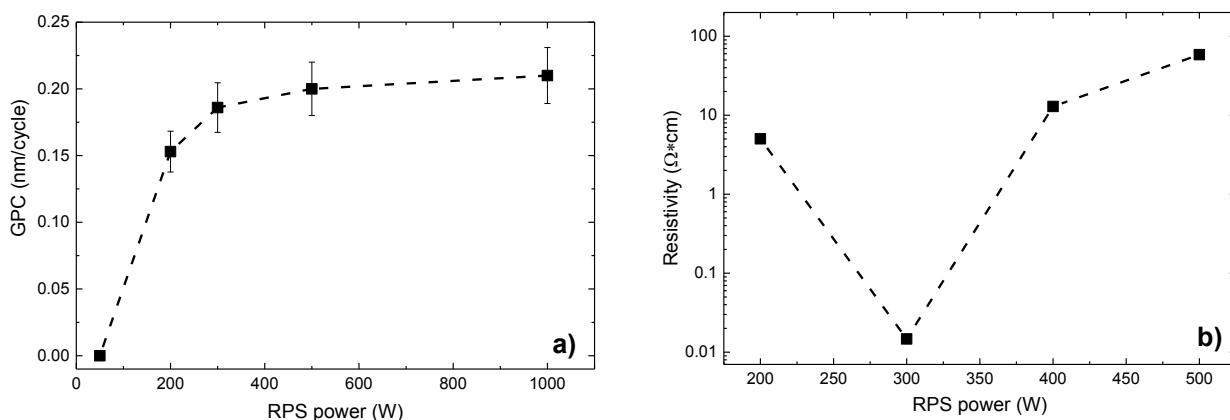


Figure 4.2: a) GPC, b) resistivity of SnO₂ layers as a function of RPS power.

4.2.3 Influence of argon addition on the electrical and optical properties of SnO₂ layers

The addition of argon gas during the oxygen plasma discharge can be helpful for modifying plasma conditions during the deposition process. By doing so, it is possible to increase the oxygen radical concentration [162].

Therefore, the first step is to assess the influence of adding argon to the gas mix on the GPC of the deposition process. Gas concentrations were derived from the respective flow ratios. For this variation, the initial deposition temperature was set at 120 °C, and RPS power of 150 W, and oxygen plasma step at 6 seconds. For low Ar concentrations, around 2%, only slight changes in GPC were observed, as shown in fig. 4.3. However, with greater amounts of argon in the gas mix, the GPC drastically decreases. It is thus possible that the addition of argon leads to a partial etching of the deposited film during the plasma oxidation step.

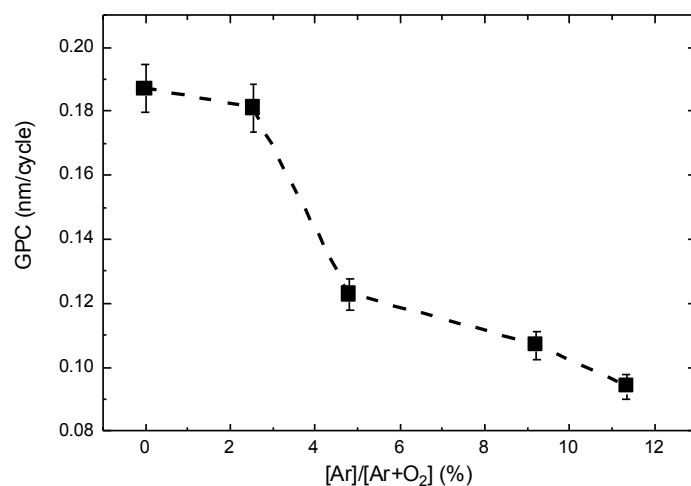


Figure 4.3: GPC for SnO₂ layers with varying Argon concentration during the plasma step.

Next, the influence of argon on the optical and electrical properties of deposited layers is assessed. Fig. 4.4 a,b show the resistivity and refractive index for deposited layers with increasing argon to oxygen ratio in the gas mix. For low argon concentrations, up to 4%, only slight changes are noticeable. However, for higher concentrations there is a drastic decrease in resistivity, of around 3 orders of magnitude. Additionally, the refractive index increases with argon concentration, as shown in fig. 4.4 b. This is also consistent with increased surface etching, as the changes could be explained by the removal of residuals from the surface, which improves opto-electronic properties of the SnO₂ layers. This hypothesis is further substantiated by XPS measurements, as will be seen later in section 4.3.3. Therefore, based on these results in the following an additional flow of 10 sccm Argon was introduced into the chamber during the oxidation step.

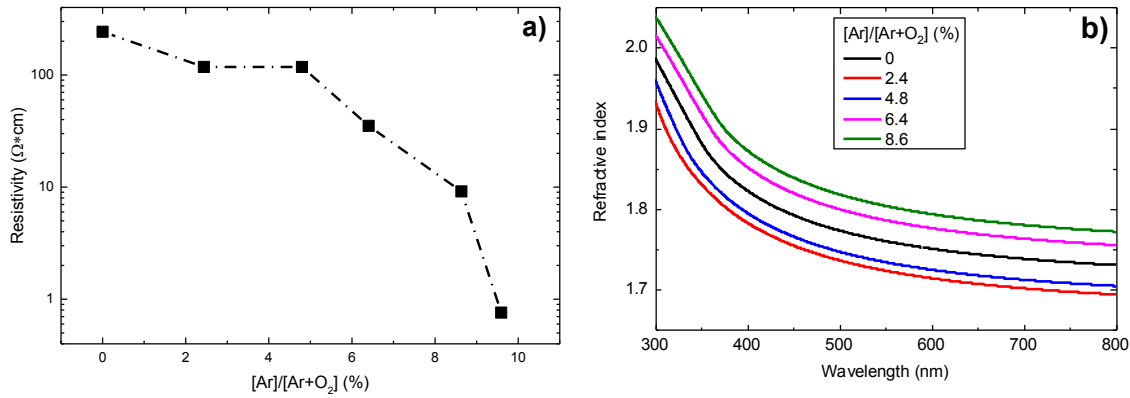


Figure 4.4: a) Resistivity, b) refractive index for SnO_2 layers with varying argon content during the oxygen plasma step.

4.3 Optical and electrical properties of SnO_2 as a function of deposition temperature

In order to investigate the influence of the deposition parameters on opto-electrical properties of the layers, two types of ALD processes were compared at the varied deposition temperatures: the initial and optimized processes. The initial process with not optimized cycle had an oxygen step duration of 2 seconds, with an RPS power of 150 W. After the optimization, which was discussed in the previous section, the optimal oxygen step duration was established at 6 seconds, at an RPS power of 300 W, with the addition of 10 sccm of argon during the plasma step.

4.3.1 Optical properties of PEALD SnO_2 layers

Fig. 4.5 shows the variation of the optical bandgap and refractive index for the deposited SnO_2 layers, as functions of the deposition temperature. Both the optimized and non-optimized PEALD process cycles are considered. For both, refractive index and bandgap, changes are most prominent for the samples with not optimized cycle parameters. With increasing deposition temperature, there is a decrease in the bandgap for the non-optimized process, and only a slight variation for the optimized one. At the same time, the refractive index increases with increasing deposition temperature, being similarly more pronounced for the not optimized parameter set. However, the trend for the refractive index is similar in both cases.

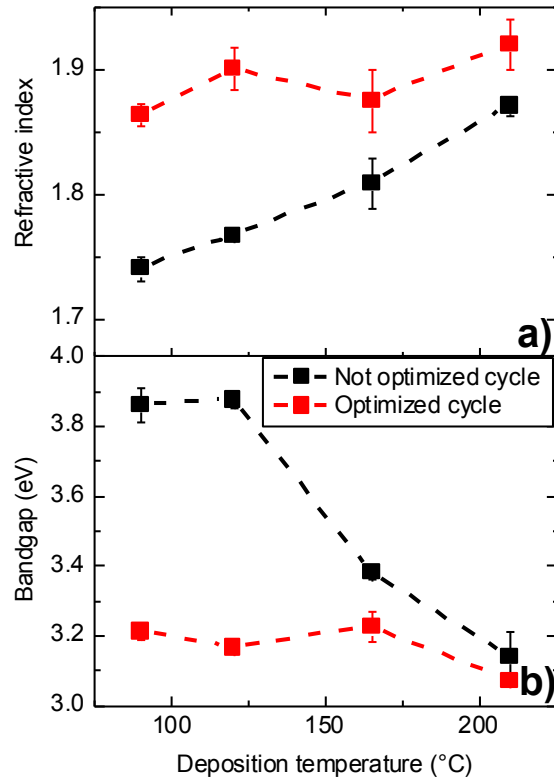


Figure. 4.5. (a) Refractive index at 632.8 nm and (b) optical bandgap for SnO₂ layers deposited using both the not optimized and optimized cycle parameters, as a function of deposition temperature.

For high deposition temperatures, it is possible to achieve refractive index values around 1.9, which is in the range for high-quality SnO₂ thin films [163]. These trends are comparable with the literature for other types of ALD of tin oxide layers [164], [165]. Changes in these parameters with deposition temperature can be correlated to the contamination of the layer with carbon-nitrogen containing residues from the precursor at the surface, or in the bulk, which will be discussed in later sections.

4.3.2 Electrical properties of PEALD SnO₂ layers

Layer resistivity for both optimized and non-optimized cycles and for different deposition temperatures are presented in fig. 4.6. Both trends show similar behaviors with temperature, with a drastic decrease in the resistivity by about 4-5 orders of magnitude when changing the deposition temperature from 80 °C to 210 °C.

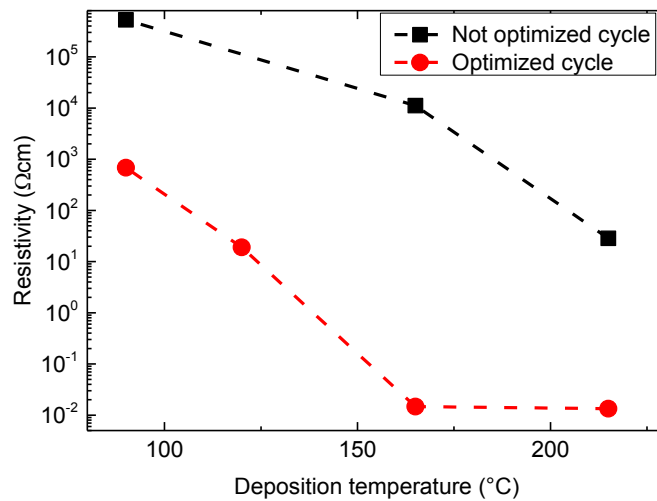


Figure 4.6: Resistivity of SnO₂ layers deposited using both the not optimized and optimized cycle parameters, as a function of deposition temperature.

For samples deposited using the optimized cycle, the resistivity saturates at about 10 mΩcm at a deposition temperature of 165 °C, while the resistivity of samples deposited with the non-optimized process is more than three orders of magnitude higher. For the optimized cycle, the SnO₂ layers show similar conductivities and a comparable trend vs. deposition temperature, as for those reported for thermal ALD using the same precursor [163], [164]. However, even for the optimized cycle, the difference in layer resistivity between low and high temperature regimes is substantial.

The conductivity of the deposited layers can be improved with post-treatments. For the layers deposited at low temperatures, the resistivity can be drastically increased with a short annealing step of 5 minutes at temperatures above 200 °C. Fig. 4.7 shows the resistivity of SnO₂ layers at optimized cycle parameters after 5 minutes annealing at varied annealing temperatures. It can be seen that, for layers with higher deposition temperatures, the difference in resistivity with annealing temperature is minor. However, for layers deposited at 90 and 120 °C, the resistivity can be reduced by 1-2 orders of magnitude by annealing for 5 minutes at 200 °C. This is possible due to the desorption of oxygen and the formation of oxygen vacancies [166]. With further increases in the annealing temperature, the resistivity of these layers is almost comparable to those deposited at higher temperatures.

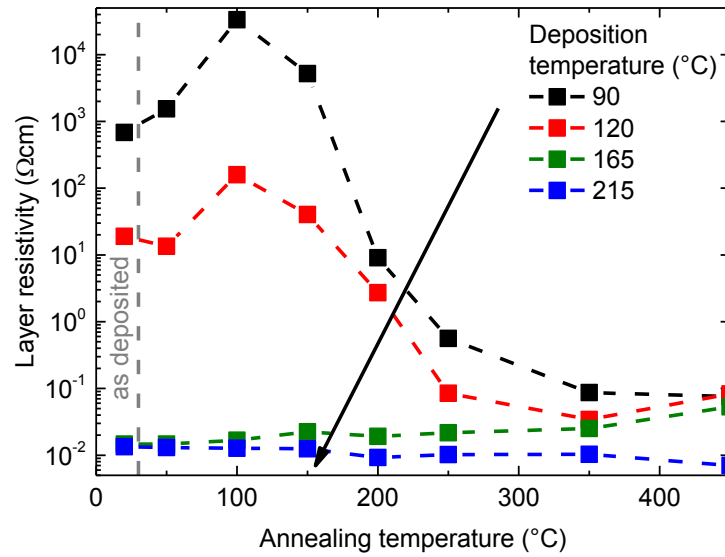


Figure 4.7: Resistivity of SnO₂ layers deposited at different deposition temperatures for optimized deposition parameters after consecutive 5 minutes annealing at varied annealing temperatures.

The increase in resistivity of the layers at low annealing temperatures (100-150 °C) can probably be attributed to the chemisorption of oxygen from the air, which results in the capture of conductive electrons. Slight increases in the resistivity at annealing temperatures above 350 °C can probably be explained by crystallization of the amorphous layers [167].

4.3.3 XPS analysis of SnO₂ layers with varied deposition temperature

The most likely reason for the changes in optical and electrical layer properties with deposition temperature is a change in the deposited layer's composition. Therefore, XPS measurements were conducted to further investigate whether precursor residuals and/or byproducts are present at the surface, or incorporated in the volume of the SnO₂ films.

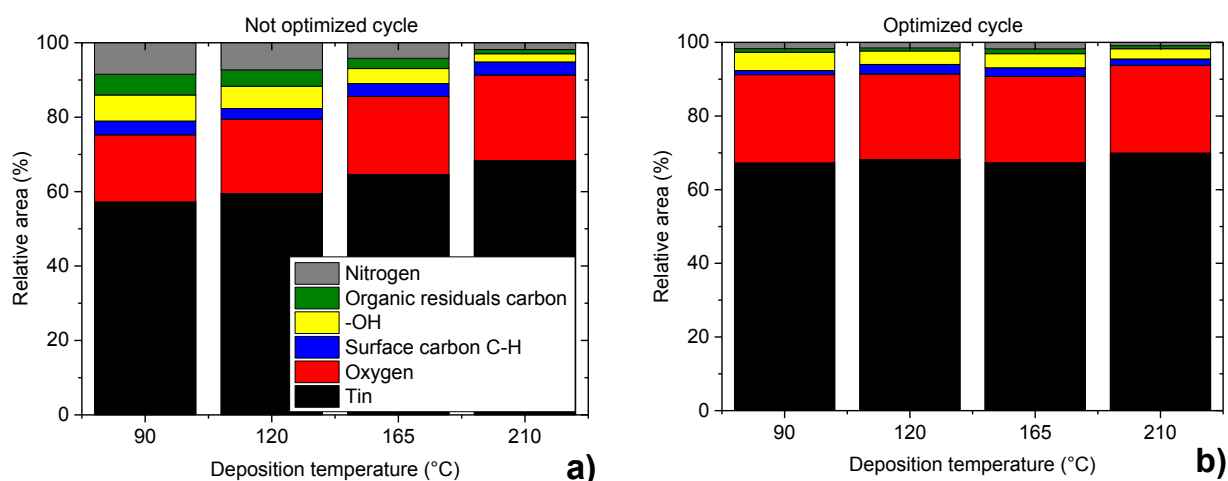


Figure. 4.8: Relative XPS core level peak areas for PEALD SnO₂ layers as a function of deposition temperature for (a) not optimized and (b) optimized cycle parameters.

The analyzed XPS core level data for these SnO₂ layers includes tin 3d_{3/2}, oxygen 1s, carbon 1s and nitrogen 1s signals. Fig. 4.8 shows the relative peak areas for specific core levels compared to the total sum of the areas of the main core levels (Sn 3d_{3/2}, O 1s, C 1s, N 1s) present in the SnO₂ for both processes (“not optimized” and “optimized”). For this plot, the total peak area for the Sn 3d_{3/2} core level spectrum is labeled as “Tin”, the area for the main peak in the O 1s spectra, as “Oxygen”, and the O 1s secondary peak as “-OH”. “Surface carbon C-H” and “Organic residuals carbon” labels correspond to parts of the C 1s signal, which will be discussed in the further section, and “Nitrogen” to N 1s signal. For both the optimized and non-optimized sets of deposition parameters, there is a decrease in the presence of contamination species with increasing temperature. These species include nitrogen, carbon residuals and -OH groups. The decrease is more prominent for the non-optimized cycle parameters, where the total relative area of these species at the lowest temperature was above 24 % and decreases to around 9 %. At the same time, the relative area of the described contamination species at low temperatures for the optimized cycle is almost comparable to the area for high temperatures using the non-optimized cycle. However, the trend with temperature change is similar in both cases. In later subsections, these signals are analyzed in further detail.

4.3.3.1 Evaluation of carbon and nitrogen signals

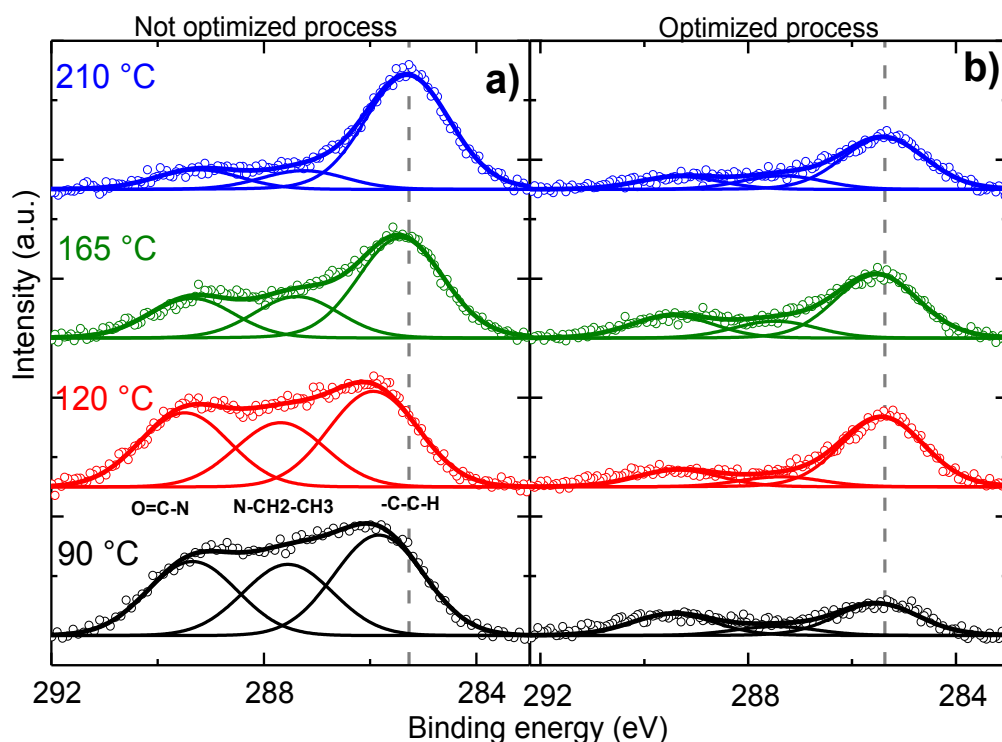


Figure 4.9: C 1s XPS spectra of SnO₂ films deposited at different temperatures for (a) not optimized and (b) optimized process. The spectra (data: open circles; fit: solid lines) are shown after subtraction of the fitted linear background, with identical scaling and are offset for better visibility.

In fig. 4.9, the carbon C 1s core level spectra for SnO₂ layers deposited at different temperatures are shown. Three peaks and a linear background were sufficient to fit these spectra, with binding energies centered at around 285.2-285.5 eV, 287.0-287.3 eV and 289.2-289.5 eV. The shift of the core level for not optimized process samples at deposition temperature 90 °C and 120 °C of approximately 0.2 and 0.4 eV towards higher binding energy is due to the slight charging of the samples. This shift is persistent for other core levels and thus is not discussed in details. The peak with the highest binding energy at about 289.4 eV can be attributed to O=C-N bonds [168], or other carboxyl-containing precursor residues. The peak at about 287 eV can be attributed to carbon-nitrogen bonds in ethyl groups of the form N-CH₂-CH₃ [169] from TDMASn precursor residues. The third one, with the lowest binding energy is attributed to carbon atoms bonded to hydrogen [169]. Unlike the previous two peaks, does not show any clear correlation with

changing deposition temperature or with other deposition parameters. The two peaks in the C 1s signal, which are assumed to be due to precursor residuals, show a clear decrease in peak area with increasing deposition temperature, especially for the non-optimized process.

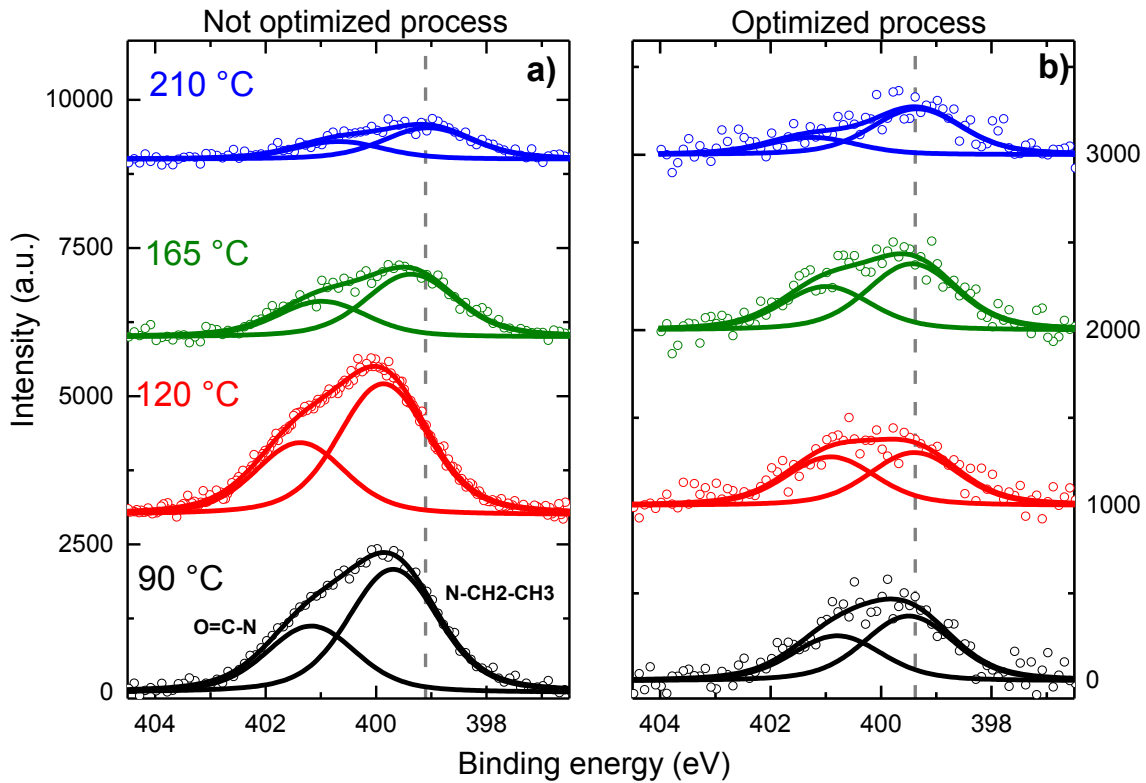


Figure 4.10: N 1s XPS spectra for SnO₂ films deposited at different temperatures for (a) not optimized and (b) optimized process. The spectra (data: open circles; fit: solid lines) are shown after subtraction of the fitted linear background and are offset for better visibility.

The next important signal to analyze stems from the N 1s core level. Similar to the carbon signal, there is a clear correlation between the overall peak area and deposition temperature, as shown in fig 4.10. The spectrum was fitted with two peaks, where the signal at the lower binding energy of 399.2-399.5 eV is assumed to originate from the N-CH₂-CH₃ TDMASn precursor residues [169], and the higher energy part of 401.5-401.8 eV from O=C-N related bonds, as concluded from fig. 4.9 [168].

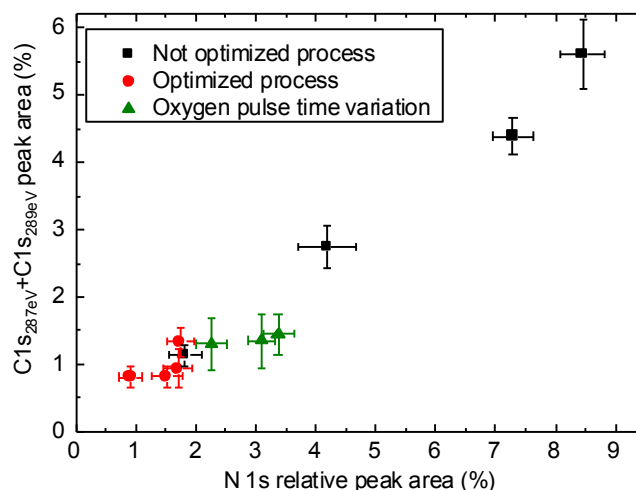


Figure 4.11: Sum of relative peak areas for the 287-287.3 eV (“C1s_{287eV}”) and the 289.2-289.5 eV (“C1s_{289eV}”) contributions to the C 1s core level plotted versus the total relative area of the N 1s signal. Data points represent samples from the three studied sample sets: not optimized process, optimized process and oxygen pulse time variation at 120 °C.

In Fig. 4.11, the sum of areas of the C 1s contributions that are assumed to be due to precursor residuals is plotted against the total area of the N 1s peak for different deposition conditions. Clearly, with increasing nitrogen N 1s area, there is also an area increase for the two high-binding energy C 1s signals. This shows that these two groups of signals are directly related to each other. Therefore, it is likely that these signals are indeed caused by TDMASn residuals incorporated in the SnO₂ layers and that these residuals contain nitrogen-carbon bonds. Since the intensities of these signals decrease with increasing deposition temperature, it can be surmised that with increasing deposition temperature fewer precursor residues are incorporated into the layer and at the surface, due to more efficient precursor reactions.

However, even at the highest investigated temperatures and for the optimized cycle, a measurable amount of carbon and nitrogen contamination can still be detected. In contrast, for SnO₂ layers deposited with TDMASn by thermal ALD [163]–[165], [170], no nitrogen or carbon was found in the films for deposition temperatures above 200 °C. It can be concluded that, for PEALD, the incorporation of impurities from the precursor cannot be prevented even at elevated deposition temperatures. Therefore, it is important to understand how the contamination from the precursor affects the optical and electrical characteristics of the deposited films. To this end, samples with different deposition conditions were further

investigated in terms of their electrical and optical properties, with results shown in fig. 4.11 vs. the relative nitrogen N 1s peak area.

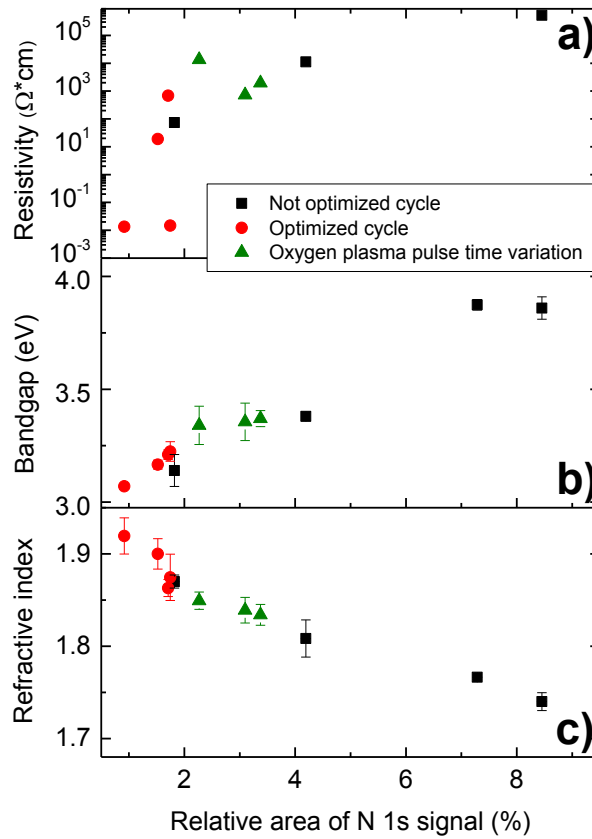


Figure 4.11: (a) Layer resistivity, (b) optical band gap and (c) refractive index at 632.8 nm for PEALD SnO₂ layers, as functions of the relative area of the N 1s signal. Data points represent samples from the three studied sample sets: not optimized process, optimized process and oxygen pulse time variation at 120 °C.

Regarding the electrical properties, there is a correlation between resistivity and nitrogen contamination in the layers, as shown in fig. 4.11 a. However, the data is quite scattered, which can indicate that surface and substrate contamination as probed by XPS relate to the resistivity of the layers, but that there are possibly other parameters that influence it to a higher extent, e.g. the crystallinity of the layers.

At the same time, as seen in fig. 4.11 b and c, the optical band gap and refractive index, which were extracted from ellipsometry measurements for investigated layers, strongly depend on the amount of nitrogen-containing residues from the precursor. Additionally, the highest refractive

index and minimal band gap are achieved for the lowest amount of precursor residuals in the layer. The relationship between bandgap and the amount of residues in the layer can have next possible explanation: as it is known for i-aSi:H layers, the presence of hydrogen can replace weak Si-Si bonds with more stable Si-H bonds. Therefore, there is an increase in the bandgap due to a shift in the valence band from the Fermi level, with the conduction band remaining almost at the same level [27]. For the SnO₂ layers, a similar behavior might take place [171].

4.3.3.2 Evaluation of the oxygen signal

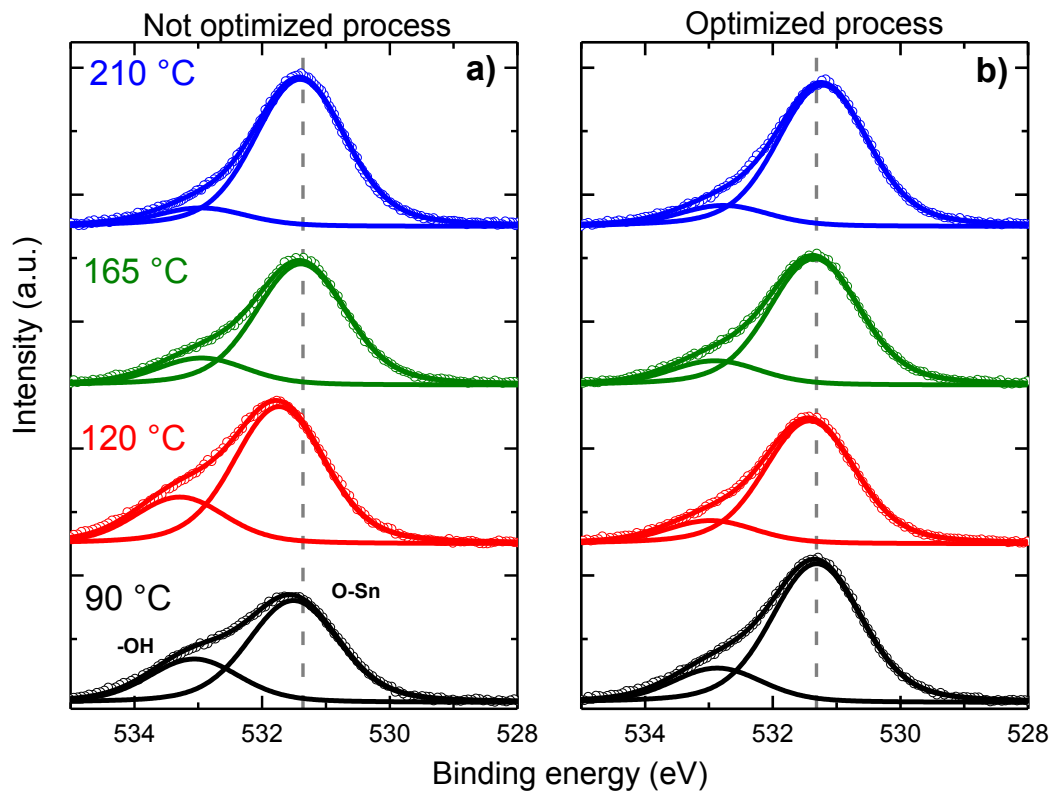


Figure 4.12: O 1s XPS spectra of SnO₂ films deposited at different temperatures for (a) not optimized and (b) optimized process. The spectra (data: open circles; fit: solid lines) are shown after subtraction of the fitted linear background, with the same scaling and are offset for better visibility.

The nitrogen and carbon signals are not the only ones that show a dependence on deposition temperature. As seen in fig 4.12, the O 1s core level signal also undergoes changes upon

variation of the deposition temperature. The O 1s signal was fitted with two components: the main peak centered at 531.2-531.4 eV, which corresponds to O-Sn bonds [172], and the secondary signal centered at 532.7-533.3 eV, which corresponds to other oxygen species like -OH groups or carboxyls [173], [174]. However, it is not possible to discriminate between -OH groups and carboxyls in these spectra, since their binding energies have a significant overlap. For the sample with optimized process deposited at 210 °C a slight additional shift of O 1s core level towards lower binding energy can be observed. The reasons for this shift are not fully clear. However, it is possible that this shift is caused by the stoichiometry change of the layer at this deposition temperature. This will be discussed in the next section. With increasing temperature, the O-Sn related signal intensity remains almost constant, while the impurity related signal intensity decreases. Assuming the high-binding energy contribution to the O 1s signal is indeed due to -OH groups, then a possible explanation for its temperature-induced decrease is dehydroxylation with increasing temperature [175]. However, it is known for PEALD of Al₂O₃ that -OH groups can be located not only at the surface, but can also be incorporated into the layer [117], [161]. This might then also happen during SnO₂ PEALD. However, from the obtained data, it is not possible to state whether -OH groups are located only at the surface or also incorporated in the bulk.

4.3.3.3 Evaluation of the tin signal and layer stoichiometry

The next step is to evaluate the tin 3d core level signal. Fig. 4.13 shows the evaluation of the Sn 3d_{3/2} core level signal for different deposition temperatures, both for the non-optimized and the optimized processes. The signal was fitted with two components, which correspond to two tin valences: Sn⁴⁺ and Sn²⁺. No presence of metallic Sn⁰⁺ was detected in any of the samples. The peak corresponding to Sn⁴⁺ was fitted at binding energies of 496.1-496.3 eV. Sn²⁺ peaks were fitted at lower binding energies, at a distance of 0.64 eV to those for Sn⁴⁺, which is comparable to literature data [176]. For the non-optimized process, at all deposition temperatures, only Sn⁴⁺ is present, except at 120 °C, where a small amount of Sn²⁺ is detectable. Therefore, for the non-optimized process, the deposited layers can be considered fully stoichiometric.

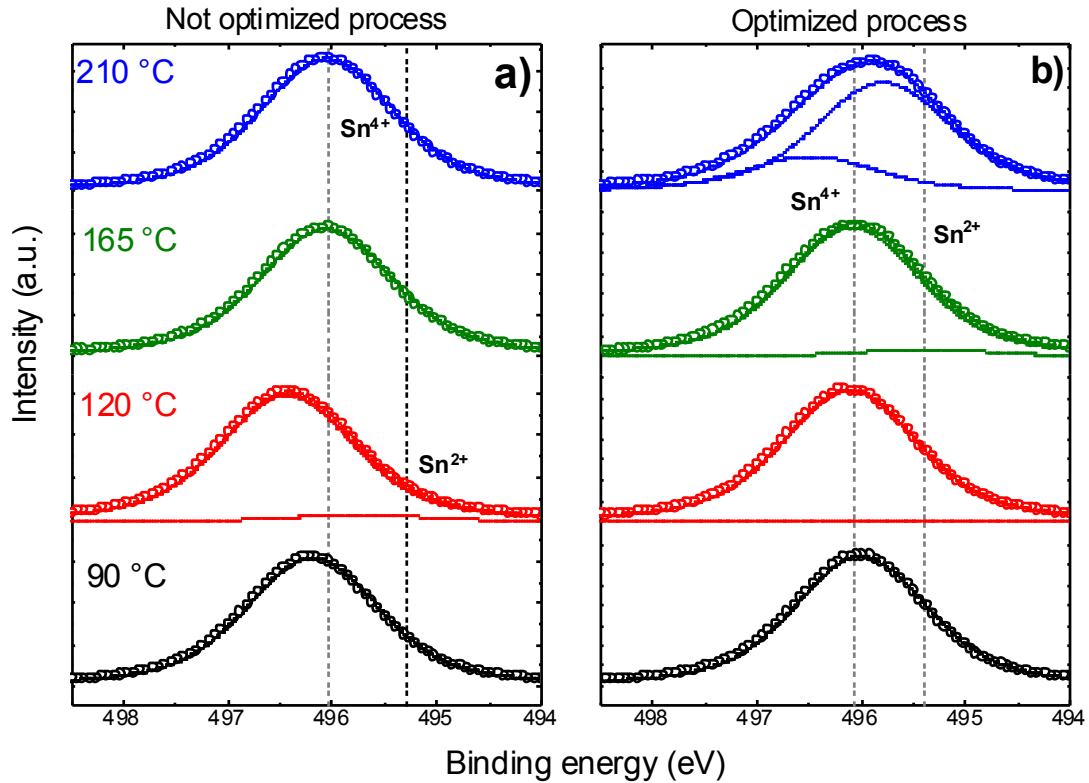


Figure 4.13: Sn $3d_{3/2}$ XPS spectra of SnO_2 films deposited at different temperatures for (a) not optimized and (b) optimized process. The spectra (data: open circles; fit: solid lines) are shown after subtraction of the fitted linear background and are offset for better visibility.

However, for the optimized cycle, there is an increase in the presence of Sn^{2+} with increasing deposition temperatures. At the highest investigated temperature of 210 °C, Sn^{2+} is the dominant signal. Moreover, for this sample, there is an additional shift of the core level towards higher binding energies. It can then be said that, for the optimized process, layers become less stoichiometric with increasing deposition temperature. The dominant presence of Sn^{2+} at high deposition temperatures can be explained either by a partial decomposition of the precursor at regarded process conditions, or, additionally, by the possible influence of the argon plasma during the deposition process for optimized process. It has been shown for other metal oxide layers that argon plasma post-treatments can lead to a decrease in layer stoichiometry [177].

4.4 Band offset between SnO₂ layers and hydrogenated amorphous silicon

Due to SnO₂ being an n-type semiconductor, it can be combined with n-aSi:H to form an electron selective contact, as a bilayer. It is also conceivable to deposit it on an undoped passivation layer as a stand-alone electron-selective contact. Previous studies of sputtered [178] and CVD-grown [179] SnO₂ on crystalline silicon have been conducted, but the chemical composition and properties of the interfacial region have not been investigated in detail,. However, the inverted structure, i.e. growth of silicon on SnO₂, has been investigated in detail in context of the silicon-based solar cells [180], [181], including an analysis of the incubation layer. A reduction of SnO₂ after the first deposition stages, as well as the formation of an intermediate silicon oxide at the interface, were observed. Regarding the growth process of SnO₂ on silicon, it is worth investigating if the deposition of SnO₂ in an oxygen rich environment could prevent the reduction of SnO₂, which can occur due to the formation of the intermediate silicon oxide at the interface. Such conditions can be achieved in the PEALD process, in which highly reactive oxygen radicals are present during the oxygen plasma step in every cycle. Moreover, ALD enables the monitoring of changes at the interface for different levels of SnO₂ film growth, with monolayer scale resolution. Thus, it is possible to have a detailed representation of the formed interface at each growth stage.

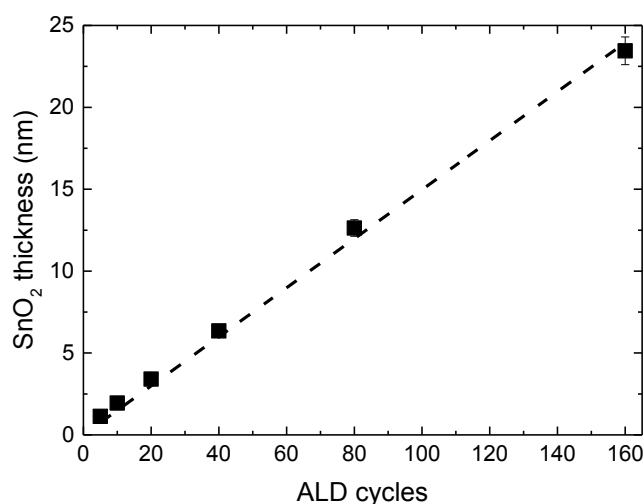


Figure 4.14: Thickness of SnO₂ films with increasing number of PEALD cycles from the in-situ ellipsometry measurements.

Therefore, in this section the evolution of the interface between n-aSi:H and SnO₂ for increasing SnO₂ layer thickness is investigated. The thickness of the overlayer is controlled by increasing the number of PEALD cycles. The growth of SnO₂ layers within the optimized process cycle at a deposition temperature of 150 °C displays a linear behaviour, as shown in fig. 4.14. The GPC of PEALD for SnO₂ at these conditions is around 0.17 nm/cycle. This temperature enables a low concentration of precursor residues, as discussed in the previous sections. Additionally, it is possible to avoid degradation of the amorphous silicon layers, which would occur at elevated temperatures [182], and to exclude an annealing effect on the a-Si:H layers during the deposition process.

In-system UPS and XPS measurements were used to monitor shifts in the core levels and the valence band edge positions of the silicon substrate and SnO₂ film. Additionally, *ex-situ* spectroscopic ellipsometry was used to extract the band gap of both the SnO₂ layers and the underlying n-aSi:H layers. This combination of PEALD, in-system XPS/UPS and ellipsometry makes it possible to thoroughly characterize the n-aSi:H/SnO₂ heterojunction for increasing SnO₂ thicknesses, as discussed in chapter 3.2.1.4. Therefore, the valence and conduction band offsets can be estimated for different growth stages of the SnO₂ layers.

For the interface investigation, crystalline silicon wafers (n-type, resistivity 1-3 Ωcm) coated with a stack of 20 nm intrinsic and 20 nm n-doped a-Si:H were used as substrates. These layers were deposited by PECVD and the relevant process parameters and pre-treatments of the wafer are outlined in chapter 3.1. The additional intrinsic amorphous silicon layer was deposited to prevent epitaxial growth of the n-doped amorphous silicon. After the PECVD process, samples were moved to the ALD chamber with a short (< 1 min) air exposure in between. Before the PEALD process, the substrates were exposed to nitrogen gas flows in order to stabilize the substrate temperature. After the deposition, samples were directly transferred to the XPS chamber in ultra-high vacuum (UHV) with a base pressure in the range of 5×10^{-9} mbar. The highest pressure the samples were exposed to during the transfer was 10^{-7} mbar for very short (on the order of seconds) intervals. This was due to the rapid movement of the UHV transfer mechanisms, the opening/closing of valves and the base pressure of the transfer chamber for the deposition chamber. In order to have a detailed understanding of the interface chemistry and electronic structure of the interface, XPS spectra for the Si 2p, O 1s and Sn 3d_{3/2} core levels are discussed. Peak positions for the XPS measurements were aligned on the energy scale using the binding energy position of the surface –C-C-H component of the carbon 1s core level [183].

This originates from precursor residuals, as discussed in the previous sections and appears to be independent of the process conditions.

4.4.1 XPS analysis of SnO₂ layers with increasing thickness

4.4.1.1 Si 2p analysis and intermediate oxide thickness estimation

Fig. 4.15 a shows the evolution of the Si 2p core level signal with increasing numbers of PEALD cycles. The core level can be divided into five main parts: The Si⁰⁺ and the four oxidation states of silicon [184]. Before the first PEALD cycle, i.e. on the bare n-aSi:H layer, only the Si⁰⁺ and Si¹⁺ oxidation states are detectable. However, already after the first deposition cycle, there is a drastic increase in signals at higher binding energies that are characteristic of higher oxidation states, which indicates the oxide layer formation. Thus, an intermediate silicon oxide layer is formed at the interface between the Si and SnO₂. After about 5 to 10 cycles (0.85-1.7 nm SnO₂ layer thickness), the ratio of the areas of the peaks that correspond to the oxidation states, relative to the Si 2p peak, stabilize and remain unchanged during further growth of the SnO₂, for as long as the Si signal remains detectable.

Assuming that the intermediate SiO_x layer at the interface is fully formed after 1-3 cycles, its thickness can be determined from the Si 2p core level intensity, from the equation discussed in chapter 3.2.1.3 [185]:

$$T_{ox} = \lambda \cos \theta \ln \left(\frac{R_{exp}}{R_0} + 1 \right). \quad (4.1)$$

Here, λ is the attenuation length of the Si 2p photoelectrons in a SiO₂ matrix, θ is the angle between the surface normal and the analyzer. $R_0 = \frac{I_{SiO_2}^{\infty}}{I_{Si}^{\infty}}$ is the intensity of the Si 2p core level emission measured on a thick silicon oxide, relative to the emission of silicon without the oxide overlayer. Values for λ and R_0 were taken from the literature: 2.91 nm and 0.89, respectively [186]. R_{exp} indicates the relative intensity of the measured values. Applying these equations for the Si 2p core level intensity after 1-3 ALD cycles, the calculated value for the SiO_x thickness at the interface is approximately 0.45±0.1 nm.

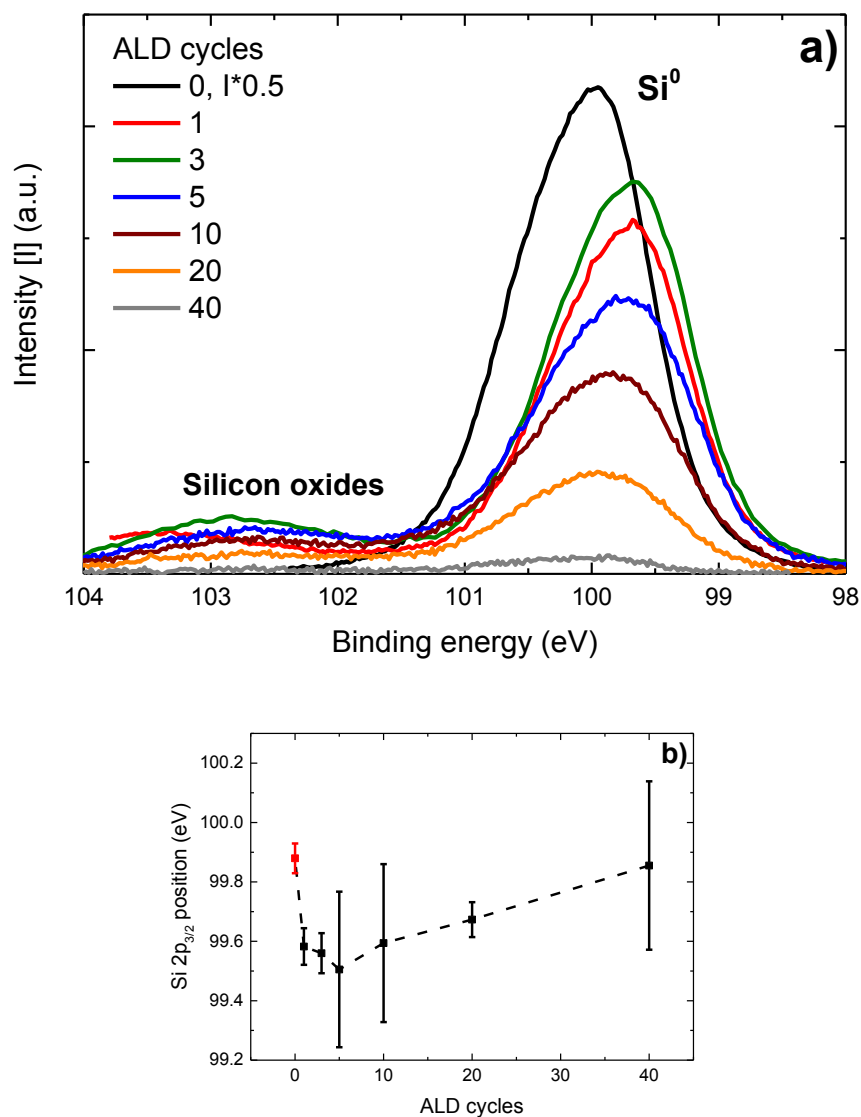


Figure 4.15: Background corrected XPS spectra for the Si 2p core level. The spectrum of the uncoated n-aSi:H sample (0 PEALD cycles) is scaled by a factor of 0.5 for better visibility and is shown in red. b) Si 2p_{1/2} peak position after a varied number of ALD cycles. Increased error bars for 5,10 and 40 cycles are due to the sample charging.

With increasing numbers of cycles, the total intensity of the Si 2p peak decreases due to the increased thickness of the SnO₂ overlayer. The non-oxidized Si 2p doublet is present for all tin oxide film thicknesses, as long as this core level is detectable. Additionally, after the first cycle, the Si 2p signal shift toward lower binding energy. However, with an increasing number of ALD cycles, the shift is reversed towards higher binding energies, as it shown in fig 4.15 b. The decreased binding energy after first ALD cycles is an indication of a negatively charged oxide

layer, yielding an additional upwards band bending (attracting holes) in the n-aSi:H close to its interface to the oxide [187]. The change of the shift direction indicates that either this interfacial fixed charge is lost, or that it is overcompensated by positive fixed charges in the growing SnO₂ film.

4.4.1.2 Changes in main core level signals with increasing SnO₂ layer thickness

In addition to the previously discussed orbital, the Sn 3d core level and Sn MNN level were analyzed. Fig. 4.16 a shows the evolution of the Sn 3d_{3/2} signal for increasing numbers of PEALD cycles. This core level was fitted with a similar procedure to the one discussed in chapter 4.3.3.3, with two signals that correspond to the oxidation states Sn⁴⁺ and Sn²⁺. The main peak is assumed to be the Sn⁴⁺ oxidation state, since its binding energy position is consistent with previously reported values [188]. The second peak, with the lower binding energy at a distance of 0.64 eV to the Sn⁴⁺ peak, corresponds to Sn²⁺. No other peaks at lower binding energies were observed, therefore it can be surmised that, at every stage during the film formation, no metallic Sn⁰⁺ is present. From fig. 4.16 a and c, it is clear that after one ALD cycle the ratio between these two peaks is almost 1:1. However, with further deposition cycles the Sn⁴⁺ peak intensity relative to Sn²⁺ continuously increases, up to 10 ALD cycles. Afterwards, the Sn²⁺ state is no longer detectable. Therefore, it can be said that, during the first 10 ALD cycles, an intermediate state of tin is present in the layer. Afterwards, the layer reaches stable growth conditions, and only stoichiometric Sn⁴⁺ is present in the fully formed layer. Similar to Si 2p core level, there is an observable shift of the core level signal with the increasing number of deposition cycles, which is observed for the intermediate layer and indicates band bending of not only in the substrate, but in the overlayer.

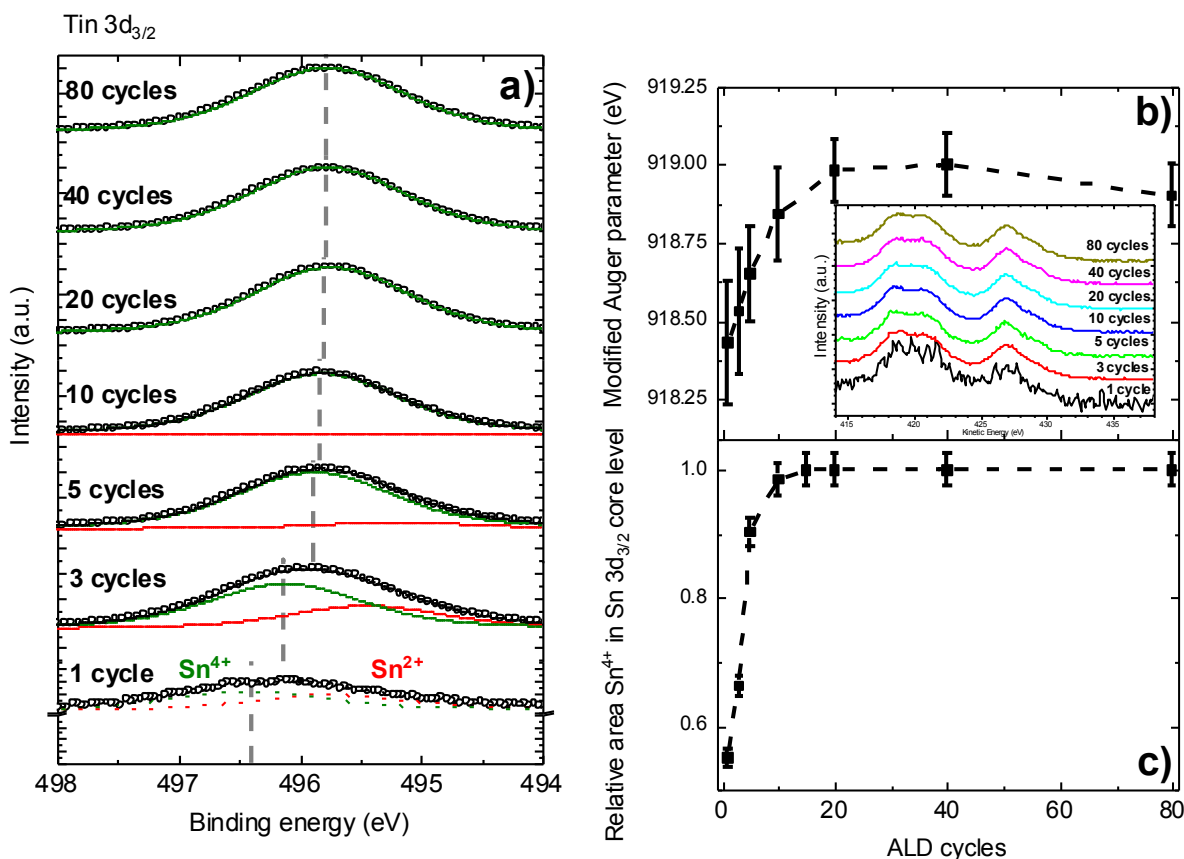


Figure 4.16: a) Fits and raw data of the Sn $3d_{3/2}$ XPS signal after subtraction of fitted linear background for increasing numbers of PEALD cycles. The spectra (data: open circles, fit: solid lines) are offset for better visibility. Gray dash lines indicate the position of Sn^{4+} peak. b) Sn $3d - \text{Sn}$ MNN modified Auger parameter (α'). The inset graph shows Sn MNN Auger spectra after subtracting the background at 435 eV at kinetic energy and shifted in energy to overlap with 80 cycle spectra, using zero-crossing of the first derivative. c) Ratio of Sn^{4+} bonds in the Sn $3d_{3/2}$ core level. Dashed lines serve as guides to the eye, both as functions of the number of PEALD cycles.

Additionally, the Sn MNN Auger spectra were analyzed. The modified Auger parameter (α') gives chemical composition information by combining the binding energy of a core level with the kinetic energy of the corresponding Auger spectrum (Sn $3d_{5/2} - \text{Sn}$ MNN), which numerical value can describe the chemical state of Sn. By adding two contributions, shifts due to e.g. charging are cancelled out, and so it is possible to probe the Sn state in a way that is free from the uncertainties involved in referencing the C $1s$ core level position. To exclude the presence of the satellite intensity of Mg K_b , that is located at the 8.54 eV distance, which is similar to

spin-orbit splitting of Sn 3d core level (8.45 eV) distance, the Sn 3d_{3/2} core level was analyzed and spin-orbit splitting distance was subtracted [124]. Thus, this calculated value can be compared with the literature values for tin oxide. Fig. 4.16 b shows the Sn 3d_{5/2}-MNN modified Auger parameter as a function of the number of deposition cycles. All values are in the range that is expected for Sn oxides [189]. There is a clear tendency of the Auger parameter to increase until 20 cycles, then leveling off at 919.1±0.1 eV, a value that corresponds SnO₂. The lower values for fewer deposition cycles suggest that the material formed at the interface is more like SnO than SnO₂, which agrees with the discussed Sn 3d core level analysis.

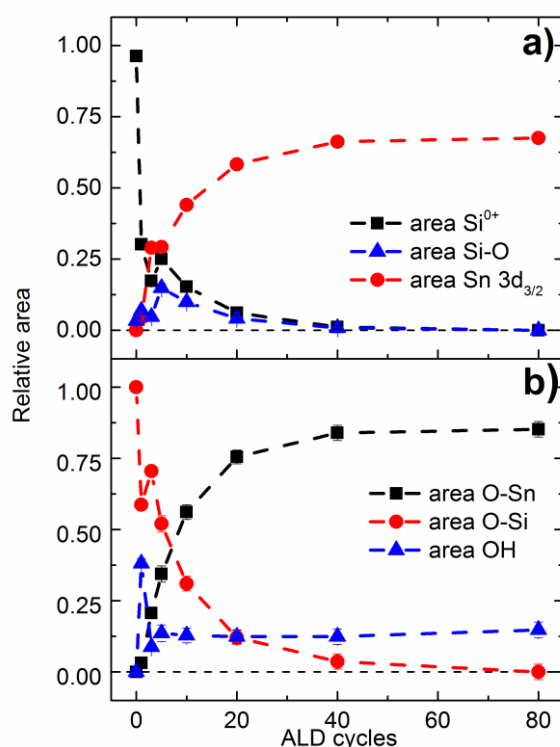


Figure 4.17: a) Relative area of the Si 2p⁰⁺, Si 2p^{1+,2+,3+,4+} (Si-O) and Sn 3d_{3/2} core levels. b) Relative area of the contributions of O-Sn, O-Si and -OH bonds to the O 1s core level. All values are plotted vs. the number of PEALD cycles.

Moving on with the XPS analysis, fig. 4.17 a displays the relative XPS signal intensities of the Si 2p and Sn 3d_{3/2} core levels plotted versus the number of PEALD cycles. The Sn 3d_{3/2} orbital has been already detectable after the first cycle. This indicates that, already within the first cycle, tin is able to bond to the a-Si:H surface. Thus, there is no growth delay for the PEALD process. Additionally, the intensity of the silicon bulk signal decreases with SnO₂ film

thickness, until it is no longer detectable after 40 cycles. Therefore, only tin oxide is observed after further deposition steps and the film can be considered a closed, fully formed layer.

The next core level of interest is the O 1s orbital. The O 1s core level was fitted with three signals: the O-Sn bond at a binding energy of about 530.6-531.3 eV, the O-Si bond at a distance of 0.89 eV relative to the O-Sn bond [179], and -OH related surface groups [190] at a distance of 1.73 eV from the O-Sn bond. Fig. 4.17 b displays the relative contributions of these three signals to the total intensity of the O 1s signal, plotted versus the number of PEALD cycles. It can be seen that the O-Si bond fraction of the O 1s core level continuously decreases, while the O-Sn bond signal increases for increasing numbers of PEALD cycles. Finally, the O-Si bond fully disappears after 80 cycles, with only O-Sn and -OH bonds detectable, which coincides with the absence of the Si 2p XPS signal. Additionally, with the increase in SnO₂ layer thickness, the -OH component ratio remains almost unchanged. Therefore, it can be surmised that the -OH species are mostly surface-related [161].

4.4.2 UPS analysis of SnO₂ layers

Moving on, from UPS measurements it is possible to quantify the work function and the valence band edge positions for the SnO₂ layers after different growth steps. The fitting procedure is described in chapter 3.3.2.

The cut-off region for the UPS spectra and the extracted work function values for layers with increasing numbers of PEALD cycles are shown in Fig. 4.18 a and c, respectively. In both graphs, a drastic shift in the work function for the first cycles is apparent, which presumably reflects the oxidation of the silicon surface [191]. During the first 5-10 cycles, an intermediate tin oxide layer is grown, which features a lower work function than for the thick SnO₂. However, after 15 cycles the work function stabilizes, which indicates that at this stage the incubation of SnO₂ on the silicon/silicon oxide surface has been completed and the growth has entered a stable regime. This agrees with observations of the Sn 3d core level, where at this stage of growth only the Sn⁴⁺ oxidation state is present. The work function for the final SnO₂ layer after 80 cycles was measured at about 4.82±0.1 eV. This is consistent with literature values, which are between 4.4 and 5.7 eV, depending on the surface state of the material [191]. Oxygen rich SnO₂ surface tends to exhibit higher work function, whereas reduced surface tends to work function lowering [38]. However, this value is higher than those reported for other

n-type semiconductors, such as ZnO (4.4 eV) [192] or TiO₂ (4.2 eV) [193]. Such high work functions can be an issue for using PEALD SnO₂ as an electron contact in silicon heterojunction solar cells, due to its negative impact on the fill factor, as shown in simulations [6], [131].

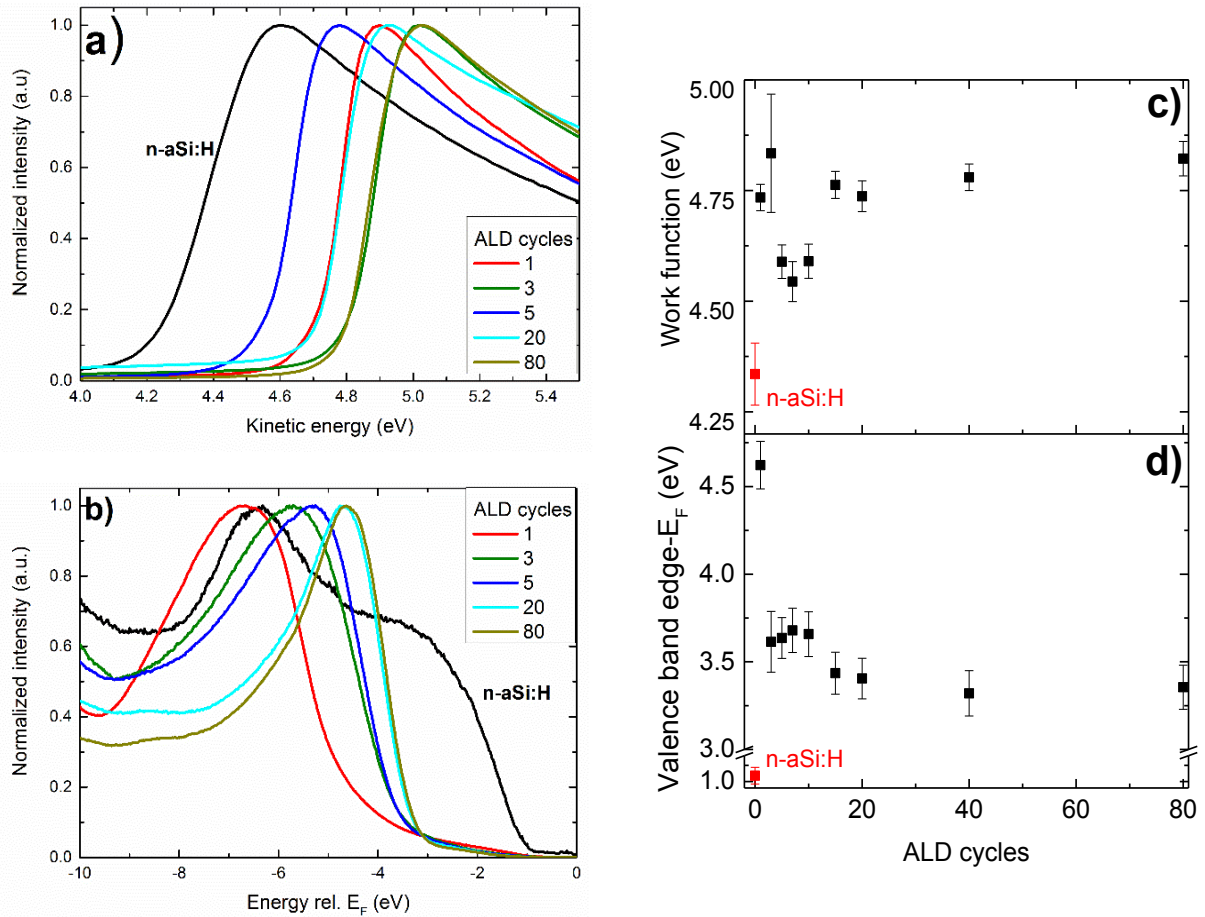


Figure 4.18: UPS spectra for SnO₂ layers deposited on top of n-doped amorphous silicon and measured after different numbers of ALD cycles. a) Secondary cut-off after extracted bias, b) valence band region of the UPS spectra with normalized signal intensity, c) work function of SnO₂ layers on n-aSi:H, d) valence band edge energies relative to E_F as a function of the number of PEALD cycles.

Fig. 4.18 b displays the normalized valence band spectra, obtained by UPS, vs. kinetic energy. It is clear that the position of the leading edge of the spectrum shifts with increasing numbers of ALD cycles. Additionally, the shape of the valence band changes from that of pure a-Si:H to SnO₂. The shape of the signal undergoes the most drastic change after the first PEALD cycle, where it is possible to detect the intermediate stage between SnO₂ and Si. The valence band

edge energies E_v relative to the Fermi level were obtained using the fitting procedure discussed in chapter 3.2.1.2, and are plotted against the number of PEALD cycles in Fig. 4.18 d. The valence band edge position for the n-aSi:H layer was measured at 1.1 eV below the Fermi level. Similar to the work function, a rapid shift in the valence band edge position after the first PEALD cycle is observed. This is due to the formation of an intermediate silicon oxide on the surface, which has a much lower valence band edge position, $E_v - E_F = 4.62 \pm 0.2$ eV. This is consistent with the growth of a silicon oxide on the a-Si:H, which has a valence band offset of ~ 4 eV to a-Si:H [194]. With continued deposition up to 15-20 cycles, there is a noticeable shift in E_v values and slight further changes in the shape of the curve, which might be correlated to the previously discussed presence of Sn^{2+} . The valence band edge position saturates after 20 cycles and, for thick SnO_2 layers, reaches about 3.32 ± 0.15 eV.

4.4.3 Band offset between SnO_2 and n-aSi:H layers

The next step is to discuss the electronic band line-up at the $\text{SnO}_2/\text{n-aSi:H}$ heterojunction. The XPS and UPS measurements discussed so far allow extracting the valence band edge positions of n-doped amorphous silicon and SnO_2 at the different growth stages, relative to E_F . Additionally, spectroscopic ellipsometry was used to determine the bandgap E_g for the PEALD grown SnO_2 layers and the amorphous silicon. Thick SnO_2 layers (after 40 cycles) were fitted with the Tauc-Lorentz model, with a bandgap of 3.38 ± 0.1 eV, which was assumed constant for all other SnO_2 thicknesses. The n-aSi:H layer was fitted using a Drude-Lorentz model and its band gap was found to be 1.65 ± 0.05 eV.

Finally, the construction of a complete band line-up necessitates determining band offsets between SnO_2 and n-doped amorphous silicon. This information can be obtained from the Si 2p and Sn 3d core level binding energies, extracted from XPS measurements, as well as the valence band edges from UPS measurements for samples with different SnO_2 thicknesses by the Kraut method, as discussed in chapter 3.2.1.4. The valence band offset ΔE_v can be estimated as follows [138]:

$$\Delta E_v = E_{\text{over}}(\text{SnO}_2) - E_{\text{sub}}(\text{Si}) + \Delta E_{\text{CL}}. \quad (4.2)$$

In this case, $E_{\text{over}}(\text{SnO}_2)$ is the difference between the Sn^{4+} 3d_{3/2} core level position and the valence band edge for the layer stack after 80 cycles (reduced binding energy). At this thickness, no silicon signal is detectable. Therefore, it can be assumed that there is no influence from the

silicon interface at this growth stage. $E_{\text{sub}}(\text{Si})$ is the difference between the Si $2p_{3/2}$ core level position and the valence band edge for a bare n-aSi:H film. ΔE_{CL} is the difference between the $\text{Sn}^{4+} 3d_{3/2}$ and Si $2p_{3/2}$ core level positions at the intermediate or interface state, where both, substrate and overlayer are detectable.

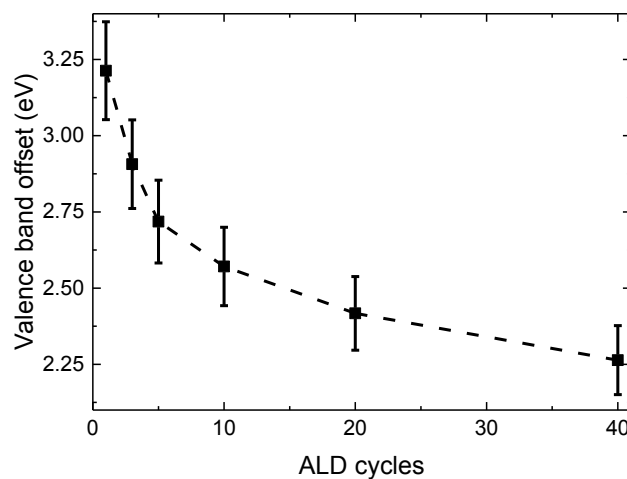


Figure 4.19: Valence band offset for the $\text{SnO}_2/\text{n-aSi:H}$ interface plotted versus the number of PEALD cycles.

The evolution of the valence band offset with increasing numbers of PEALD cycles calculated by the Kraut method is represented in fig. 4.19. It is possible to see that with increasing thickness of the deposited layer, the valence band offset continuously decreases. It is likely that this is due to two effects that are difficult to distinguish, one related to the materials, the other to the evaluation method. Firstly, the mentioned intermediate silicon oxide (SiO_x) formed during the first ALD cycles can be expected to have a larger band offset to the a-Si:H than the SnO_2 formed at later stages. Secondly, there are fundamental limitations to the applicability of Kraut's calculation method for the considered measurements, because it does not account for possible band bending within the XPS probing depth. XPS and UPS have different probing depths: UPS probes only the surface (< 2 nm), whereas XPS probes not only the surface but also the bulk (< 5 nm). This is evident in the discussed UPS and XPS data, where already after 3 cycles no presence of the a-Si:H bulk was detectable for the UPS valence band spectra whereas in the XPS measurements, the Si $2p$ peak is observed up to 40 cycles. Additionally, for the first deposition cycles, the shift in core level positions for Sn $3d$ and Si $2p$ was the most drastic. These shifts correspond to the increased band bending at the interface. However, when

probing the interface after the first cycles, with XPS and UPS different depths are sampled. Both methods provide data that is exponentially averaged over the probing depth. However, due to the small inelastic mean free path of UPS photoelectrons, the valence band position is sampled only in the first few monolayers, whereas XPS averages over a few nm. Thus, if there is a pronounced band bending present within this probing depth, an average core level position is obtained, whereas the valence band edge position corresponds to the state at the surface. As was established earlier, there are pronounced changes in band bending with increasing number of ALD cycles, starting already at the first cycle. Therefore, it is not possible to exactly determine the band offset for the first cycles. The offset for the a-Si:H/SnO₂ interface can be estimated only beyond the space-charge region, where no changes in offset will occur due to the band bending. After 20-40 cycles, where the SnO₂ layer can be considered as fully formed, with no presence of substoichiometric species, but with a detectable presence of the Si 2p signal, the valence band offset is calculated to 2.23±0.2 eV. Due to the mentioned limitations of Kraut's method, this value includes an eventual band bending in the SnO₂ film towards the SnO₂/Si interface.

Similarly, the conduction band offset ΔE_c can be estimated, as:

$$\Delta E_c = E_{g_{SnO_2}} - E_{g_{Si}} - \Delta E_v, \quad (4.3)$$

Where E_g is the bandgap of the corresponding material and ΔE_v is the valence band offset. Like the valence band offset, the conduction band offset decreases with layer growth, from 1.19±0.3 eV after 3 deposition cycles to 0.55±0.1 eV after 40 deposition cycles, due to included band bending at the interface. Note that in addition to the previously discussed limitations for valence band offset calculation, for the conduction band offset an additional source of error is introduced by the ambiguity of the bandgap during the first deposition cycles, due to formation of SiO_x and substoichiometric SnO_x layers.

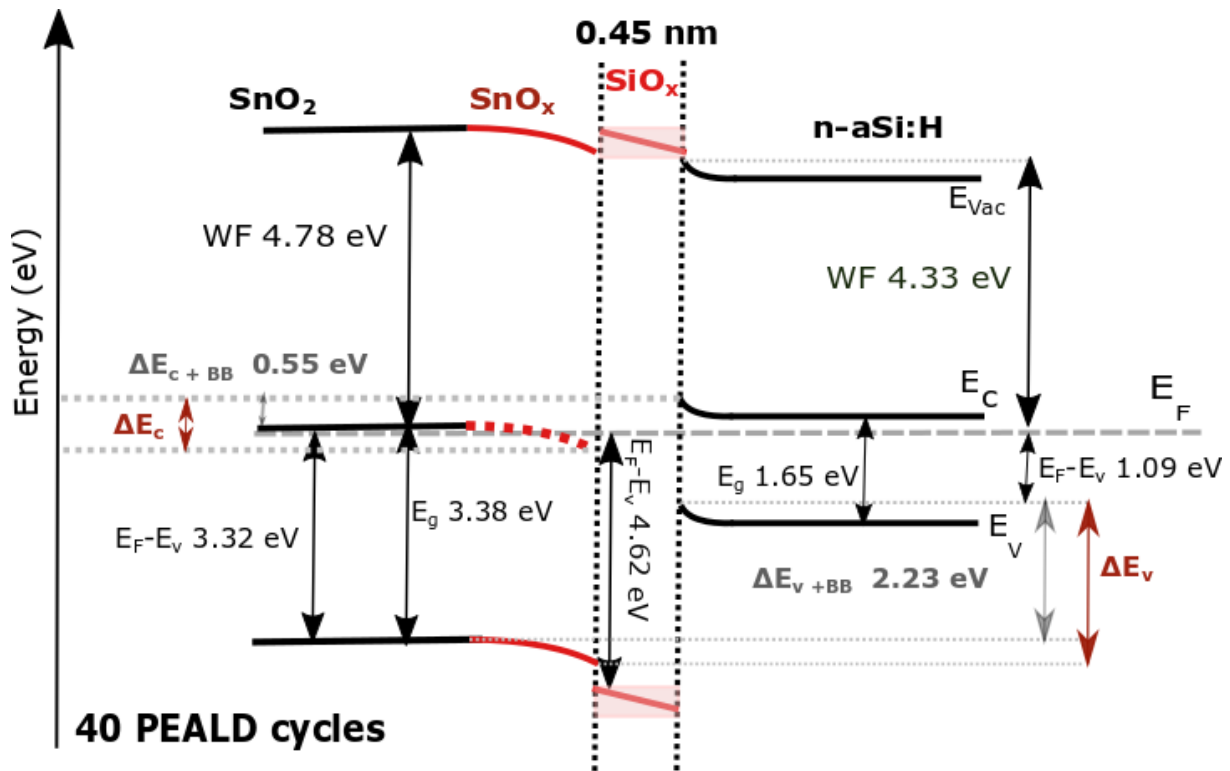


Figure 4.20: Sketch of the band line-up of SnO₂/n-aSi:H interface after 40 ALD cycles with the inclusion of the intermediate SiO_x layer. The red color indicates the intermediate SiO_x and SnO_x regions. The shaded area indicates uncertainties in the vacuum level and valence band of SiO_x region.

A schematic representation of the SnO₂/n-aSi:H heterojunction after 40 deposition cycles is shown in fig. 4.20. The region in red indicates the space-charge region, which includes the intermediate SiO_x and SnO_x layers. The SiO_x region presents most uncertainties at this interface, especially with the position of the conduction band, due to unknown bandgap that can differ from the stoichiometric SiO₂ layer. From the shift of Si 2p core level during the first deposition cycles towards lower binding energies, it can be assumed that intermediate SnO_x is negatively charged. Thus, an additional upwards band bending in the n-aSi:H layers is induced. With the further growth and formation of a stoichiometric SnO₂, the interfacial fixed charge is lost and the offset decreases. For the fully formed stoichiometric SnO₂ layer after 40 cycles, the film is thicker than the width of the space charge region. Thus, the conduction and valence band offsets calculated with Kraut's method disregard the band bending at the interface, and thus

underestimate the value for the valence band offset and overestimate the value for the conduction band offset.

4.5 Implementation of PEALD SnO₂ layers in SHJ devices

PEALD SnO₂ layers were tested in SHJ solar cells as part of the electron contact and as a possible replacement for the TCO (ITO) at the rear side. Thus, the first step was to perform TLM measurements for the SnO₂ layer in combination with different metallization stacks. TLM test structures consisted of 15 nm PEALD SnO₂/ 5 nm i-aSi:H/c-Si layer stack, on top of which metal grid with different metal stacks was evaporated.

Contact layer stack	$\rho_c, \Omega\text{cm}^2$	ρ_c after annealing, Ωcm^2
SnO ₂ /Ag	0.06-0.1	n/a*
SnO ₂ /Ti-Ag	n/a**	0.1-0.15
SnO ₂ /Al	39.61*	12.41*

*poor contact linearity, **scattered data

Table 4.1: Contact resistivity (ρ_c) for SnO₂ layers with different metal stacks.

Table 4.1 shows the extracted results for contact resistivity from the TLM measurements for the different layer stack systems: as-deposited, and after a 5 minute annealing step at 200 °C. For the as-deposited state, the SnO₂/Ag layer stack showed a decent contact resistance below 100 m Ωcm^2 . However, after the annealing step, no data could be extracted due non linearity of the IV curves, which impeded the application of the TLM method. At the same time, the Ti-Ag metal stack showed a superior contact resistance after the annealing step, despite the fact that no data could be extracted for this stack in the as-deposited state. Finally, the SnO₂/Al stack was highly resistive, and yielded non-linear current-voltage curves both after the deposition and after annealing. Therefore, only Ti/Ag or Ag metallization stacks can be considered for the interface with SnO₂. However, due to the poor lateral conductivity of these layers (regarded layers had $\rho \approx 180 \Omega\text{cm}$), their implementation as a single rear side TCO in solar cells could be problematic. The investigated solar cells that had a standard front layer stack (p,i-aSi:H layers) and the rear n-aSi:H/SnO₂ (15-30 nm)/Ti-Ag layer stack showed very poor output parameters

and efficiencies below 5 % (not presented here). Therefore, on the rear side, ITO in the solar cell must still be used.

SnO ₂ ALD cycles	J _{sc} , mA/cm ²	V _{oc} , V	FF, %	η, %	Rs, Ωcm ²
0	31.6	0.690	70.3	15.4	2.9
25	31.4	0.680	66.0	14.1	4.73
50	31.6	0.684	67.3	14.5	4.33
75	32.3	0.681	63.9	14.1	5.14

Table 4.2: Parameters of the best solar cells on planar wafers with a varied SnO₂ layers thickness.

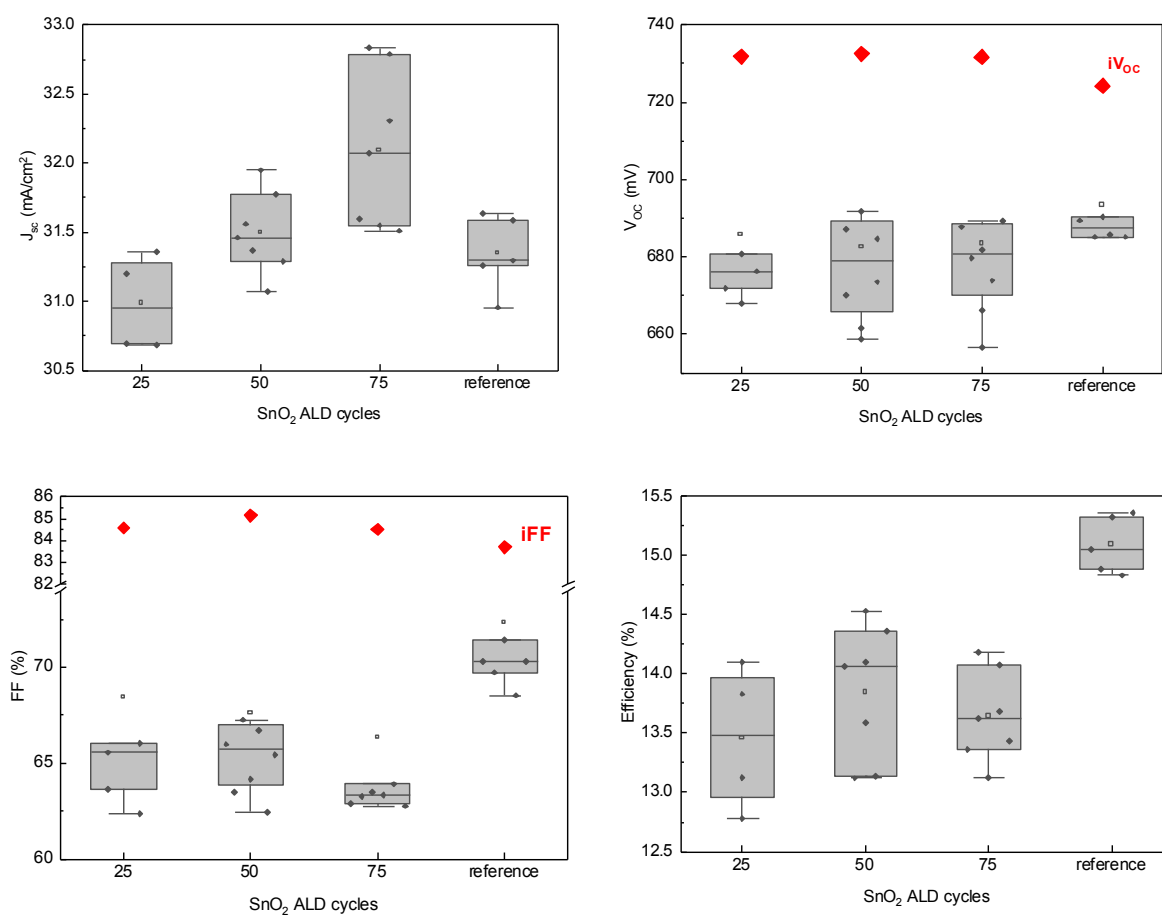


Figure 4.21: Solar cell parameters for device with a varied SnO₂ layer thickness. iV_{oc} and iFF values extracted from TrPCD measurements, before the metallization step.

Thus, SHJ solar devices with a rear structure consisting of i-aSi:H/n-aSi:H/SnO₂/ITO/Ti-Ag with varied SnO₂ layer thicknesses were fabricated on planar c-Si wafers. The parameters of these cells are presented in fig 4.21 and table 4.2. Additionally, the series resistances for all samples were calculated from Suns-Voc measurements. The reference cell shows reduced parameters, due to overly thick i-aSi:H layer (6.5 nm) and not fully optimized p-aSi:H layer. However, the addition of a thin SnO₂ layer causes a slight drop and scatter in V_{OC} and a drop in the fill factor, of more than 6 % already for the thinnest SnO₂ layer. The inclusion of SnO₂ layers drastically increases R_S, which can explain the drop in fill factor with increasing layer thickness. Slight drop and increased scatter of the V_{OC} values could be associated with possible sputter damage of the layer stack during the ITO deposition, or formation of the defective SiO_x layer at the interface between n-aSi:H and SnO₂ layers, which was discussed in the previous sections.

4.6 Tin oxide layers for perovskite solar cells

4.6.1 Introduction

So far, the main focus of this thesis was on SHJ solar cells. However, perovskite solar cells have achieved drastic increases in efficiency and stability in the span of the last several years, such that they can be now regarded as one of the promising routes for future solar cell development. Perovskite refers to crystalline materials with a perovskite-type structure with an ABX₃ formula. For perovskites used in photovoltaics, A is a monovalent and often organic cation (such methylammonium, formamidinium or cesium), B is a metal (usually lead or tin), and X is a halogen (iodine, bromine or chlorine) [195]. Planar perovskite devices are typically classified, according to the arrangement of precedent electron, or hole-transport layer, as either n-i-p (regular) or p-i-n (inverted) contact stacks, depending on the deposition sequences, where a perovskite film serves as the absorber [196]. The most recent record power conversion efficiency (PCE) for a single junction perovskite solar cell was above 24% [197]. Having already achieved such prominent results, one of the further developments for perovskite cells is their combination, as a top sub-cell, with other solar cell concepts to form tandem cells. This would allow these tandems to surpass the Shockley-Queisser limit for single-junction solar cells. By now, there are prominent results for perovskite-silicon [198] and perovskite-CIGSe [199] tandem solar cells.

However, despite recent impressive progress in the development of perovskite solar cells, this technology is still far from ready for commercialization in the next years. The main limitations and roadblocks in the development of such devices include poor photo- and thermal stability, the presence of hysteretic behaviour in cell performance [200], and concerns regarding the presence of lead [201].

The development of perovskite solar cells has been derived from research in organic solar cells. Therefore, a lot of effort has been dedicated to the development of different organic materials and metal oxides for use as carrier-selective contacts and TCOs, respectively. For the hole-selective contacts, organic materials such as spiro-OMeTAD or PTAA are often used, as well as metal oxides like MoO₃ or NiO_x [202]. Recently, self-assembling monolayer contacts have also been used for this purpose [203].

For electron-selective contacts the most commonly used layers are PCBM, TiO₂ and SnO₂, due to their good band alignment towards the perovskite interface [204]. The main functions of electron-selective contact layers are to have an optimal band alignment with the perovskite layer for electron transport, and to reduce the presence of surface defects and therefore mitigate losses at the interface. A recurring problem for perovskite solar cells is a hysteresis behaviour in the JV curves for the solar cells. If the electron contact leads to an accumulation of charge, there is a drastic increase in hysteresis. However, if the charge can be easily extracted at the interface, the hysteresis can be decreased or even eliminated [205].

By now, the most common electron-transport layers in perovskite solar cell are organic materials, or metal oxide layers. However, metal oxide layers show more advantages in terms of cost and long-term stability, in comparison to organic materials. More research is concentrated nowadays on SnO₂ layers, due to their higher conductivity, better band alignment, wider bandgap and excellent transparency, compared to TiO₂ [206], and better chemical stability in comparison to ZnO.

There is a variety of different methods used for the deposition of tin oxide in perovskite solar cells, such as spin-coating, sol gel, e-beam evaporation or ALD. The main criteria for layer deposition is to have high scalability and to have low deposition temperatures.

Spin-coating is one of the most used deposition methods for layers in perovskite solar cells, due to its simplicity, low cost and low deposition temperature. For this, an appropriate precursor solution, which for SnO₂ could be SnCl₄ in isopropyl alcohol or a SnCl₂·2H₂O solution in

ethanol, is used. Spin-coated tin oxide is widely used material for perovskite solar cells. However, solar cells with as deposited SnO₂ layers exhibit reduced efficiencies or device stability [207]. One possible reason is an improper band-alignment between as deposited tin oxide and perovskite layers. Additionally, deposition by spin-coating often results in poor coverage and/or porous SnO₂ layers, which can cause efficiency losses [208].

To prevent these issues, post-treatments of the layers after deposition have to be considered. The most common post-treatment techniques are ozone treatments [209] and annealing of the layer [208]. Another option is to treat spin-coated layers with an oxygen plasma at elevated temperatures, which is explored in this thesis. Thus, in the next section, the oxygen plasma treatment of spin-coated SnO₂ layers is introduced and its influence on layer properties and device performance will be discussed.

4.6.2 Oxygen plasma post-treatments for spin-coated SnO₂ layers

A study of post-treatment procedures for spin-coated SnO₂ films was conducted by Philipp Tockhorn and the author of this thesis. P. Tockhorn deposited SnO₂ layers and produced perovskite solar cells. The author of this thesis designed and optimized an oxygen plasma post-treatment process, and additionally measured and analyzed XPS and UPS data for the as deposited and oxygen plasma treated layers.

The developed plasma post-treatment procedure was carried out in a PECVD chamber at AltaCVD deposition tool by Altatech, with a plasma power density of 50 mW/cm², 0.5 mbar pressure, oxygen gas flow of 15 sccm and a process temperature of 180 °C. This temperature has an additional annealing effect on the SnO₂ layers, which improves their conductivity and was found to be optimal for the functionality of SnO₂ films as electron transport layers [210]. The described post-treatment process was applied for spin-coated SnO₂ layers with layer thicknesses of 20-25 nm deposited on ITO/glass substrates for solar cells and XPS/UPS measurements, and on flat c-Si wafers for ellipsometry measurements and XPS measurements. The investigated layers were deposited from a SnCl₂·2H₂O solution. Layer thickness was obtained via ellipsometry measurements, using a Drude-Lorentz model for fitting.

The main step for the implementation of the post-treatment was to find the optimal duration of the plasma step, and how it influences layer structure and solar cell performance. Thus, the duration of the post-treatment was varied as the main optimization parameter. This is especially

important due to the etching of the exposed material during the plasma step. Fig. 4.22 shows how the thickness of a spin-coated SnO₂ layer decreases with varied plasma duration steps. For a short plasma step of 30 seconds, up to 3% of the SnO₂ layer is removed, which means that mostly the film surface is etched away. However, with further increases in plasma duration, the change in layer thickness reaches up to 13%. This indicates that, with a longer post-treatment process, the layer bulk starts to be etched. Thus, it is possible that with the longer plasma exposure step plasma-induced damage occurs in tin oxide layer, which would create additional recombination centers [114], [211].

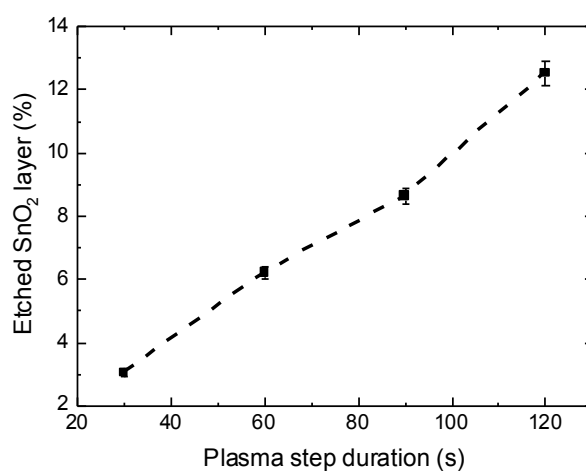


Figure 4.22: Relative reduction in thickness of SnO₂ layer during the plasma post-treatment step.

In order to monitor changes in layer properties with the post-treatment step, XPS and UPS measurements were performed. The core level XPS spectra of spin-coated SnO₂ layers were fitted with the same procedure as in the previous sections for the PEALD SnO₂ layers.

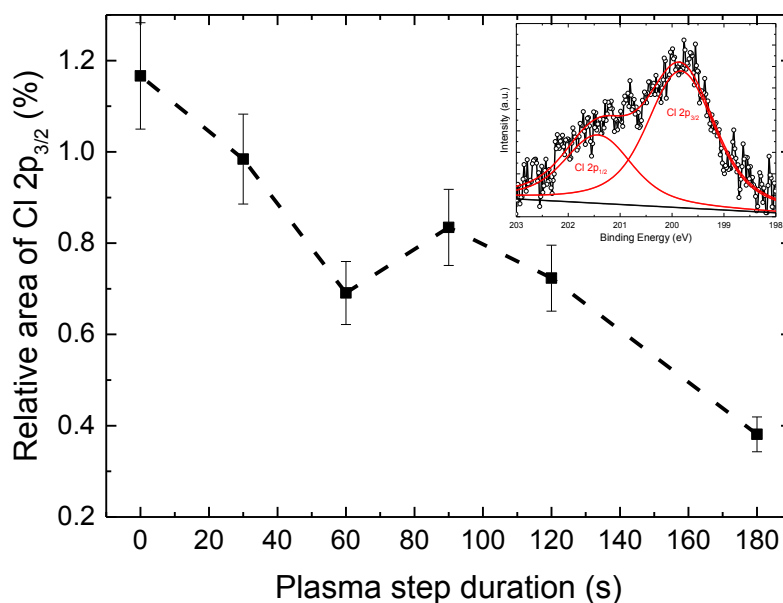


Figure 4.23: Area of the Cl 2p_{3/2} core level signal, relative to the total area of all main core levels for spin-coated SnO₂ layers (i.e. Sn 4d_{3/2}, O 1s, C 1s, Cl 2p_{3/2}), as a function of oxygen plasma step duration. The inset shows an example of raw data and fit for Cl 2p core level.

The main difference in the XPS spectra for spin-coated tin oxide layers, in comparison to the previously discussed PEALD SnO₂ layers, is a detectable Cl 2p core level signal at a binding energy of around 199.7-200.0 eV. This signal originates from the residuals of the SnCl₂ precursor salt used for the spin-coating deposition process. Fig. 4.23 shows the evolution of the Cl 2p_{3/2} XPS signal with increasing duration of the oxygen plasma post-treatment. It can be seen that for the as deposited SnO₂ oxide layer, there is a high concentration of chlorine, which steadily decreases with plasma treatment duration. However, even after the longest investigated plasma step of 180 seconds, there is still a detectable Cl 2p core level signal. At this point of the plasma post-treatment, more than 10 % of the layer has been etched away. Therefore, it is possible to conclude that for spin-coated SnO₂ layers chlorine is present, not only as a surface contaminant, but also incorporated into the bulk.

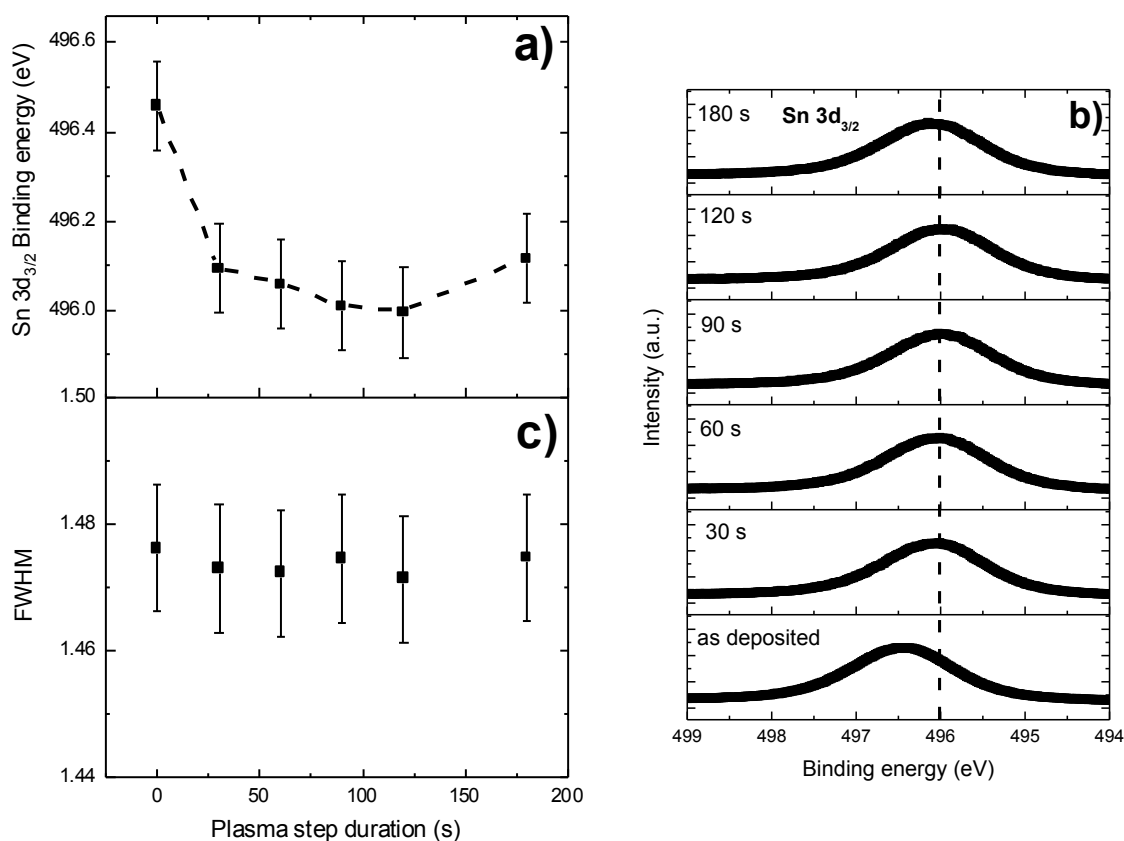


Figure 4.24: a) peak position of Sn 3d_{3/2} core level, b) evolution of the raw data of Sn 3d_{3/2} core level after varied oxygen plasma treatment step, referenced to C 1s core level positions. Spectra are offset for better visibility. c) FWHM of the fitted peak for Sn 3d_{3/2} core level

In order to check for the presence of additional signals in Sn 3d_{3/2} core level, the fit for all signals was done with one peak, with FWHM as a fitting parameter. The change in FWHM would indicate the presence of additional signal in the core level. However, as it is seen from fig. 4.24 c, there are no noticeable changes in FWHM for any sample. Thus, all spin-coated layers, both as-deposited and after the post-treatment step, showed no detectable presence of the Sn²⁺ oxidation state. However, already with the shortest plasma treatment process of 30 seconds, there is an observable shift of around 0.4-0.5 eV for the core level energy, as it is shown in fig 4.24 a,b. The oxidation state of Sn within the bulk remains unchanged with the plasma treatment, thus it can be assumed that the shift in the core level is caused by charging of SnO₂ layers upon the plasma treatment.

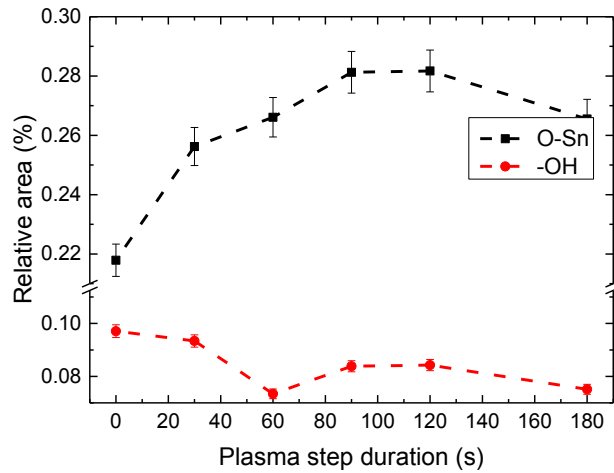


Figure 4.25: Area of the O 1s core level signal, relative to the total area contributed by all main core levels for spin-coated SnO₂ layers (Sn 4d_{3/2}, O 1s, C 1s, Cl 2p_{3/2}) as a function of oxygen plasma step duration.

Additionally, with the plasma post-treatments changes in the O 1s core level signal could be observed, as shown in fig. 4.25. The O 1s core level was fitted with two components, the main peak that corresponds to the O-Sn bond, and a second one that represents -OH groups. With an increased plasma duration, the signal that corresponds to the O-Sn bond continually increases until saturation at around 90 seconds. At the same time, the -OH signal steadily decreases. This behaviour indicates that the surface and the bulk of SnO₂ layers are oxidized during the plasma step.

Another important point is to identify the influence of the oxygen plasma on the surface of the spin-coated SnO₂ layer. Fig. 4.26 illustrates the evolution of the valence band edge and secondary cut-off region of the UPS spectra for the investigated layers, with varied oxygen plasma step duration. Both regions are strongly affected by the applied oxygen plasma treatment. With increasing oxygen plasma duration, the valence band edge moves towards lower binding energies. Thus, the value changes from 3.29±0.2 eV for as deposited samples, which is comparable to values obtained for PEALD SnO₂ layers, to 2.59±0.2 eV after 180 seconds of oxygen plasma step.

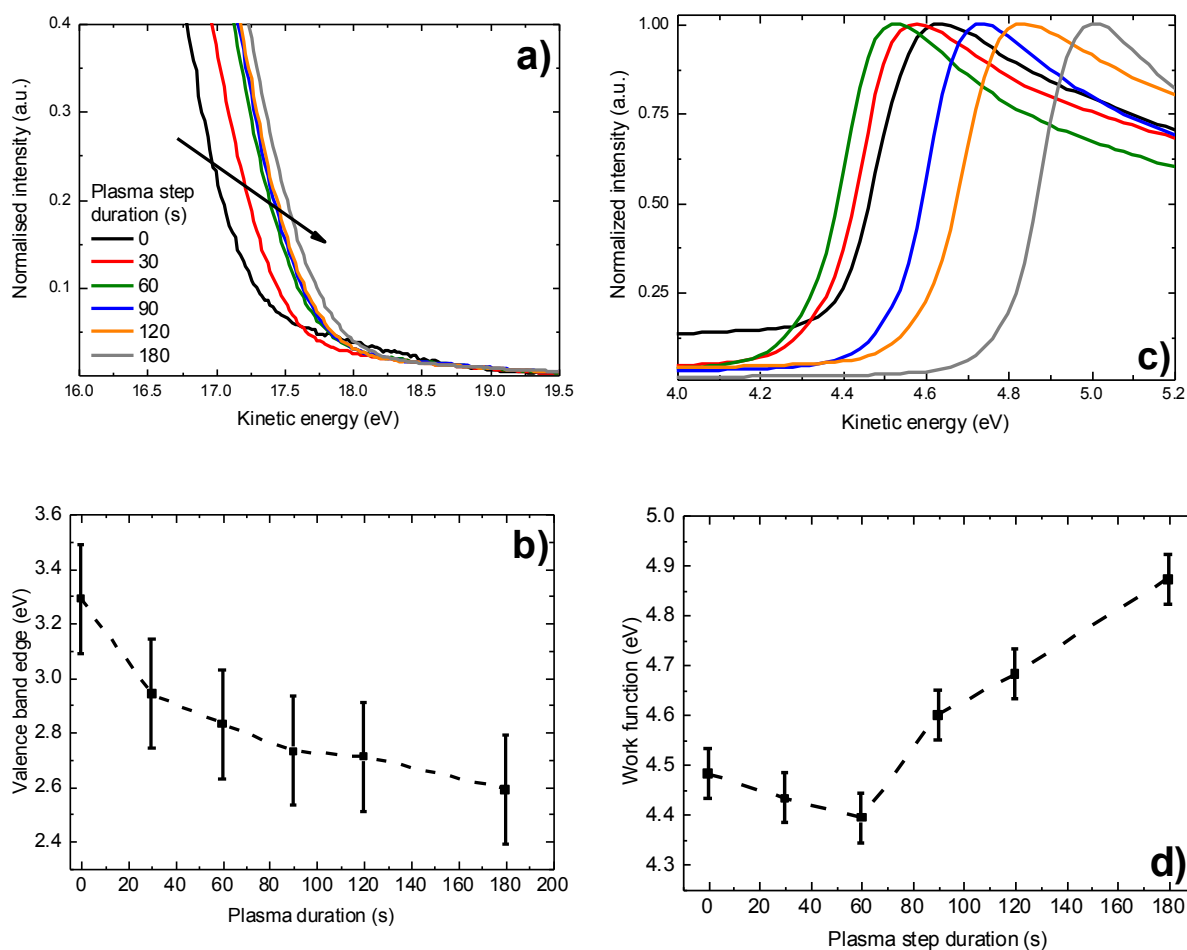


Figure 4.26: UPS spectra of spin-coated SnO₂ layers after oxygen plasma step of varied duration: a) valence band region after satellite spectra extraction (chapter 3.2.1.2), b) evolution of the valence band edge with plasma duration, c) secondary cut-off of the UPS spectra with normalized signal intensity, d) evolution of work function with plasma duration.

Additionally, the shape of the curve changes already after a short plasma step of 30 seconds. For the untreated sample, there is an additional feature at low binding energies of 2-4 eV, which is possibly characteristic to Sn 5s surface states and would indicate the presence of the Sn²⁺ oxidation state [188]. While fitting the XPS data, the Sn 4d core level signal did not exhibit any detectable presence of Sn²⁺. Therefore, it is possible to conclude that the reduced states are present only at the surface and, by applying the plasma post-treatment, the surface is oxidized and reduced states are lost.

Additionally, it is possible to observe changes in the cut-off region for the investigated layers. Within a short plasma step, the work function is slightly reduced in comparison to the untreated

sample. However with a longer step, an increase in the work function from the initial 4.48 ± 0.05 eV to 4.87 ± 0.05 eV after 180 seconds of oxygen plasma step can be observed. This increase can be caused by the further oxidation of the surface and reduction of surface species, such as chlorine, or -OH groups.

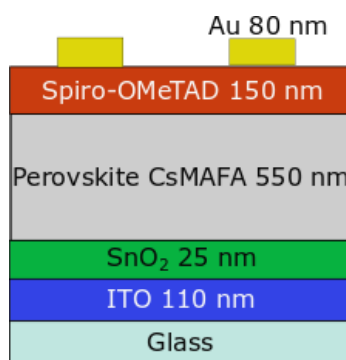


Figure 4.27: Schematic representation of the investigated perovskite solar cell structure.

The next step is to compare the performance of the perovskite solar cells with oxygen plasma post-treatment steps of varied duration. Thus, inverted perovskite solar cells were investigated, with a layers structure, as shown in fig 4.27. For these cells, 25 nm of SnO₂ layer is deposited at the rear side of the cell on top of glass substrates coated with 110 nm of patterned ITO. Such deposition sequence allows to have oxygen plasma post-treatment step and to exclude damage to the absorber, due to oxygen and elevated temperature exposure. Subsequently, “triple cation” $\text{Cs}_{0.05}(\text{FA}_{0.83}\text{MA}_{0.17})_{0.95}\text{Pb}(\text{I}_{0.83}\text{Br}_{0.17})_3$ (CsMAFA) perovskite absorber is deposited. Afterwards, 150 nm of Spiro-OMeTAD layer, as hole-selective contact are spin-coated. Finally, 80 nm layer of gold grid was thermally evaporated.

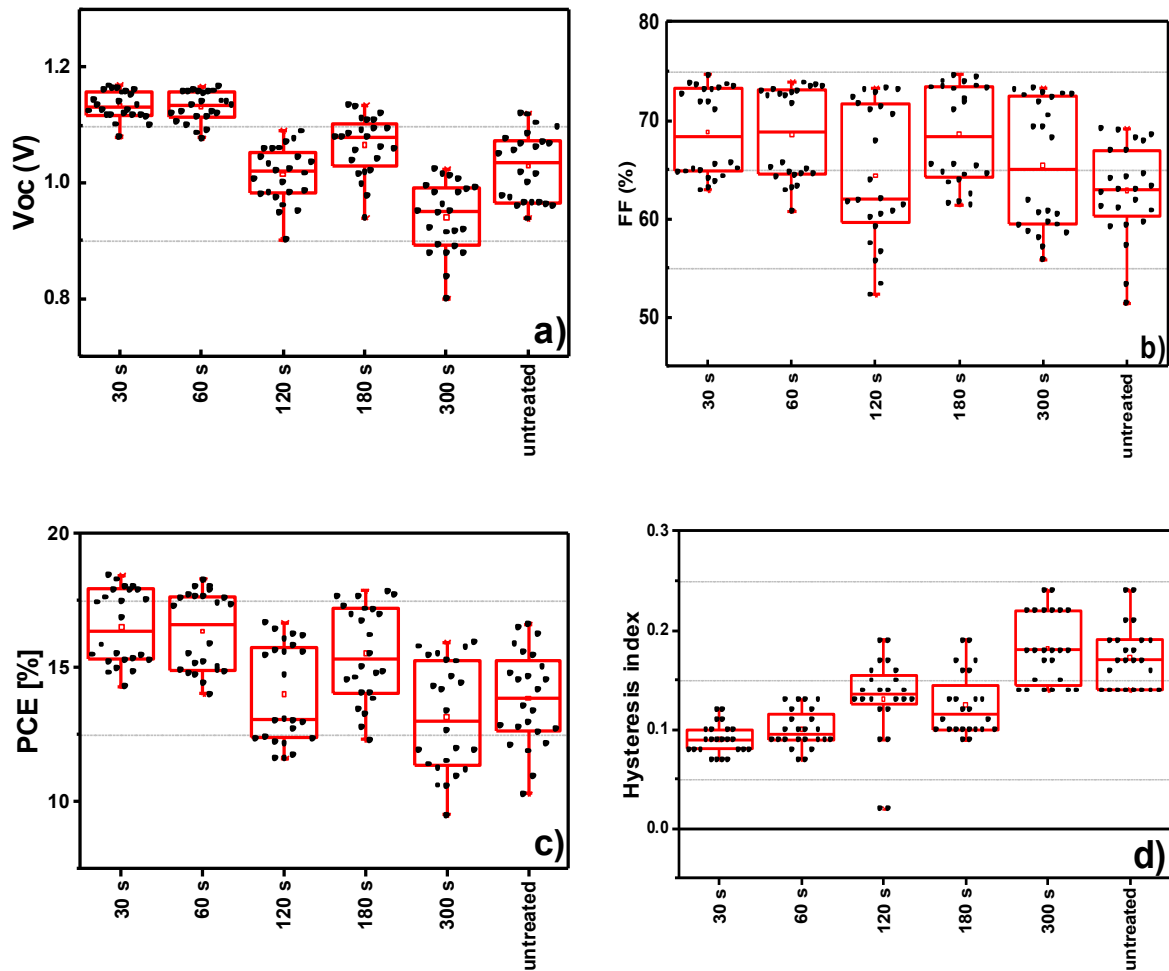


Figure 4.28: a) V_{OC} , b) FF c) power conversion efficiency and d) hysteresis index for perovskite solar cell with varied plasma step duration.

Fig. 4.28 shows the main output parameters and a schematic representation of the investigated devices. It can be seen, for a short plasma step of 30-60 seconds, there is a clear improvement in V_{OC} , which leads to increased solar cell efficiencies. Additionally, this short plasma step yields a noticeably decreased hysteresis index, which is extracted from comparing forward and reverse IV curve scans [207]. However, with further increase in the post-treatment duration, the performance of solar cell degrades. A possible explanation for this behaviour is that, because of the short plasma step, the top defective contaminated surface layer is etched and the surface is oxidized without plasma-induced damage. Therefore, the passivation is improved. However, with longer plasma step durations, more of the layer is etched off and then the surface roughness and induced defects from oxygen plasma might increase, which could then lead to the decreased V_{OC} . Moreover, the observed increase of the fill factor and decreased hysteresis index for the

short oxygen plasma step can be assigned to the improved band alignment between SnO₂ and perovskite layer.

The straightforward way to estimate the band offset is by applying Schokley-Anderson model, which is a simplistic representation of the heterojunction interface and does not include the interface dipole. The bandgap of CsMAFA layer is 1.6 eV, work function is 4.7 eV and valence band edge is at 0.9 eV below the Fermi level [199]. From the ellipsometry measurements the extracted bandgap of spin-coated tin oxide is 3.5 eV. Thus, by applying Schockley-Anderson model (chapter 2.2.1) and using the valence band edge and work function of spin-coated SnO₂ layers (fig 4.26 b, d) , the conduction band offset can be estimated, and its evolution over oxygen plasma step time is shown in fig 4.29.

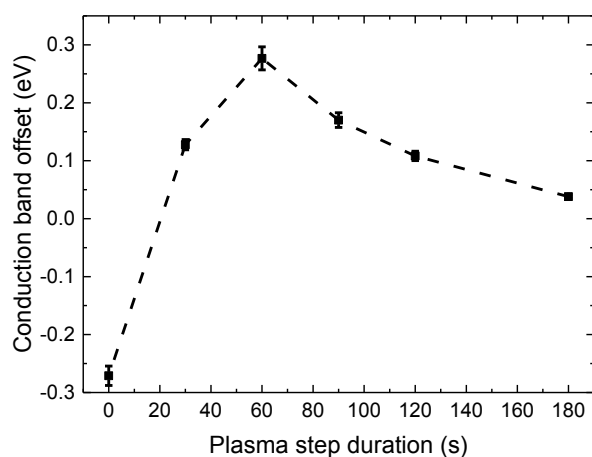


Figure 4.29: Calculated band offset for the SnO₂/CSMAFA interface, as a function of oxygen plasma treatment duration.

Within the shortest oxygen plasma treatment process, the conduction band offset is decreased, which is indicated the improved electron selectivity in the interface. However, with assuming Anderson model, it can be seen that even for the longer plasma duration the conduction band offset is steadily decreasing, which does not correspond to the observed hysteresis index behavior for long treatment that can indicate charge accumulutaion at the interface. The reason is not fully clear, however, it can be assumed that upon a longer plasma treatment time, the Schockley-Anderson model is no longer valid, due to the creation of the dipole at the interface

upon long plasma exposure that was seen with the increase of the work function after 60 s oxygen plasma step (fig. 4.26 d).

Additionally, the performance of the perovskite solar cells with SnO₂ layers was also compared for different post-deposition treatments. For the ozone treatment, the spin-coated SnO₂ layers were exposed to UV-ozone for 30 minutes at room temperature. This treatment would also oxidize and clean the surface of the layer. The reference sample, “annealed”, was only subjected to an annealing step at 180 °C.

<i>Treatment</i>	<i>J_{sc} (mA/cm²)</i>	<i>V_{oc} (V)</i>	<i>FF (%)</i>	<i>PCE (%)</i>
<i>Annealed</i>	20.9	1.15	75.8	16.4
<i>Ozone</i>	20.5	1.13	69.5	14.1
<i>Plasma (30 s)</i>	21.1	1.17	77.9	18.1

Table 4.3: Best perovskite solar cell performance with different SnO₂ layer post-deposition treatments

Table 4.3 shows solar cell characteristics for best perovskite solar cells with just annealed, ozone and short plasma (30 seconds) treated SnO₂ layers. It can be seen that the solar cell with the ozone treated SnO₂ layer shows a reduced V_{OC}, FF and PCE, even in comparison to the device with only annealed SnO₂. Much lower FF of the device for ozone treated layer can be attributed to the possible misalignment between perovskite layer and SnO₂, due to which a carrier barrier is likely formed. Another important parameter is V_{OC}. From the XPS measurements, the ozone treated sample behaved similarly to the oxygen plasma treated ones, showing an increase in O-Sn bonds and an oxidation of the surface in comparison to the as-deposited sample. However, unlike the oxygen plasma treated layers, no Cl 2p core level signal was detectable from XPS.

Therefore, it is possible to conclude that after the ozone treatment, chlorine is removed from the layer surface and bulk. However, chlorine can be beneficial for the perovskite passivation, as it was shown for both chlorine terminated TiO₂ [212] and SnO₂ [213] layer surfaces for perovskite solar cell. It was reported that chlorine termination on TiO₂ and SnO₂ surfaces can suppress the defect formation in the perovskite, upon its deposition and thereby reduce interface recombination. In comparison to the oxygen plasma treatment, in which is chlorine was present even after the long plasma step and can be assumed to be present at the surface of the film, the

surface of ozone treated layers exhibits no presence of these species. Thus, the passivation at the interface is decreased, which is reflected in the solar cell performance.

4.7 Chapter summary

This chapter presented a detailed investigation of a PEALD process for SnO₂ layers, from the process optimization to device implementation of the layers and discussed post-treatment of spin-coated SnO₂ layers for perovskite solar cell.

In the first part, optical and electrical properties of SnO₂ layers deposited using TDMASn as a precursor and oxygen plasma in the deposition temperature range of 90-210 °C were investigated. The PEALD cycle optimization for this process was discussed, and three sets of layers were investigated in detail: one based on the initial non-optimized process, the other on the final optimized process. For the third sample set starting from the optimal process, the oxygen pulse time was varied. The influence of deposition parameters on optical and electrical properties was investigated, and XPS measurements were conducted to connect these macroscopic layer properties with the layer composition. It was shown that, in all layers deposited with PEALD, residual carbon and nitrogen are present that can be assigned to residuals from not fully reacted precursor molecules. These contaminations, which decrease with deposition temperature, have a direct influence on the refractive index and optical band gap of the SnO₂ layers. Additionally, a shoulder in the O 1s core level spectrum at higher binding energy is indicative of -OH and/or carboxyl groups present in the film or at its surface. It was shown that, with increasing deposition temperature, there is a decrease in this high-binding energy O 1s signal. Assuming that most of this signal can indeed be attributed to -OH groups, its thermally induced decrease could be interpreted as a dehydroxylation of the SnO₂ layers. Additionally, the stoichiometry of the layers with deposition temperature was investigated. It was observed that, at deposition temperatures above 165 °C, the layers contain more substoichiometric species, which may partially contribute to the bandgap variation.

Moreover, the influence of deposition temperature on the electrical properties of SnO₂ layers was investigated. The layer resistivity changes drastically, by up to five orders of magnitude, with varying deposition temperatures from 90 °C to 210 °C. However, there is no direct simple dependence between layer resistivity and composition. Presumably, the high inclusion of precursor residues leads to high resistivity. However, low residue concentrations do not

necessarily lead to low resistivity. Thus, it is likely that other factors (like layer topography and crystallinity) become dominant in this composition regime.

The second part of this chapter is focused on understanding the formation of the SnO₂/n-aSi:H interface throughout the different stages of SnO₂ growth using PEALD, starting from thin incubation layers up to a full stoichiometric SnO₂ overlayer. For this interface, no growth delay was observed, and the Sn 3d core level signal was detectable at the surface already after the first PEALD cycle. However, it was seen that, after the first 1-3 cycles, intermediate understoichiometric silicon oxide was formed. Moreover, during the first 10 cycles, the intermediate substoichiometric tin oxide is deposited, with the present Sn²⁺ oxidation state was observed. The apparent conduction band offset at the SnO₂/n-aSi:H interface is decreasing with increasing SnO₂ layer thickness and is estimated as 0.55±0.15 eV after 40 ALD cycles. However, this value represents not only the offset between the fully formed SnO₂ layer and the n-aSi:H bulk, but also includes the band bending in the SnO₂ film towards the interface, and not the direct interface. Even though the fully formed ALD SnO₂ layer does not cause an additional upwards band bending at the interface with n-aSi:H substrate as compared to the free n-aSi:H surface, the conduction band offset is still too high to consider SnO₂ as a part for the electron contact for a silicon based device.

The calculated conduction band offset for this interface is substantially higher than for other n-type wide gap semiconductors, such as ZnO (200 meV) [192]. Additionally, SnO₂ layers deposited by PEALD have a high work function of around 4.82 eV, which is problematic for the electron contact. Therefore, as-deposited PEALD SnO₂ layers are not suitable to function as electron transport layers in SHJ based devices. Nevertheless, SHJ devices with the implementation of this interface were presented. Solar cell with c-Si/i-aSi:H/n-aSi:H/SnO₂/ITO layer stack showed a high drop in fill factor in comparison with the reference device, which may be due to the formation of a potential barrier at the interface, according to presented XPS/UPS results and due to series resistance of these cells, which was drastically increased by the addition of SnO₂ layers, which also contributed to the decrease in fill factor. Therefore, PEALD SnO₂ layers are not suitable for use in SHJ devices. Post-treatment procedures for these layers might be considered in order to decrease the offset between SnO₂ and aSi:H layers, which is beyond the scope of this thesis.

The final section of this chapter was dedicated to the post-treatment procedures for the spin-coated layers, with the focus of their implementation in perovskite solar cells. Within this

section, the oxygen plasma post-treatment process for spin-coated SnO₂ layers is introduced as an effective method to improve the surface of SnO₂ layers and interface between SnO₂ and the perovskite layers. Thus, XPS and UPS measurements were carried out for layers after varied oxygen plasma treatment time and these results were further correlated with the solar cell performance.

The main difference between PEALD and spin-coated SnO₂ layers was the detectable signal of Cl 2p in the XPS spectra that originates from the salt precursor for spin-coating. Upon oxygen plasma treatment, the intensity of Cl signal was steadily decreasing, but even after the longest investigated step this signal was detectable. Additionally, amount of O-Sn bonds drastically increased until the saturation at around 90 s of the post-treatment. This indicates that upon oxygen plasma treatment, SnO₂ surface was oxidized. Moreover, with the prolonged oxygen plasma treatment the valence band edge shifted towards Fermi level. At the same time, high increase of the work function occurred upon the oxygen plasma treatment step above 60 s, with 4.48 ± 0.05 eV for as-deposited sample, to 4.87 ± 0.05 eV after plasma step of 180 s. This led to the changes at the interface between SnO₂ and perovskite layer, which were mirrored in the solar cell performance. It was observed that due to the improved conduction band alignment between SnO₂ layer and the perovskite, fill factor and hysteresis index for solar cell were improved after the short plasma treatment step. As a result, it was possible by the short oxygen plasma treatment step of 30 seconds to improve PCE of the solar cell by 10 % relative, due to increased FF and V_{OC} of the solar cell.

Chapter 5

Magnesium oxide as a passivating electron-selective contact for silicon heterojunction solar cells

5.1 Introduction

Magnesium oxide has a work function of 4.2 eV [214], which makes it a suitable material for the electron contact in c-Si based devices [6]. Recently, the successful implementation of MgO thin layers as stand-alone passivation and electron transport layers on n-type c-Si wafers [12], [60], [61], and in combination with aluminum oxide as a ternary oxide ($\text{Al}_x\text{Mg}_{1-x}\text{O}_y$), as a passivation layer for p-type c-Si wafers [62] have been shown. Devices with 1-2 nm thin MgO electron-selective contacts, prepared by e-beam or thermal evaporation, have been reported. These devices showed moderate improvement of the passivation with MgO layer as compared to the bare c-Si wafer and had a good contact resistance in the range of 18-40 $\text{m}\Omega\text{cm}^2$ for a MgO thickness of ~ 1 nm. The main issue with implementing MgO layers is a trade-off between passivation and contact resistance: by increasing the MgO layer thickness it is possible to achieve higher passivation quality, but at the same time the contact resistance increases drastically, due to the insulating nature of the MgO layers. Therefore, an optimal thickness has to be established with high precision. Additionally, it is possible to introduce a buffer layer, such as i-aSi:H, in order to optimize the passivation of the solar cell. In common deposition techniques such as chemical beam deposition [215], metal-organic chemical vapor deposition [216], [217] or chemical vapor deposition [218], the growth of MgO layers demands high deposition temperatures. In order to decrease the deposition temperature without sacrificing layer properties, ALD can be regarded. ALD is shown to be a suitable deposition method, especially for low work function metal oxides layers in solar cells. Therefore, the applicability of ALD MgO layers for devices is an important topic to address.

The following chapter outlines the optimization of an ALD process for magnesium oxide (MgO) layers using Bis(ethylcyclopentadienyl)magnesium ($\text{Mg}(\text{CpEt})_2$) and is partially based on the accepted publication in IEEE Journal of Photovoltaics.

The considered precursor was shown to be suitable for the growth of high quality MgO layers for ALD processes using water as the oxidizing agent, at the deposition temperature range of 125-200 °C [219]. Such an ALD process for MgO thin film deposition was investigated, with a focus on obtaining well-passivated interfaces for MgO/c-Si and MgO/i-aSi:H/c-Si layer stacks.

The first section of this chapter focuses on the ALD process optimization and the chemical characteristics of MgO layers.

The second section discusses the passivation properties and contact resistance for MgO/c-Si and MgO/i-aSi:H/c-Si layer stacks, with varying thickness of the MgO layer. Additionally, a post-treatment annealing step and its influence on the layer stack is discussed. Furthermore, this section presents and discusses results obtained for SHJ solar cell devices implementing both types of layer stacks with varied layer thicknesses.

The sections that follow discuss the further optimization of SHJ solar cells with MgO layers. First, MgO layer properties and solar cell properties for various MgO layer deposition temperatures and the influence of an annealing step on layer properties are investigated. Afterwards, different possible metallization schemes are analyzed and the thermal stability of the SHJ solar cells with MgO layers is addressed.

5.2 Optimization of the ALD process and MgO layer properties

5.2.1 Optimization of the ALD cycle

MgO films were deposited by thermal atomic layer deposition in an Arradiance GEMStar XT 6-8 ALD reactor. Mg(CpEt)₂ was used as a precursor and was held at a temperature of 80 °C in the stainless steel bubbler. N₂ as the carrier gas and water as the reactant were applied. The default temperature for the cycle optimization was set at 150 °C, as this is an optimal temperature for layer deposition [219]. As a first step, the precursor and water step durations were optimized for the ALD cycle.

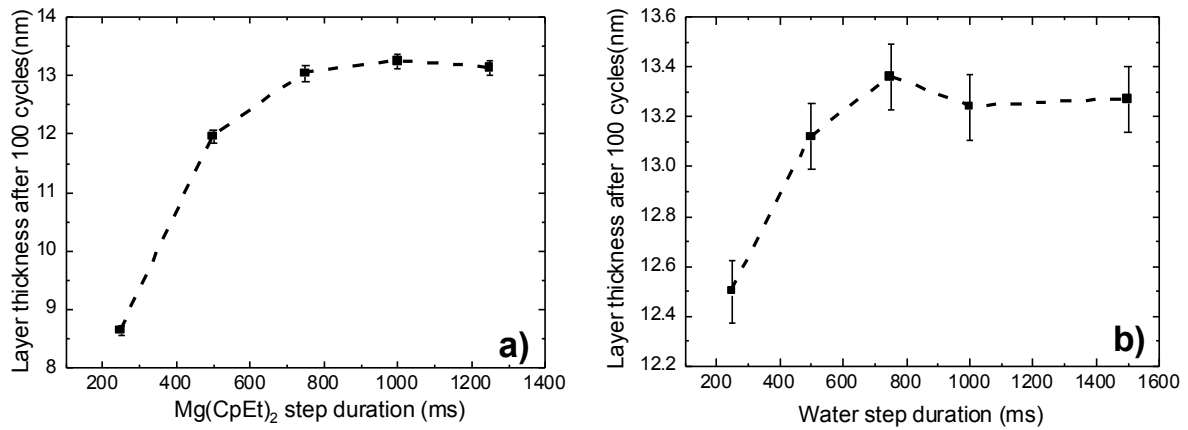


Figure 5.1: MgO layer thickness after 100 deposition cycles as a function of a) Mg(CpEt)₂ and b) water step durations.

For each variation in step duration, MgO layers after 100 ALD cycles were deposited on HF-treated c-Si substrates. The results of these variations are presented in fig. 5.1. It can be seen that for the Mg(CpEt)₂ step duration of around 800-1000 ms, there is no change in the deposition rate, thus the growth rate saturates. For the oxidizer step, the growth rate also saturates in a comparable time range. Hereby, the standard deposition cycle for MgO layers in this thesis consists of a 1 second pulse of Mg(CpEt)₂, 10 s of first purge step with N₂, a 750 ms water pulse, and a 10 s second purge with N₂.

5.2.2 Growth of MgO layers on c-Si and i-aSi:H/c-Si substrates

The next step was to evaluate the growth behavior of ALD MgO layers on c-Si and 5 nm thick i-aSi:H/c-Si substrates. As shown in fig. 5.2, there is a linear dependence of film growth with increasing number of ALD cycles with a very slight delay. The linear fits cross the abscissa at around 4 cycles for the series on c-Si and at 7 cycles for i-aSi:H. In case of the i-aSi:H substrate, the delay is higher, due to surface passivation by silicon-hydrogen bonds, which possibly hinders the nucleation of the layer at Si surface dangling bonds during the first cycles of the deposition process [220]. Additionally, no growth on glass substrates was observed, which could possibly indicate a low reactivity of Mg(CpEt)₂ precursor with the surface groups of the glass substrate.

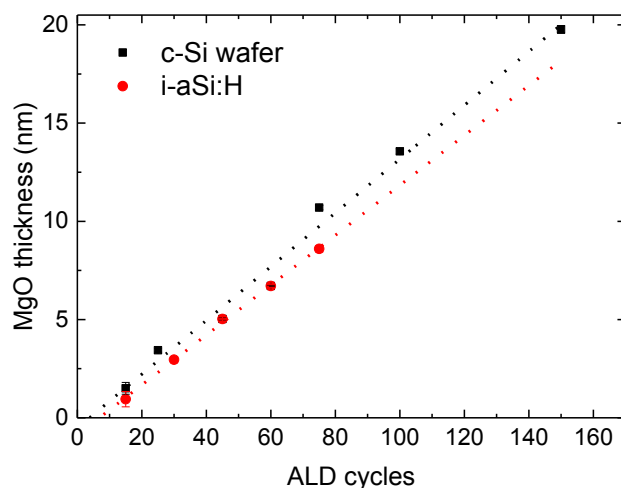


Figure 5.2: Film thickness of MgO layers on HF- dipped c-Si wafers (black) and on i-aSi:H layers on c-Si (red), as a function of the number of ALD cycles. The deposition temperature was set at 150 °C.

5.2.3 Changes in layer composition with air exposure

Next, the chemical composition of the deposited layers and the effects of air exposure were evaluated. As discussed in chapter 2.1.3, magnesium oxide is known for hydrogen accumulation and adsorbing water at the surface [66], [221]. Therefore, it is important to compare air-exposed with as-prepared samples to identify changes at the surface and in the bulk. To this end, two MgO layers with thickness of 10 nm were deposited at 150 °C on c-Si wafers. Afterwards, one of the samples (“exposed”) was subjected to ambient air for about one hour, before being introduced to the UHV XPS System. The second sample (“clean”) was directly transferred to the UHV system through nitrogen-filled gloveboxes, without exposure to ambient air. Therefore, additional contamination could be excluded.

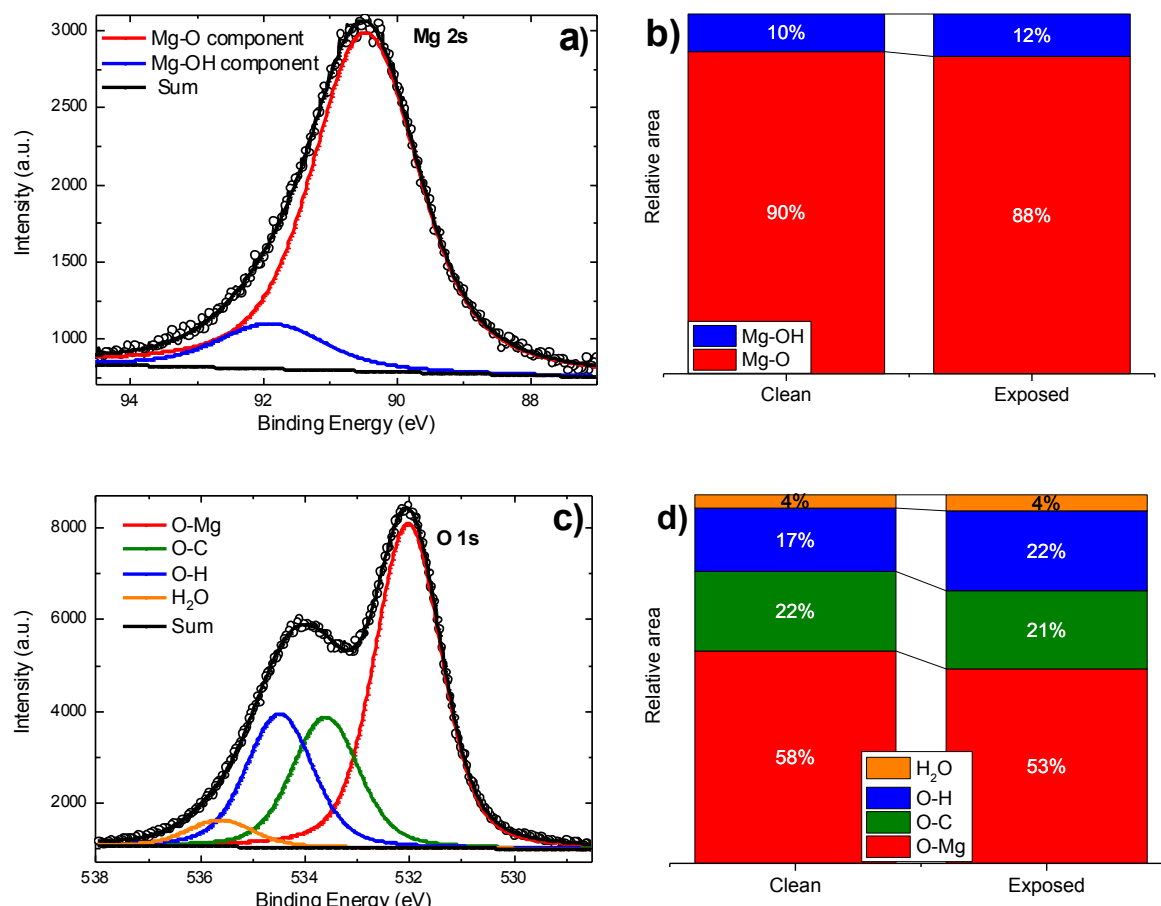


Figure 5.3: a) Fitting of the Mg 2s core level for the “exposed” sample. Circles represent the raw signal data, b) Relative area of the Mg-OH and Mg-O components of the Mg 2s core level signal for “clean” and “exposed” samples, c) Fitting of the O 1s core level for the “exposed” sample. d) Relative areas of the O 1s core level components for the “clean” and “exposed” samples.

Fig. 5.3 a and c show the Mg 2s and O 1s raw data and fitting of the core levels for the “exposed” sample. As shown in Fig 5.3 a, it is not possible to fit the Mg 2s core level using only 1 peak, the Mg-O bond. At higher binding energies, there is a strong contribution that can be attributed to Mg-OH bonds, which correspond to the presence of Mg(OH)₂ [222]. In fig. 5.3 b, the relative contributions of Mg-OH and Mg-O bonds to the Mg 2s core level for the “clean” and “exposed” samples are shown. It can be seen that even the “clean” sample has a high intensity for the Mg-OH bond component, which increases upon sample exposure to ambient air.

Another relevant core level is O 1s. As seen in fig. 5.3 c, the core level can be fitted with four component peaks, which are Mg-O at around 531.5 eV, a peak at around 533.5 eV that possibly

originated from C-O bonds in precursor residuals, a Mg-OH bond at around 534.5 eV and an H₂O peak at the highest binding energy of around 536 eV [223].

Figure 5.3 d shows a comparison between the O 1s core level compositions for the “clean” and “exposed” samples. Contamination residues assigned to C-O bonds and H₂O, remain at the same level. However, with exposure to ambient air the intensity of the peak assigned to O-H bonds increases, which correlates with the Mg 2s core level Mg-OH bond component. Therefore, it is possible to conclude that the deposited layers are not fully stoichiometric. Moreover, there is an accumulation of hydrogen and an increase of peroxide Mg(OH)₂ with air exposure.

5.3 MgO layer thickness variation

5.3.1 Passivation properties

The next important step is to investigate the passivation properties of ALD MgO layers with varying thickness. For this, samples with symmetrical layer stacks on both sides of the wafer were produced in order to investigate changes of the passivation quality in terms of minority carrier lifetime upon deposition of MgO layers. Minority carrier lifetime data was extracted at an injection level of 10^{15} cm^{-3} . The full lifetime vs. injection level data sets, $\tau(\Delta p)$, were further analyzed using a semi-analytical simulation model to separate the influence of field-effect passivation from defect passivation for the investigated layer stacks [147], [224]. A more detailed description of the simulation model is given in chapter 3.2.3.3.

With the direct deposition of a thin MgO layer (30 ALD cycles, $d \approx 3 \text{ nm}$) on c-Si substrates, no passivation was achieved, neither in the as-deposited state, nor after the annealing steps. However, for a thicker MgO layer, i.e. after 75 ALD cycles ($d_{\text{MgO}} \approx 9.8 \text{ nm}$), changes in the passivation quality were observed: Fig. 5.4.a shows the minority carrier lifetime for such a MgO layer deposited on a c-Si wafer. For the as-deposited stack no passivation was noticeable. However, after 5 minutes annealing at 200-250 °C, a slight passivation effect, yielding a lifetime of around 150 μs , is observed.

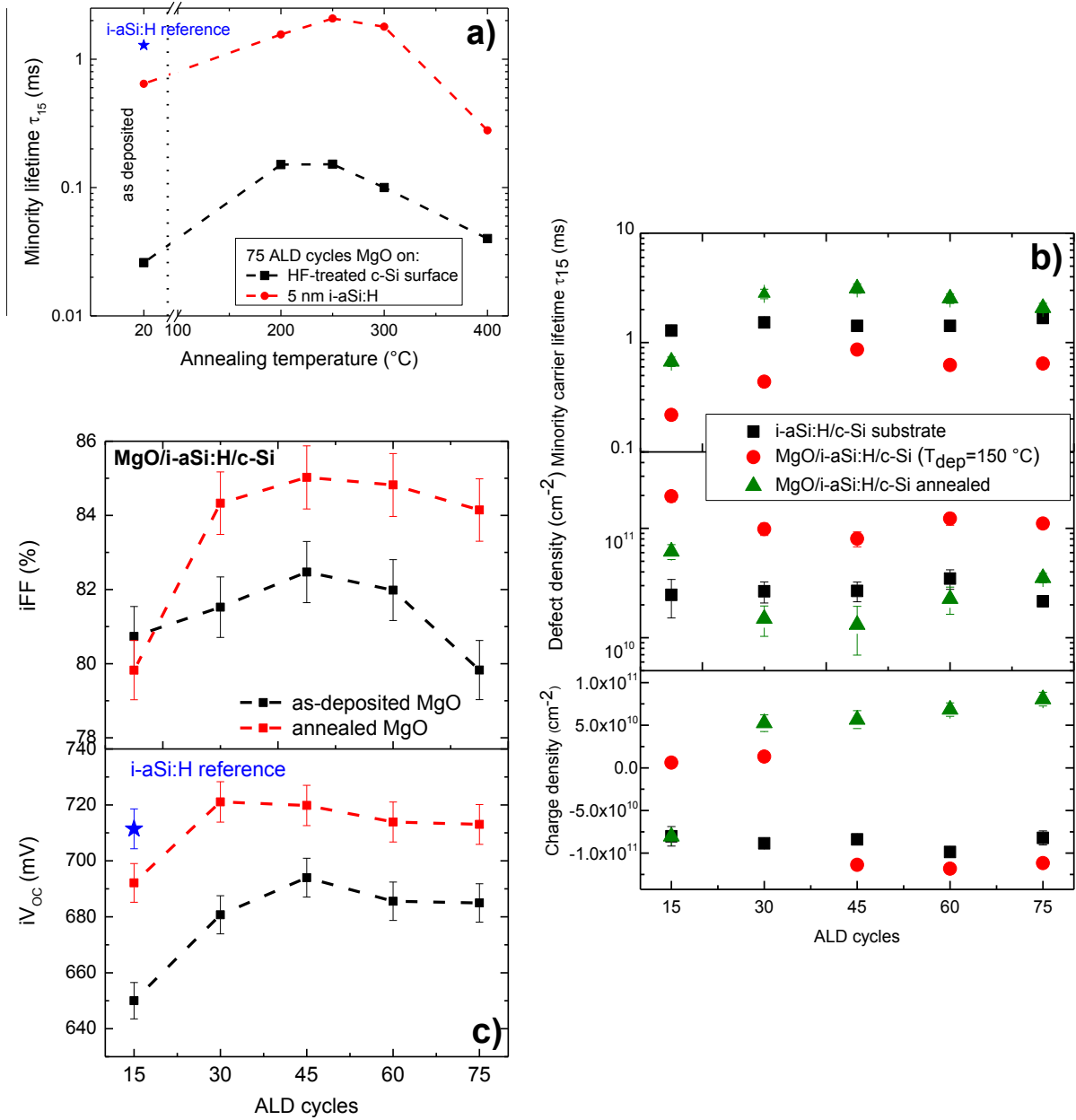


Figure 5.4: a) Effective excess minority carrier lifetime at 10^{15} cm^{-3} injection level after MgO layer deposition at $150 \text{ }^\circ\text{C}$ for the HF-treated c-Si wafer and i-aSi:H/MgO layer stacks on c-Si, as a function of the annealing temperature. b) Carrier lifetime at 10^{15} cm^{-3} injection level, modelled defect densities and effective charge, c) iFF and iV_{oc} for i-aSi:H/MgO layer stacks on c-Si substrates, as a function of the number of ALD deposition cycles.

A similar experiment was performed on MgO deposited on i-aSi:H coated c-Si substrates. For this, 5 nm i-aSi:H layers were deposited using PECVD with the process parameters described in chapter 3.1, prior to the ALD growth of the MgO layer. In this case, it was possible to observe significant changes in the effective lifetime with varying MgO thickness.

In the upper panel of fig. 5.4 b, the effective minority charge carrier lifetime for c-Si wafers coated with such layer stacks is shown as a function of the number of ALD cycles. After the initial deposition of MgO layer atop the i-aSi:H substrate, there is a noticeable degradation of the lifetime for all MgO layer thicknesses, which also correlates with iV_{OC} , as shown in fig. 5.4 c. From the analytical model fitting, it can be seen that the degradation is caused by the drastic increase in interface defect density (middle panel of fig. 5.4 b). However, similar to the MgO/c-Si layer stack, recovery and improvement in the passivation is observed after a 200 °C annealing step, with the maximum increase for the sample after 45 MgO ALD cycles, which also corresponds to the point with the lowest interface defect density. At the same time, the total effective charge slightly increases with the number of deposition cycles. Therefore, it is possible to conclude that the main c-Si interface passivation mechanism is that of chemical passivation by the i-aSi:H film, which degrades upon MgO deposition, then recovers during the annealing step. The existence of an optimal MgO layer thickness for the passivation is similar to results found for some other metal oxides, such as TiO₂ [225]. Furthermore, it is interesting to note that the fixed charge reverses its sign: while it is initially rather small and negative, $\sim -1 \times 10^{11}/\text{cm}^2$ after i-aSi:H deposition, it increases to $> +5 \times 10^{11}/\text{cm}^2$ after MgO deposition and anneal, for all MgO thicknesses except the thinnest (15 cycles). This indicates, that MgO/i-aSi:H stacks are indeed suitable as electron contact layers, since the positive fixed charge will lead to a downwards band bending and attract electrons at this contact.

It is not fully clear why the fixed charge changes its sign. It is possible that after 15 cycles, the MgO layer is not yet fully closed, and that the intermediate SiO_x is dominant. This oxide is formed at the interface between i-aSi:H and MgO layer therefore plays the main role for the values of D_{it} and the sign of Q_i . The formation of an intermediate SiO_x layer will be discussed in further sections.

As explained above, the annealing step is needed after the MgO layer deposition to improve the passivation quality by decreasing the defect density at the interface. Therefore, the next step is to optimize the annealing temperature in order to achieve the highest improvement of passivation. Fig. 5.4 a compares the minority carrier lifetimes as a function of annealing

temperature for both layer stacks. As expected, for the MgO/i-aSi:H layer stack, the minority carrier lifetime values decrease at annealing temperatures above 300 °C due to the degradation of the i-aSi:H layer caused by hydrogen effusion [226]. The MgO/c-Si layer stack shows a similar trend, with a nearly total degradation of the effective lifetime at annealing temperatures above 300 °C. Possible reasons for this degradation can be the breaking of Mg-OH bonds present in the layer and the partial recrystallization of MgO layer [227].

5.3.2 Contact resistivity of MgO layers

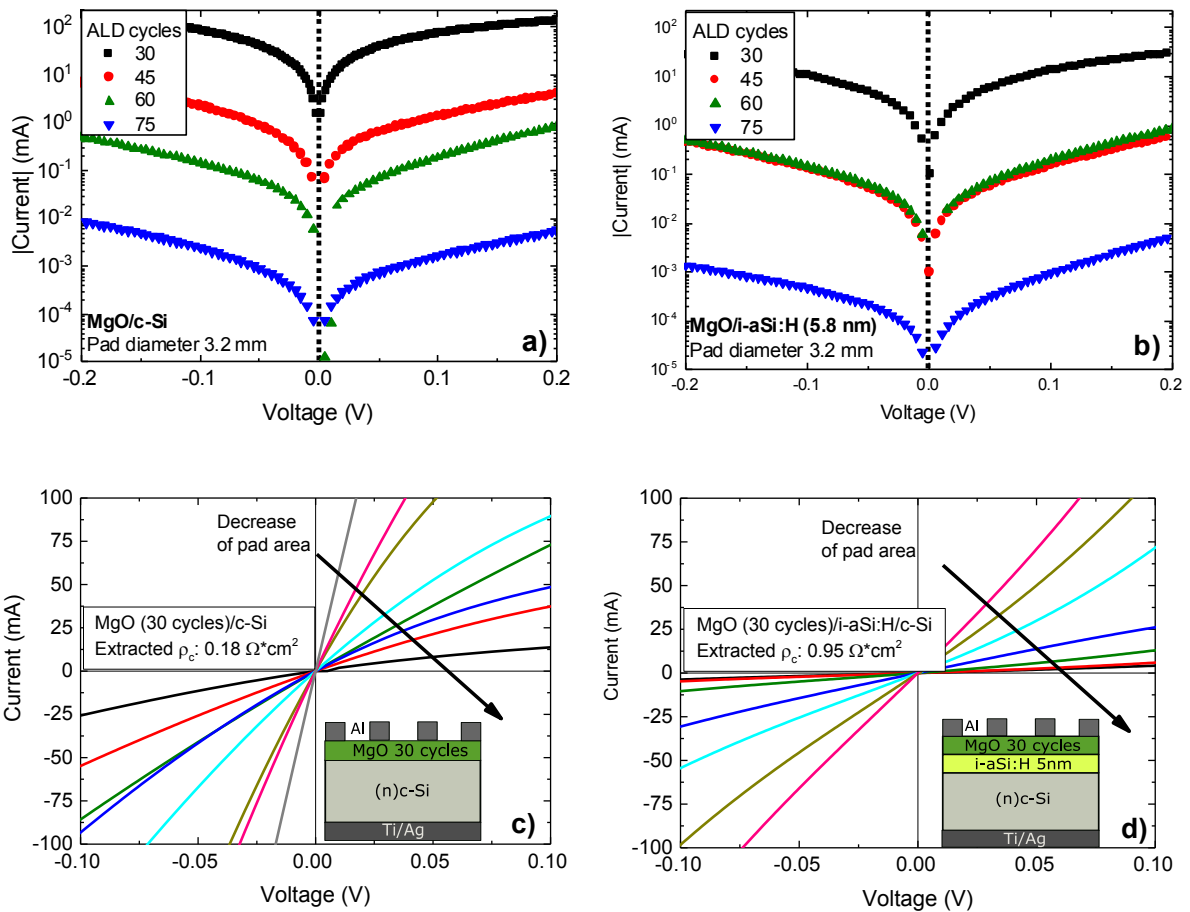


Figure 5.5: IV characteristics of Cox & Strack test structures for varying thicknesses of ALD MgO deposited at 150 °C on, a) c-Si substrates, and b) i-aSi:H/c-Si layer stacks. IV characteristics for varying pad diameters on the test structures after 30 cycles of MgO for, c) c-Si substrate, d) i-aSi:H/c-Si layer stacks. Samples were annealed at 250 °C before the metallization process, insets show schematics of the test structures.

The next point to evaluate is the contact properties of the MgO/c-Si and MgO/i-aSi:H/c-Si layer stacks. Therefore, test structures using the method devised by Cox and Strack, as described in chapter 3.2.5.2, were investigated [157]. At the front side, the corresponding contact stacks with MgO layers with different thicknesses were realized. On the rear side of the structure a 10 nm titanium/500 nm silver metal stack was thermally evaporated. This yields an Ohmic contact to the c-Si wafer and is assumed to contribute negligibly to the total resistance of the sample. As shown previously, the passivation of the c-Si substrate by such layer stacks can be improved by a short annealing step at 200-250 °C. Consequently, samples were annealed at 250 °C for 5 minutes before metallization. Afterwards, 2 µm thick circular aluminum pads of different sizes were evaporated onto the front side.

For both cases, i.e. with and without i-a-Si:H buffer layers, the IV characteristics had a linear, Ohmic behaviour as shown in fig. 5.5 c,d. On the other hand, it can be seen from fig. 5.5 a,b that with the increase of MgO layer thickness there is a drastic increase of resistance. The conduction band offset between the MgO layer and c-Si is around 1.55 eV [228]. The band offset between c-Si and i-aSi:H is around 0.2-0.3 eV [27]. Assuming the transitivity rule, which implies that three semiconductors A, B and C should combine in a predictable manner, and the band offset at A/B heterojunction can be deduced from band offset of the sum of A/C and C/B heterojunctions [229]. Thus, the conduction band offset between MgO and i-aSi:H is still expected to be around 1.25-1.35 eV. Such a barrier is considerably higher than the thermal energy $k_B T$. Thus, tunneling of electrons from the a-Si conduction band through the MgO to the metal contact is probably the main current transport mechanism, and an exponential scaling of resistance with barrier thickness is consistent with this argument. Therefore, this increase most likely corresponds to a dominant contribution of tunneling resistance [230]. With the increase of the layer thickness, the IV data become more scattered. Therefore, the contact resistivity for thicker layers could not be reliably determined from the thicker layers. As a result, in the following only data obtained from the test structures with 30 ALD cycles of MgO, for both cases, i.e. with and without i-aSi:H, is discussed.

For the MgO/c-Si stack the contact resistance of the structure is $0.18 \pm 0.01 \text{ } \Omega\text{cm}^2$, which is comparable to values reported by others for evaporated MgO layers with similar thicknesses [60]. For samples with i-aSi:H layer, the extracted contact resistance is drastically higher: $0.95 \pm 0.11 \text{ } \Omega\text{cm}^2$.

One of the possible reasons for such an increase in contact resistance can be due to the insertion of the i-aSi:H buffer layer itself. The lowly conductive i-aSi:H layer introduces an additional resistance in the current transport path through the contact stack, due to its bulk resistivity [231]. Indeed, the reference structure for the rear structure, Ti-Ag/ITO/n-aSi:H/i-aSi:H/c-Si, showed a total contact resistance of $1.1 \pm 0.15 \text{ } \Omega\text{cm}^2$, which is even higher than for the considered MgO/i-aSi:H/c-Si stack. Most of the contributions can be assigned to i-aSi:H layer resistivity, whereby the contribution of other layers in the stack are negligible. While calculating the contact resistance by the Cox and Strack method, the resistivity of the layer can be neglected, if the product $\rho * t$ is low, where t is the thickness of the layer (equation 3.11). However, in case of i-aSi:H and MgO layers, which are dielectric layers with $\rho \geq 10^6 \text{ } \Omega\text{cm}$, this value cannot be excluded. Thus, the presented calculated values represent the contact resistance with included resistivity of the layers. Another possible influence on the contact resistance values is the aluminum metallization at the front contact. The aluminum contact is shown to be suitable in combination with MgO material [60], which due to its low work function ($\sim 4 \text{ eV}$) should contribute to a more pronounced downward band bending. However, for very thin MgO layers, it is possible for aluminum to diffuse through the layer to the i-aSi:H interface. The interaction of Al with the a-Si:H layer produces p-type counterdoping [232] and as a result, yields an increase in the total contact resistance [233].

5.3.3 Devices with varying MgO thickness

Solar cells with MgO/c-Si and MgO/i-aSi:H/c-Si layer stacks as rear contacts were fabricated in order to explore the feasibility of implementing ALD MgO layers in devices and compared to the standard SHJ solar cell. The process flow for SHJ solar cells is described in chapter 3.1.4. For the cells with an MgO layer, the MgO layer thickness was varied in the range of 20-50 ALD cycles ($\approx 2\text{-}5 \text{ nm}$) to assess the influence of layer thickness on the final solar cell performance. Two types of solar cell structures were considered: They have different rear sides with either a direct c-Si/MgO contact or contain an i-aSi:H buffer layer, i.e. an c-Si/i-aSi:H/MgO layer stack. Both types of layer stacks received 5 minutes annealing at $200 \text{ } ^\circ\text{C}$ after the MgO layer deposition. One of the technological problems during the fabrication step of such cells is a possible parasitic deposition (under-deposition) of the MgO material on the other side of the wafer during the ALD process. This parasitic deposition can contaminate the front side with residuals from MgO layer deposition. In such cases, a degradation of solar cell parameters can

be observed, especially in the passivation. For standard SHJ solar cells, the p-aSi:H layer at the front is deposited after n-aSi:H layer. However, for SHJ cells with MgO layers, p-aSi:H layers were deposited first, in order to prevent a degradation in passivation due to the under-deposition. For structures with MgO layers, the rear side ITO was omitted, and the rear side metallization consisted of a blanket layer of 1 μm aluminum. Schematic representations of both types of stacks are shown in fig. 5.6 a,b.

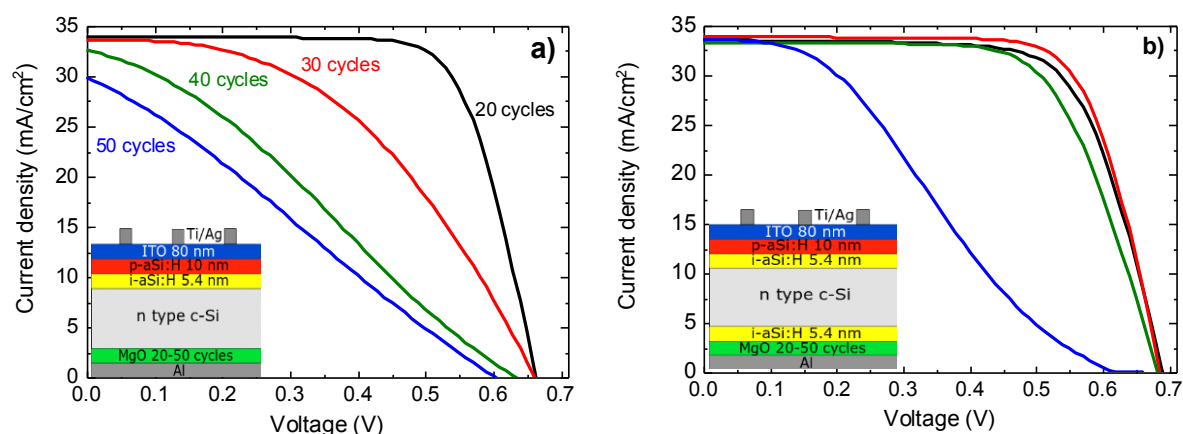


Figure 5.6: Illuminated one-sun JV characteristics of solar cell devices with rear electron contacts composed of a) MgO/c-Si layer stack, B) MgO/i-aSi:H/c-Si stacks. The MgO layer thicknesses were varied from 20 to 50 ALD cycles. The colors of the curves represent the same number of deposition cycles for both graphs. Schematic representations of the corresponding devices are shown as insets.

Contact stack	MgO cycles	J_{sc} (mA/cm^2)	V_{oc} (mV)	FF (%)	Efficiency (%)
MgO/c-Si	20	33.4	664	73.8	16.4
MgO/i-aSi:H	30	33.8	687	72.4	16.8
Reference (n,i-aSi:H)	0	33.3	698	73.4	17.0

Table 5.1. Solar cell parameters for the best devices fabricated on planar Si wafers incorporating the ALD-grown MgO layers.

The JV characteristics of such devices, with solar cell size of 1 cm² are shown in fig. 5.6. Additionally, table 5.1 shows the results for the best cell for each type of stack. Due to the flat surfaces on the c-Si wafers and shading by the front grid used for these cells, the short circuit current density is strongly limited.

For cells with the MgO/c-Si stack, an efficiency of 16.4 % is achieved with a thin MgO layer (20 ALD cycles, $d_{\text{MgO}} \approx 2.5$ nm). For comparison, a reference cell with an i,n-aSi:H/ITO contact has an efficiency of 17 %. From the Suns-V_{oc} measurements it was possible to extract series resistance for cells with MgO layer after 20 and 30 cycles. For the thinnest MgO layer after 20 cycles, the series resistance in the cell is $2.5 \pm 0.2 \text{ } \Omega\text{cm}^2$. However, already after 30 deposition cycles, the series resistance increases to $5.45 \pm 0.3 \text{ } \Omega\text{cm}^2$. With a further increase in layer thickness, the formation of a transport barrier is observed, which is reflected in the S-shape of JV curves (fig.5.6) and in a decrease of V_{oc} and FF. This degradation is consistent with the increasing contact resistance that was discussed earlier.

For the MgO/i-aSi:H/c-Si stack, it is obvious that the additional thin i-aSi:H layer helped to keep the passivation on a level that allows V_{oc} above 680 mV for devices with MgO layers. This shows that the i-aSi:H layer can sustain the passivation, and that a thin layer of MgO is sufficient to function as an electron transport layer. Moreover, the V_{oc} of the solar cell with the layer stack with included i-aSi:H layer corresponds to the passivation behavior discussed in chapter 5.3.1, where the optimal thickness for the highest iFF and iV_{oc} is found for 30-45 ALD cycles. For the best device, after 30 deposition cycles and with output parameters presented in table 5.1, the series resistance is $2.39 \pm 0.15 \text{ } \Omega\text{cm}^2$. The slight degradation of the V_{oc} and FF for such stacks as compared to the reference can probably be attributed to the diffusion of aluminum through the MgO stack during the evaporation of the aluminum contact, and potential parasitic under-deposition of MgO contaminants at the front side of the wafer.

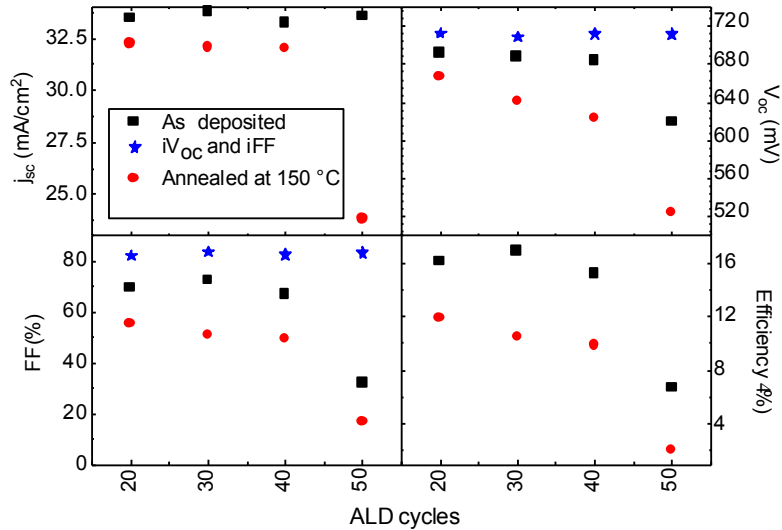


Figure 5.7: Parameters of best solar cells with (i-aSi:H/MgO/Al) stack as the rear side contact as deposited and after an annealing step of 3 minutes at 150 °C.

However, despite having acceptable device parameters these cells with Al metal contacts showed high thermal instability. In fig 5.7, the cell parameters for devices with MgO/i-aSi:H layer stacks are shown before and after an annealing step at 150 °C. It can be seen, that for all thicknesses, there is a drastic degradation in solar cell performance, which is especially prominent for the thickest MgO layer after 50 cycles. At the same time, iV_{OC} and iFF for layer stacks before the metallization, were comparable for all investigated MgO thicknesses. It is not fully clear, why the degradation is especially prevalent for the device with the thickest layer. However, it can be proposed that with Al diffusion into the MgO layer, the ternary $Al_xMg_{1-x}O_y$ may be formed. Such layer would result in high negative effective charge density [62], which would be detrimental to both passivation and fill factor of the cell. Therefore, further optimization of the layer stack, and metallization should be considered. A possible replacement for the metal contact is discussed in the following sections.

5.4 Magnesium oxide layers at varied deposition temperatures

5.4.1 Dependence of MgO layers passivation quality on deposition temperature

Another important parameter to consider is the deposition temperature for the MgO layers. The temperature window for the MgO ALD process is $\sim 125\text{-}200\text{ }^{\circ}\text{C}$ [219]. Therefore, in this temperature range, the highest precursor utilization during the deposition process can be expected. However, the interface properties and surface contamination can vary for different deposition conditions.

The starting point is to investigate the variation of passivation properties for the MgO/i-aSi:H layer stack with a varying deposition temperature of the MgO layers. Similarly to the previous section, samples with symmetrical layer stacks on both sides of the wafer were produced in order to investigate changes of the passivation quality in terms of minority carrier lifetime upon deposition of MgO layers. For these samples, 5 nm i-aSi:H layers were deposited using PECVD with the process parameters described in chapter 3.1, prior to the ALD growth of the MgO layer. Afterwards, MgO layers after 45 ALD cycles at varied deposition temperatures were deposited. No changes in the GPC with deposition temperature were observed, and the layers had comparable thicknesses ($\approx 4.5\text{ nm}$). Minority carrier lifetime data was extracted at an injection level of 10^{15} cm^{-3} . The full lifetime vs. injection level data sets, $\tau(\Delta p)$, were further analyzed using a semi-analytical simulation model to separate the influence of field-effect passivation from defect passivation for the investigated layer stacks [147], [224]. A more detailed description of the simulation model is given in chapter 3.2.3.3.

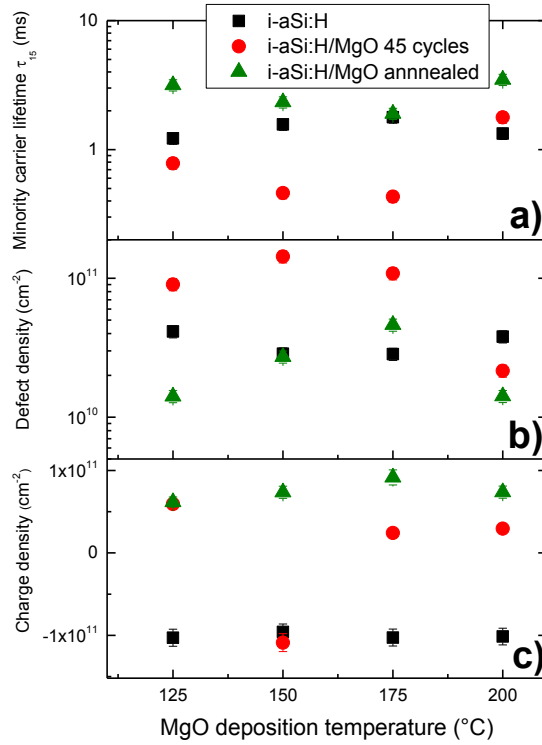


Figure 5.8: (a) Effective excess minority carrier lifetimes at a 10^{15} cm^{-3} injection level, (b) c-Si interface defect density, (c) fixed charge density after 45 cycles of MgO layer deposition on 5 nm i-aSi:H/c-Si, as a function of deposition temperature before and after annealing (5 minutes, at 250 °C).

Fig. 5.8 a shows the effective excess minority carrier lifetime for MgO/i-aSi:H/c-Si structures as a function of MgO deposition temperature for as-deposited samples, as well as after an annealing step of 5 minutes at 250 °C. For samples deposited at a temperature below 200 °C the minority carrier lifetime drastically degrades after the initial MgO layer growth. In contrast, the sample deposited at 200 °C shows an improvement that can probably be attributed to hydrogen diffusion in i-aSi:H, upon annealing during the ALD process. All lifetimes could be recovered or improved by a short annealing step at 250 °C. Interestingly, lifetimes are highest after annealing for the lowest and highest ALD temperatures, whereas for the a-Si:H/c-Si samples, i.e. prior to MgO deposition, the lifetime minimum is at a deposition temperature of 175 °C, which corresponds to the maximum defect density, as shown in fig 5.11 (panel b). Similarly to samples investigated in chapter 5.3, annealing step at 250 °C improved the passivation, and the interface defect density was decreased for samples at all deposition temperatures, especially for low deposition temperatures, of 125-150 °C. It can be assumed that this improvement occurs due to a reduction of the surface contamination of MgO layer surface

by the residuals of precursor, and layers becoming more stoichiometric. These assumptions will be discussed in a further section, based on XPS measurements for such layers stacks.

Additionally, for deposition temperatures of 175-200 °C, the initial fixed charge sign changes already after a direct deposition and it remains the same after the annealing step. However, for all samples after the annealing, the charge sign is positive, and values are comparable for all samples. Thus, all layers investigated in this temperature range are suitable to be electron-transport layers for SHJ solar cells.

5.4.2 XPS analysis of MgO layers deposited at different temperatures

To shed light on the physical mechanisms behind the dependence of passivation on deposition temperature and annealing, it is important to identify changes at the MgO/c-Si interface upon MgO layer deposition and after the annealing step. Therefore, MgO/i-aSi:H/c-Si samples were prepared for XPS investigations: thin layers of around 3 nm MgO (30 ALD cycles) were deposited on top of an i-aSi:H layer at temperatures in the range of 150-200 °C. Such thin MgO layers allow the observation of X-ray excited photoelectrons not only from the MgO film, but also from the underlying i-aSi:H layer. At the same time, such MgO film thickness is relevant for the applications in devices.

Samples were transported from the deposition tool to the XPS system through N₂ gloveboxes, without exposure to ambient air. All samples were measured as-deposited and then annealed in vacuum at 200 °C for 5 minutes.

The first peak to start the XPS analysis with is the C 1s core level signal. This signal could be fitted with two components: A peak assigned to C-H bonds at a binding energy around 287 eV, and a peak stemming from C-O groups at 289 eV [223], as illustrated in fig. 5.9 a. In fig. 5.9 b, the areas of the C-H and C-O bonds relative to the total area of the main core level signals are shown. The carbon concentration changes for different deposition temperatures: the relative area for both bonds decreases with the deposition temperature, and decreases further after annealing. However, for the sample deposited at 200 °C, the C-O signal is increased in comparison to the other deposition temperatures, which might indicate the start of precursor decomposition at this deposition temperature.

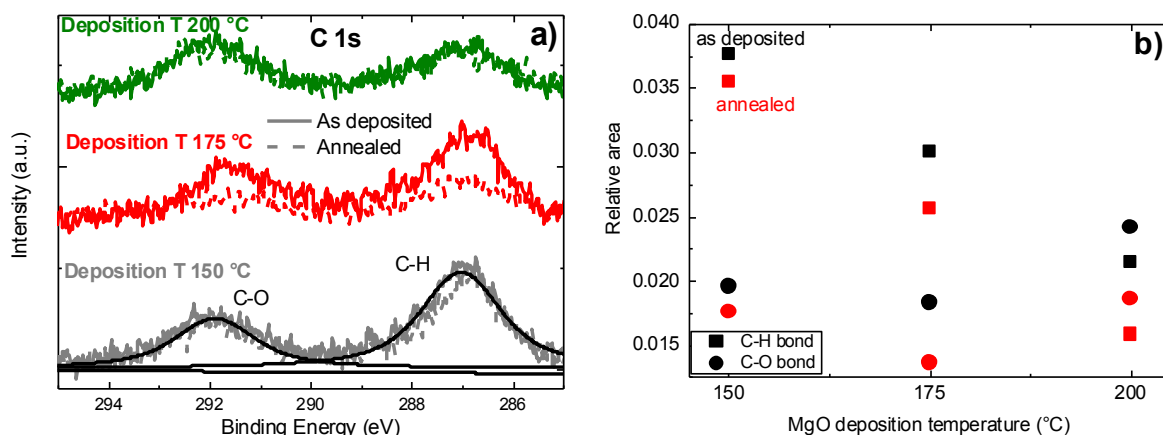


Figure 5.9: a) Raw data and example fits of the C 1s core level signal after linear background subtraction. Signals are offset for better visibility. b) Relative area of the components of the C 1s core level signal, relative to the total area contributed by all main core level signals (Mg 2p, O 1s, C 1s, Si 2p) for as-deposited samples and after 5 minutes the annealing step at 200 °C at varied deposition temperature.

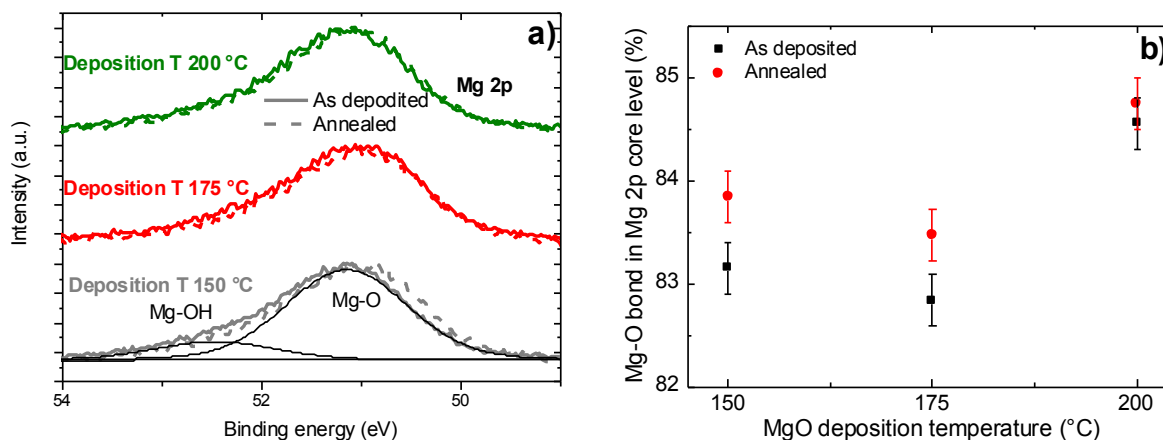


Figure 5.10: a) Raw data and example fit of the Mg 2p core level signal after subtraction of the linear background. Signals are offset for better visibility. b) Relative area of the Mg-O bond to the total area of the Mg 2p core level signal for as-deposited samples at varied deposition temperatures, and after annealing at 200 °C.

The next XPS signal of interest is the Mg 2p core level. In this core level, there are two clearly detectable components: Mg-(OH) and Mg-O bonds (fig. 5.10 a) [222]. No formation of $\text{Mg}(\text{CO})_3$ [223] was detectable in the Mg 2p core level signal. Therefore, it can be assumed that these observed carbon bonds originate from the $\text{Mg}(\text{CpEt})_2$ precursor residuals. Fig. 5.10 b

shows that for all deposition temperatures, the ratio of Mg-O to Mg-(OH) bonds increases after the annealing step. Therefore, it can be concluded that with annealing, the Mg-(OH) bonds are indeed substituted by Mg-O bonds, as surmised from the passivation/carrier lifetime data discussed in previous sections.

Finally, the O 1s core level was investigated. In this signal, at least 5 components, i.e. individual peaks, are present which are hard to distinguish from each other, and thus it is difficult to assign specific chemical bonds. The components that could be located in this binding energy range are: Mg-O, O-Si, -Mg(OH), -CO, H₂O[223], [234]. Because of this complicated peak structure and the limited energy resolution, no fitting of individual peaks to this signal will be presented, corresponding peak positions for mentioned signals as reported in the literature are shown in fig. 5.11 a.

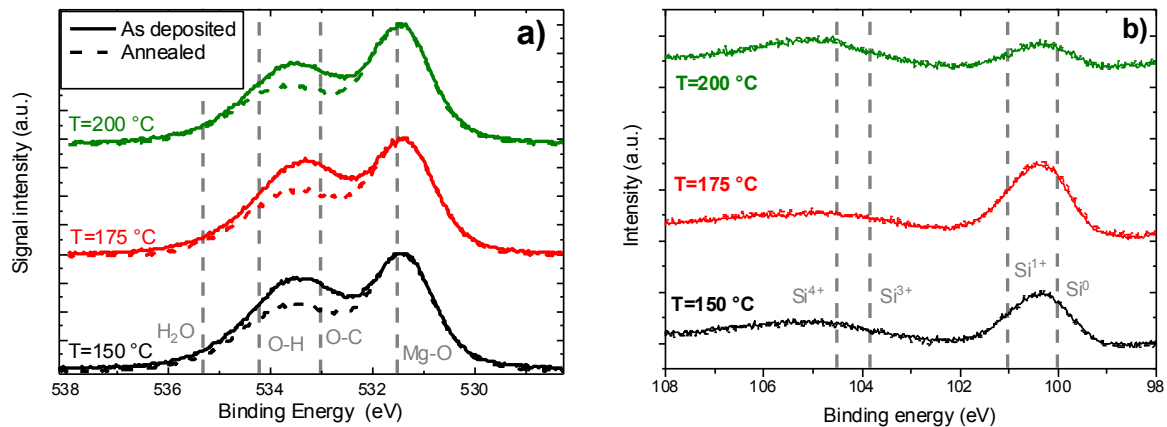


Figure 5.11: a) Normalized intensity of the O 1s core level. b) Raw data of the Si 2p core level signal for as-deposited samples at varied deposition temperatures, and after annealing at 200 °C. Signals are offset for better visibility. For both figures linear backgrounds were subtracted. Possible positions for core level signals are shown in grey.

Fig. 5.11 a shows that for all samples after annealing, the signal intensity at higher binding energies decreases. Within this sample series, the Si 2p core level was analyzed, and the presence of oxidation states of silicon has been observed, which indicates the presence of silicon sub-oxides, SiO_x at the interface.

Analysis and fit of this signal was limited, due to high level of uncertainty for this signal, especially for Si¹⁺ oxidation state, due to possible satellite of Mg K_b signal from Mg 2s core level, which would be located at around 90 eV. Peak positions for signals in Si 2p core level are shown in fig 5.11 b. However, no observable changes in relative area ratio and peak shape

were seen in this core level upon annealing. Therefore, it can be assumed that the O-Si contribution should also be unchanged for the O 1s core level, as such signal would represent Si-O bonds. Keeping this in mind, it can be surmised that the annealing step mainly affects -CO and -OH groups within the MgO film, and that layers become more stoichiometric with the annealing step [235]. Thus, the annealing temperature of 200-250 °C is sufficient to break the -OH bonds. Therefore, it is possible that hydrogen diffuses from the MgO layer to the interface, hence the MgO layers become less defective due to less hydrogen at the surface and in the bulk [236]. Thus, surface passivation would be improved.

5.4.3 SHJ solar cells with MgO layers at varied deposition temperatures

In order to see the influence of the deposition temperature of MgO layers on the final device performance, SHJ solar cells with an MgO layer at the rear side after 25 deposition cycles were produced. Similar to the previous section, devices with and without the addition of an i-aSi:H buffer layer at the rear side are considered. No differences in growth per cycle in the varied temperature range were observed, and all deposited MgO layers had thicknesses of 2.7 ± 0.1 nm.

First, devices without i-aSi:H layers are investigated. Fig. 5.12 shows the main characteristics of such cells. The efficiency of these cells is very modest, and lower than in the optimal case for such a device that was shown in chapter 5.3.3, due to the MgO layer being thicker than optimal thickness. Therefore, the fill factor of these cells is lower. However, even in such suboptimal case, it is possible to estimate the device parameter dependence on deposition temperature of the MgO layers. It can be seen that with the increasing deposition temperature, there is a slight increase in J_{SC} and V_{OC} , with the maximum cell efficiency at a deposition temperature of 175 °C, due to the highest FF. The efficiency of this sample was 13.03 ± 0.3 %. With further increase of the deposition temperature, there is a drop in efficiency, due to the slight drop in V_{OC} , and substantial decrease in fill factor. One of the possible reasons for these losses is due to the MgO layer being the most stoichiometric, as shown in the XPS analysis in the previous section. Therefore, the layer is possibly less conductive, which would cause a drop in the fill factor.

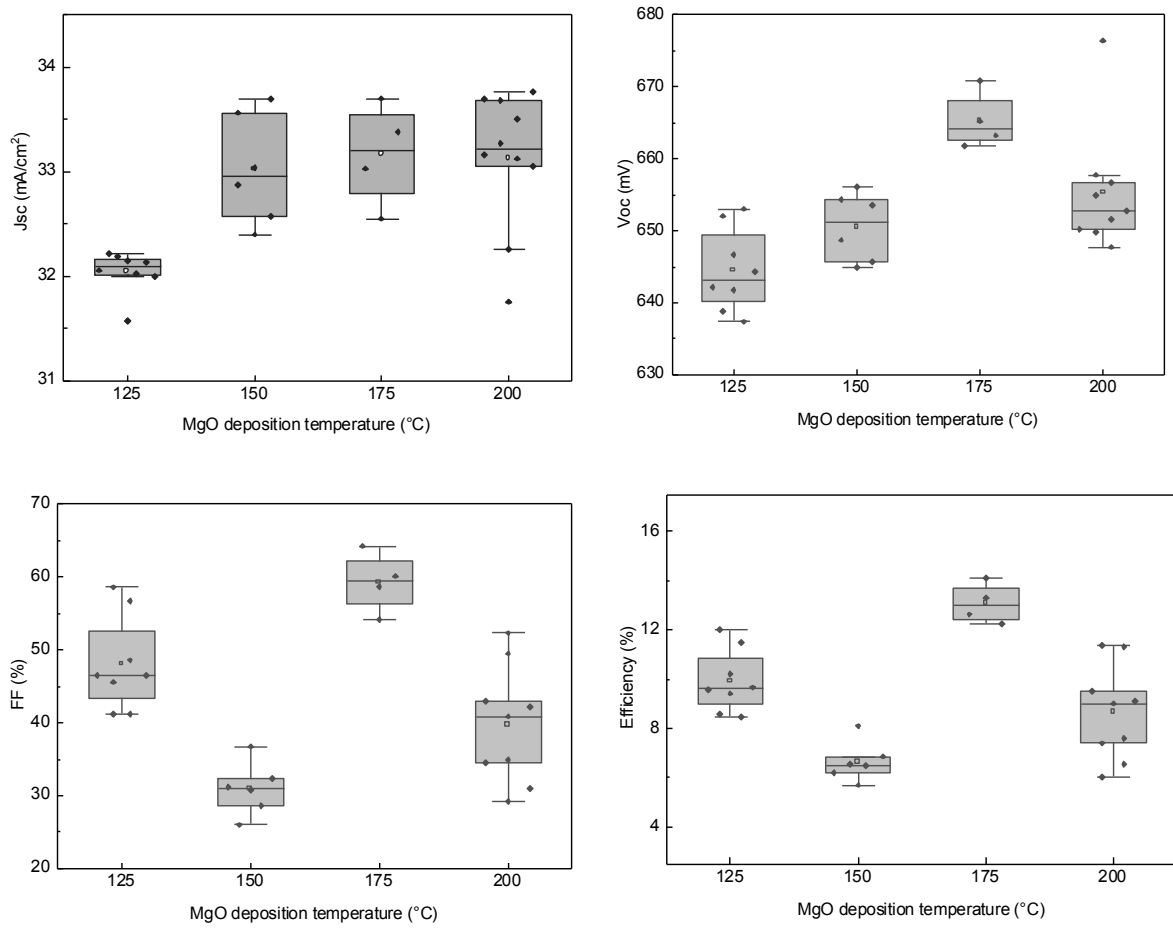


Figure 5.12: Solar cell parameters for solar cells with the rear structure c-Si/MgO/Al at varied deposition temperatures for the MgO layers.

The following step is to investigate solar cell devices with the inclusion of an i-aSi:H layer at the interface between the c-Si wafer and MgO layer. The structure of the solar cell is the same, as previously discussed, with inclusion of the i-aSi:H passivation layer (≈ 5.5 nm). Additionally, for cells with i-aSi:H layers, in order to mitigate efficiency losses due to the metallization, two types of metal stacks at the rear side of the solar cell are considered: aluminum and a stack of titanium (10 nm) and silver (500 nm) (Ti-Ag). The parameters of these solar cells are shown in fig. 5.13. It can be seen that at low deposition temperatures (125, 150 °C), solar cell parameters for both types of metallization are similar. The maximum solar cell efficiency can be achieved at MgO deposition temperature of 150 °C.

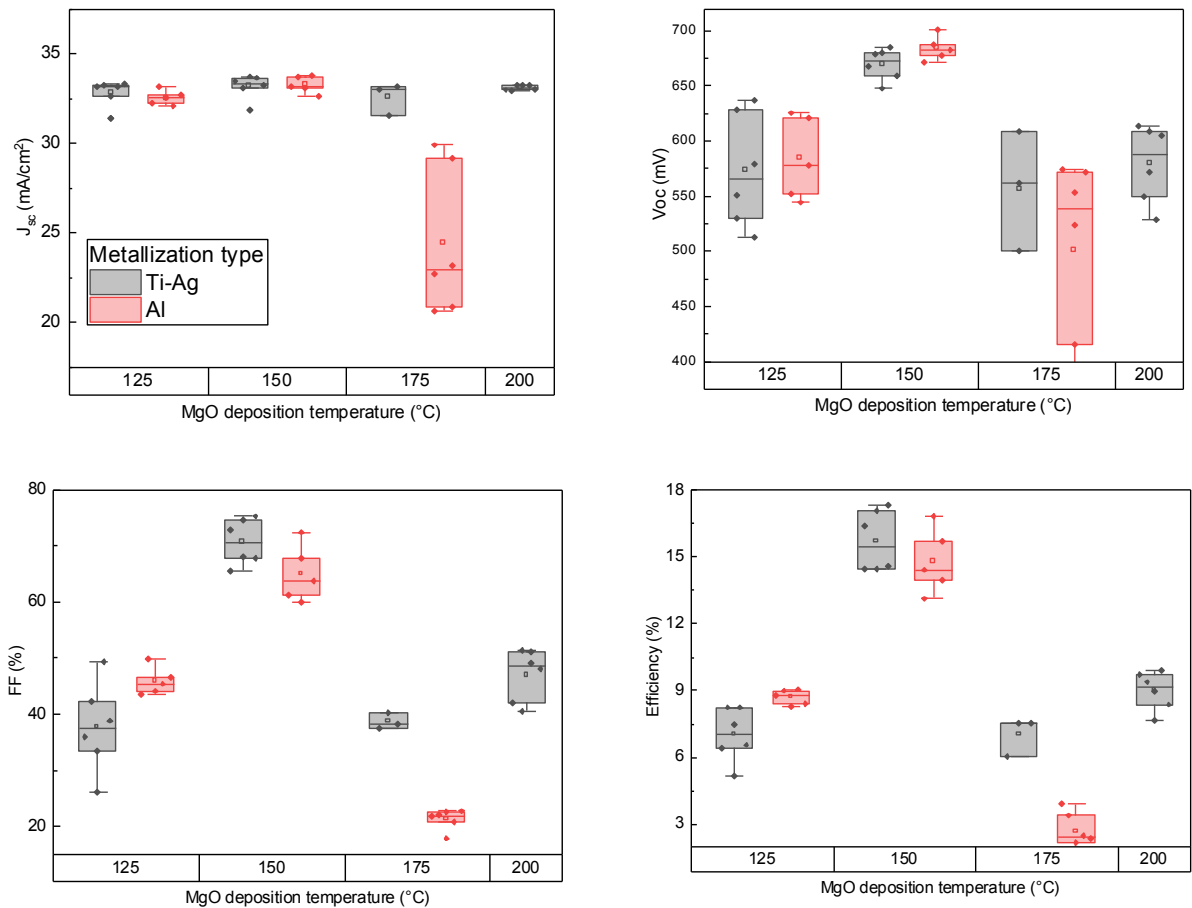


Figure 5.13: Solar cell parameters for solar cells with the rear structure c-Si/i-aSi:H/MgO/Al(Ti-Ag) at varied deposition temperature for the MgO layers. Both Al (red) and Ti-Ag (black) metallization schemes are considered.

However, for solar cells with MgO layers deposited at 175 °C, there is a drastic degradation in performance, which is especially pronounced for the sample with Al metallization. Unlike the samples without the i-aSi:H buffer layer, this temperature is already damaging for the stack. The drop in V_{oc} corresponds to the passivation behaviour for such deposition temperature, where there is an increase in the interface defect density, as was discussed in previous sections. For the deposition temperature of 200 °C only the Ti-Ag metallization was considered. It is possible to see a slight improvement in efficiency. However, both V_{oc} and FF are significantly lower, in comparison to samples deposited at 150 °C.

Therefore, despite having the ALD window at the investigated temperature range (125-200 °C) for the MgO layer deposition, interface and device properties drastically differ. In the case of

the direct deposition of MgO layers on top of c-Si wafers, the optimal temperature is at around 175 °C. However, the inclusion of i-aSi:H as a passivation layer, shifts the optimal temperature to a lower range. In both cases, it was shown how a slight change in deposition temperature of the MgO layer can influence the performance for the solar cell devices.

5.5 Magnesium oxide-metal contacts for silicon heterojunction solar cells

5.5.1 Comparison between Al and Ti-Ag metallization

As was discussed in the previous sections, solar cells with aluminum contact exhibit high thermal instability at already moderate annealing temperatures. In order to mitigate these losses, other metals should be considered for this contact. Therefore, for SHJ devices with MgO layers, two alternative metallization stacks at the rear side, deposited on top of the MgO layer were examined: aluminum and a titanium-silver stack. To compare these contacting schemes, SHJ solar cells with varying i-aSi:H layer thicknesses and with a constant MgO layer thickness after 25 ALD cycles (≈ 2.7 nm) were produced. Thus, it is possible to monitor not only the dependence of the cell performance on the metallization type, but to also find the optimal i-aSi:H thickness for these structures.

<i>Type of metallization</i>	<i>Jsc (mA/cm²)</i>	<i>Voc (V)</i>	<i>FF (%)</i>	<i>η (%)</i>	<i>Rs (Ω*cm²)</i>
<i>Aluminum</i>	33.5	0.691	69.6	16.1	3.1
<i>Titanium-Silver</i>	33.7	0.684	75.2	17.3	2.2

Table 5.2. Solar cell parameters for the best devices fabricated on planar Si wafers incorporating ALD-grown MgO layers with an i-aSi:H thickness of 5.48 nm and different rear side metallization.

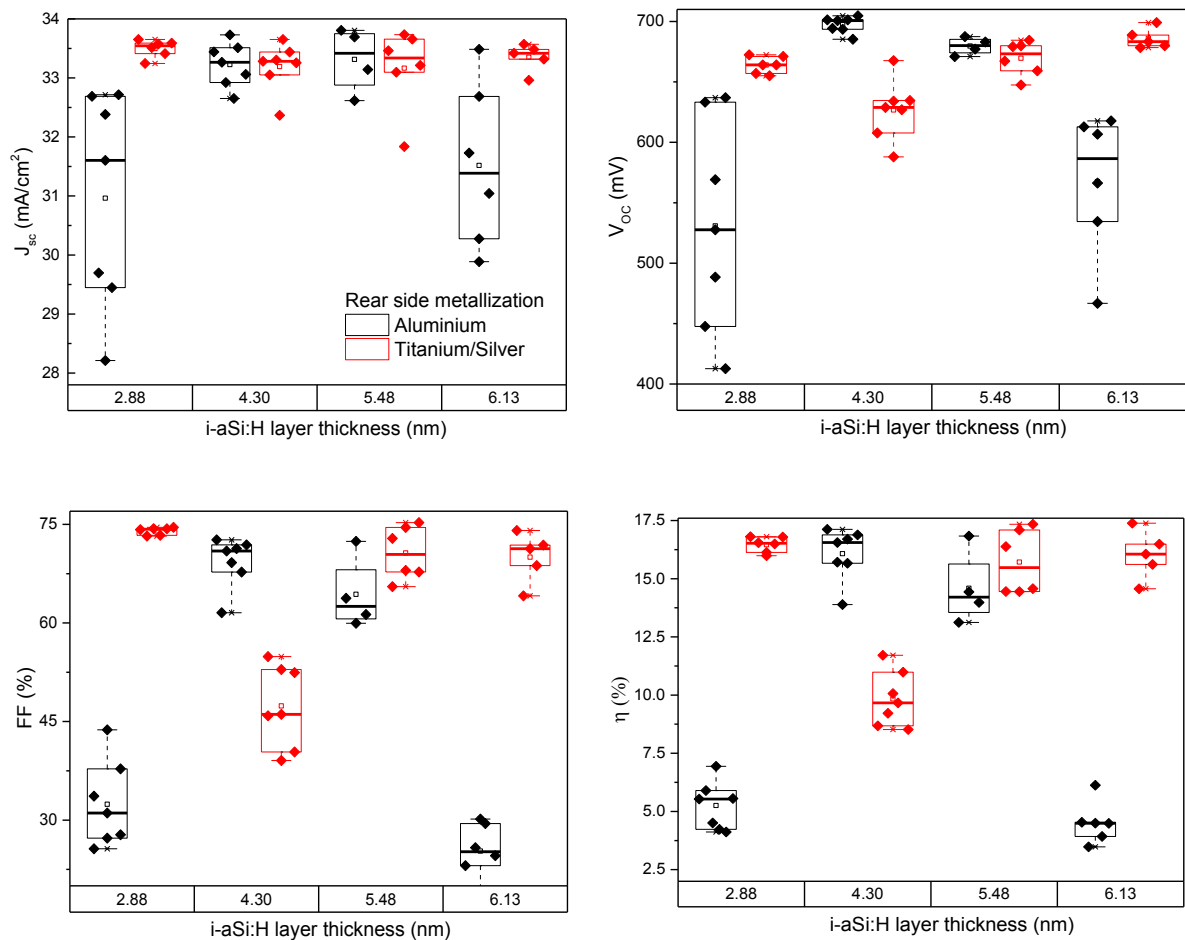


Figure 5.14: Solar cell parameters for solar cell devices with different rear side metallization and varied i-aSi:H layer thicknesses.

Fig. 5.14 shows solar cell parameters for the variations. Each wafer had 3-7 solar cells, with a cell size of 1 cm². In general, there is a high scatter in the performance for each wafer. This deviation could have been due to technological problems during the fabrication step, such as a parasitic deposition of the MgO material on the other side of the wafer during the ALD process, as was mentioned in the previous sections. Another problem in the production of these cells could be due to the MgO layer itself. As was shown in previous sections, a thin layer of 2-3 nm is needed for a high V_{oc} and fill factor of the solar cell. However, at the same time, such thickness after 25 cycles is possibly too thin to be able to improve the passivation and to provide high enough charge for the electron transport, as it was shown in chapter 5.3.1. Therefore, it is possible that for such thickness, either the layer is not fully closed, which causes the increased defect density at the interface, or the charge density is too low to provide carrier selectivity at

the interface. These issues could explain the outlier samples for Ti-Ag metallization at an i-aSi:H thickness of 4.3 nm, as well as those with Al metallization and i-aSi:H thickness of 6.2 nm. The low performance of the cells with Al metallization and a thin i-aSi:H layer of 2.85 nm can again be explained by the diffusion of Al, which degrades the interface. However, for the Ti-Ag metallization, it is possible for solar cells with such i-aSi:H thickness to have efficiencies of 16.5 ± 0.4 %, and to maintain sufficient passivation. Additionally, by comparing the averaged results over the wafer (fig. 5.8) and best cells (table 5.2) performances for both types of metallization, it is possible to see that for Ti-Ag metallization, the V_{OC} output is lower than for Al metallization. The reason for these findings is not fully clear. However, the fill factor is drastically higher, due to the reduced series resistance. For the best devices, the relative difference of FF between the solar cell devices with Ti-Ag and Al metallization is above 8 %, which indicates that that MgO/Ti-Ag metallization scheme is, indeed, preferable for improved device output in comparison to MgO/Al.

5.5.2 Annealing of solar cells with different metallization

The next issue to be addressed for the different metallizations is the thermal stability of the solar cells with MgO layers. Devices with different rear stacks were annealed for 5 minutes in air at varied annealing temperatures and measured at PL setup. Samples were measured at the same conditions, with the same analysis area chosen for the analysis. Fig. 5.15 a-c show the histograms of the PL intensities for solar cell for each stack in the as-deposited state and after annealing. An example PL image is shown fig 5.d with the selected investigated area.

In fig. 5.15 a and b, the samples measured to generate the histogram, have the same metallization and layer structure, except for the presence of the i-aSi:H layer between the wafer and MgO layer. The PL measurements were performed in an uncalibrated mode, and therefore, the PL histogram gives only an indication in the relative change of recombination at the silicon surface. Under the same illumination and exposure conditions, for the stack without i-aSi:H layer, there is only a slight decrease in the intensity distribution for the cell, thus the c-Si interface passivation by the layer stack remains at a similar level for all annealing temperatures.

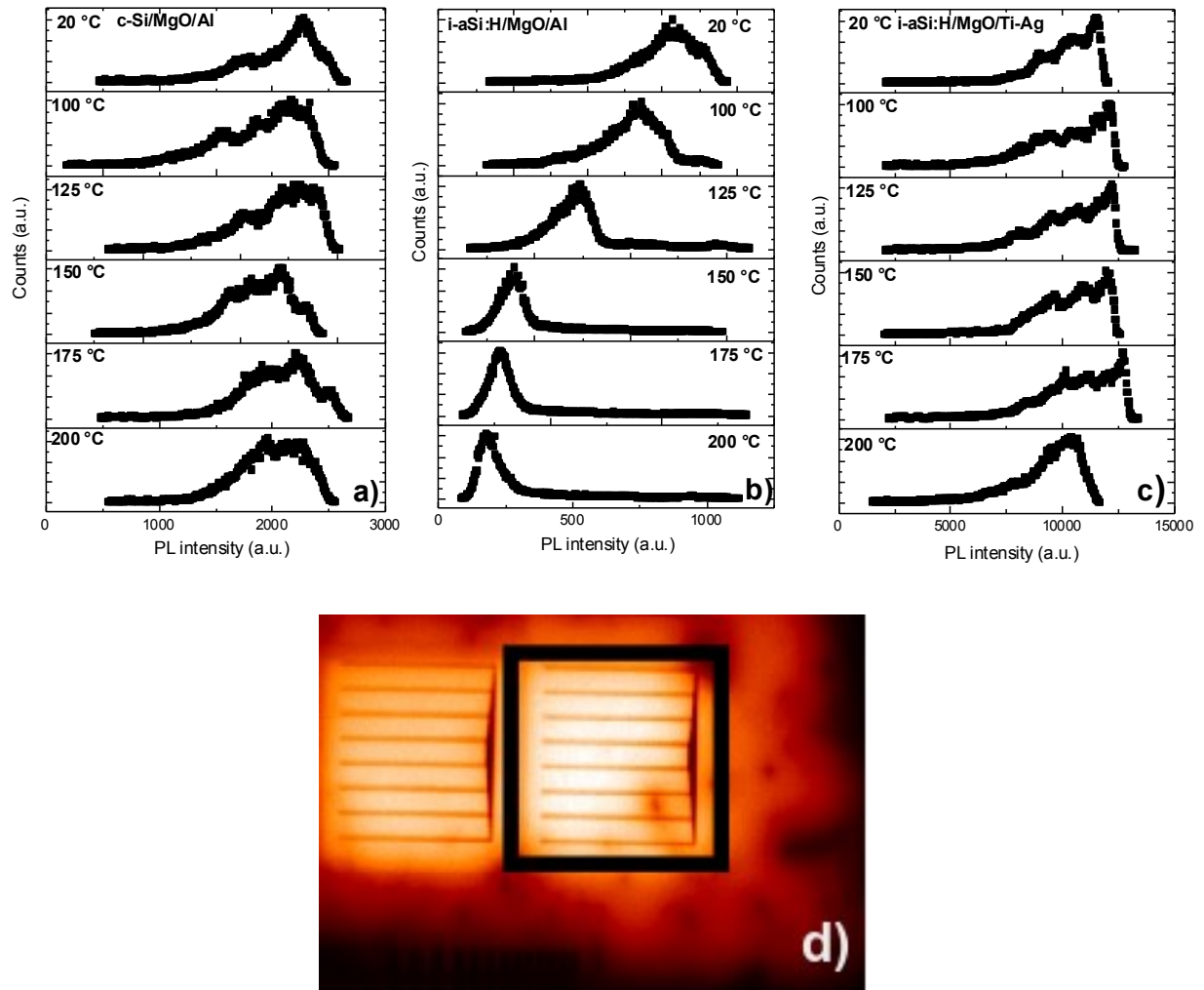


Figure 5.15: PL intensity histogram for solar cells after annealing at the temperatures given in the inset with rear side structure: a) Al/MgO/c-Si, b) Al/MgO/i-aSi:H/c-Si, and c) Ti-Ag/MgO/i-aSi:H/c-Si. D) PL image of the sample, the selected area corresponds to the area of one solar cell.

At the same time, for the stack with included i-aSi:H and Al metallization, signal intensity already starts to decrease at a low annealing temperature of 100 °C, and at 150 °C almost no signal is detectable. This is consistent with the assumption that, indeed, aluminium diffuses to i-aSi:H through the MgO layer. Thus, passivation degrades, probably due to the formation of intermediate Al silicide layer. This coincides with a significant reduction of V_{OC} in the final devices [237], [238]. On the other hand, the same structure but with Ti-Ag metallization shows almost no degradation of PL intensity up to an annealing temperature of 200 °C.

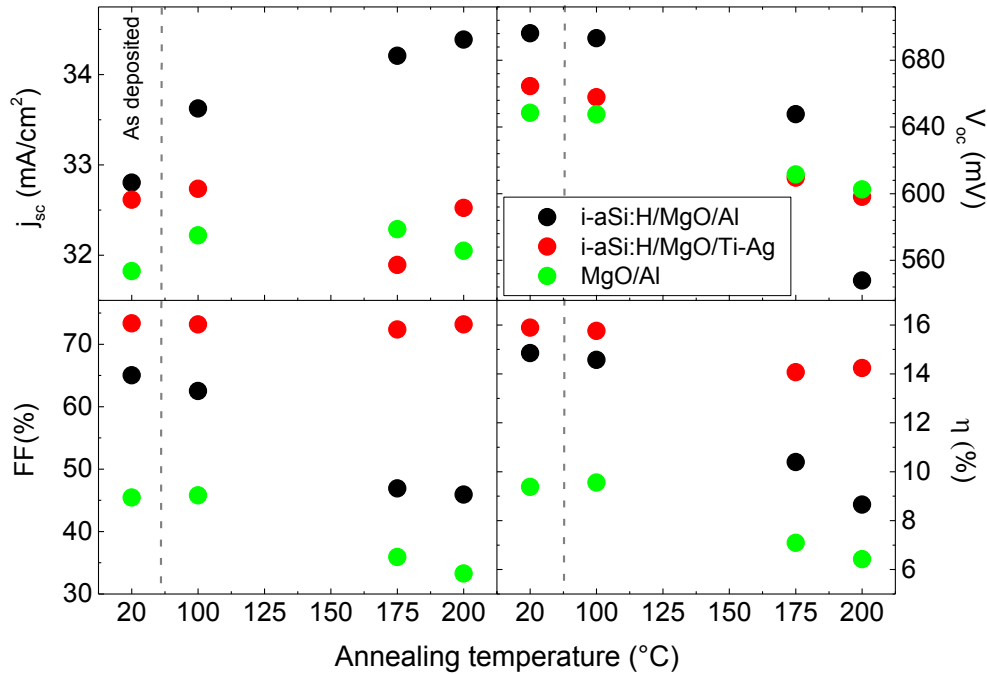


Figure 5.16: Parameters for solar cells with different rear side contact stacks using MgO layers with varying annealing temperatures.

Moving on to the comparison of this data to the solar cell performance with annealing temperature, fig. 5.16 shows solar cell parameters with the previously discussed structures at varied annealing temperatures. Despite the changes in PL intensity with annealing temperatures for the Ti-Ag metallization being less pronounced than for Al metallization, there is a noticeable degradation of the V_{oc} for cells at high annealing temperatures. On the other hand, it can be seen that the fill factor for cells with Ti-Ag metallization stays at a similar level after annealing. Therefore, decrease of the cell efficiency of around 2 % is caused by the drop in V_{oc} . At the same time, the sample with Al metallization has not only passivation losses, but also a severe degradation of the fill factor, which corresponds to the drastic increase in the series resistance of stack with annealing, from $4.5 \Omega\text{cm}^2$ for the as deposited sample, to $9.5 \Omega\text{cm}^2$ after annealing at $200 \text{ }^\circ\text{C}$, as calculated from the JV curve, while the structure with Ti-Ag metallization shows no such degradation.

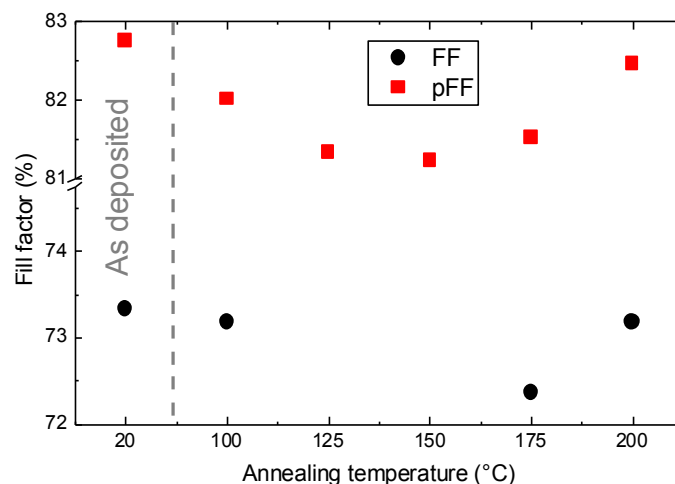


Figure 5.17: FF and pFF for solar cells with MgO/i-aSi:H/c-Si layer stack at the rear side with Ti-Ag metallization.

Only for the structure with Ti-Ag metallization it was possible to extract the pFF data from the Suns-Voc, measurements, as it is shown in fig. 5.17. Other structures exhibited s-shaped illuminated J-V curves, and the calculated pFF values were higher than expected ($> 89\%$), which indicates further recombination losses and formation of barriers for these structures. Therefore, it can be concluded that Ti-Ag metallization is preferable for solar cells with MgO layers, with benefits for cell in the efficiency and thermal stability.

5.6 Chapter summary

In this chapter an investigation of low temperature ALD magnesium oxide layers on c-Si(n) and i-aSi:H/c-Si(n) substrates, at deposition temperatures of 125-200 °C, was presented. The interface passivation and layer properties, as well as the behavior of such layers upon an additional annealing step have been discussed. It was observed that MgO layers do not provide good passivation on their own on c-Si wafers. A weak passivation effect yielding minority carrier lifetimes of 0.15 ms was observed for a ~9.8 nm thick MgO layer directly deposited on c-Si after an annealing step of 200-250 °C. However, such a thickness is too high to be device-relevant, due to the insulating properties of MgO layer insulator. Therefore, an intermediate layer is needed to provide good passivation. In this thesis, i-aSi:H layers were used as additional passivation layers. In this case, the MgO layer functioned as a part of the passivation layer stack,

and its primary function was that of an electron-selective contact. Additionally, it was observed that for both types of layer stacks the contact showed an Ohmic behavior. Therefore, both types of stacks could be used in SHJ devices. However, with increasing MgO layer thickness, the contact resistance increases drastically. For device-relevant MgO thicknesses of around 3 nm (30 ALD cycles), the contact resistance in the MgO/c-Si layer stack was approximately $0.18 \Omega\text{cm}^2$, and for the MgO/i-aSi:H/c-Si stack it was $0.95 \Omega\text{cm}^2$. Thus, for both contact stacks, there is a tradeoff between the passivation quality and contact resistance.

In order to investigate possibilities for the further development of such layers stacks and ALD MgO layers for solar cells, in particular, SHJ solar cells with different parameter variations were produced.

The first important step was to have working devices with varied ALD MgO layer thicknesses in order to see, what solar cell parameters can be achieved, and potential of ALD MgO layers in SHJ solar cells. The SHJ solar cells with two types of stacks (c-Si/MgO and c-Si/i-aSi:H/MgO) at the rear side as passivating-electron selective contacts and standard (p,i)a-Si:H hole selective contacts at the front side were fabricated on flat wafers. The cells for both types of stacks showed similar efficiencies of above 16.4 %. Therefore, both stacks showed potential for further investigation. At the same time, the stack with the additional i-aSi:H layer showed higher V_{OC} output. However, a slight decrease of the fill factor was observed, in comparison to the MgO/c-Si layer stack. Coincident, a problem with the metallization was identified for this stack. For these cells, aluminum metallization at the rear side was used. Upon annealing of the cells at the moderate temperature of $150 \text{ }^\circ\text{C}$, the total cell parameters degraded severely.

Therefore, the next important topic to consider were layer properties and cell outputs for varied deposition temperatures of MgO layers. The ALD window for these layers is in the range of $125\text{-}200 \text{ }^\circ\text{C}$. It was shown in this thesis, that the deposition temperature is a crucial parameter for the solar cell performance. For cells with i-aSi:H layer, the highest output was achieved at a deposition temperature of $150 \text{ }^\circ\text{C}$. However, for the direct c-Si/MgO stack the optimal temperature was higher, at $175 \text{ }^\circ\text{C}$.

Finally, the analysis of the rear side metallization was done. In this work, a Ti-Ag metallization scheme was compared to Al, for as deposited and annealed cells. In general, in both cases as-deposited devices showed similar solar cell efficiencies. However, solar cells with Ti-Ag contact demonstrated lower V_{OC} , but with a drastically higher fill factor than the Al contact.

Additionally, upon annealing, solar cells with Ti-Ag metallization showed a degradation in passivation, but the fill factor remained at a similar level. At the same time, solar cells with Al contact exhibited a drastic degradation in fill factor and especially V_{OC} already at moderate annealing temperatures (150 °C). Therefore, it can be concluded that Ti-Ag metallization for solar cells with MgO layers is beneficial for the solar cells, and more thermally stable in comparison to Al contacts.

Therefore, the ALD MgO layers presented in this thesis, can be considered as a suitable building block for further development in c-Si based devices. Furthermore, the low process temperatures (< 200 °C) ensure compatibility with the well-established i-aSi:H/c-Si heterojunction technology used in high efficiency cells. A solar cell efficiency of 17.3 % for SHJ cells implementing MgO layers on the rear side of flat wafers was achieved. Possible further routes for improvements include further optimization of the metal contact and the interface with the i-aSi:H layers. Also, the deposition of MgO on top of an intentionally grown ultrathin silicon oxide rather than an HF-last Si surface can be considered as a route to achieve improved contact properties and passivation.

Chapter 6

Prospects and challenges for carrier-selective contacts for solar cells

6.1 Introduction

So far, this thesis only presented results for metal oxide layers used as electron-selective contacts in SHJ and perovskite solar cells. However, this is only a part of the larger field of research dedicated to different carrier-selective contact schemes for c-Si based solar cells. It is, therefore, worthwhile to look further into other possible applications and prospects for other metal oxide layers as carrier-selective contacts, silicon-based cells, as well as into the applicability of ALD for research and further industrialization.

Therefore, this chapter addresses several points that are relevant for further development in this field.

The first section of this chapter focuses on carrier-selective contacts that can replace aSi-based layers in silicon-based devices, without sacrificing the thermal stability and efficiency of the solar cell. The first part discusses solar cells using SiO₂/poly-silicon contacts as an alternative for further development of Si-based solar cells. Moreover, these cells are already used in industry and exhibit much higher efficiencies in comparison to those using metal oxide contacts. The second part presents a brief overview of metal oxides used as electron-selective layers, and discusses perspectives on this approach. The last part comments on the perspectives and issues of implementing TMO layers with high work functions as hole-selective materials for c-Si based solar cells.

The second section of this chapter focuses on atomic layer deposition (ALD) as a prominent deposition method for carrier-selective layers for both silicon-based and perovskite solar cells. For these layers, thickness control is crucial for final device performance. With ALD, it is possible to have monolayer scale control over layer thickness. Furthermore, ALD requires low deposition temperatures and can provide high quality uniform and conformal layers, which is crucial for solar cell interfaces and further scalability of the devices. Thus, it is important to

understand, what benefits and possible complications can be encountered during further development of ALD layers.

6.2 Carrier-selective contacts for SHJ solar cells

6.2.1 Silicon-based carrier-selective contacts

SHJ solar cells based on amorphous silicon layers exhibit high efficiencies: for both-side contacted SHJ 25.1 % [9], and for integrated back contact (IBC) exceeding already 26.6 % [239]. However, the main drawback of these layers is thermal instability at temperatures above 200 °C. This issue limits further fabrication processes of the solar cells. The main topic of this thesis addresses the substitution of aSi-based layers with dopant-free layers, such as metal oxides. However, another prominent approach is to use poly-silicon contacts. Solar cells implementing poly-silicon (poly-Si) contacts (known as TOPCon (tunnel-oxide passivating contacts), or POLO (poly-Si on oxide)) have recently achieved quite remarkable efficiencies above 25 % for both-sides contacted [240], and above 26 % for integrated back contact c-Si solar cells [241]. Thus, this approach is attractive for further development and is already being researched at the industrial level, achieving efficiencies above 24.5 % for large scale wafers [242].

The main idea behind this concept is the deposition of a poly-Si layer on top of a thin SiO₂ layer. This deposition requires high-temperature processing (~ 900 °C) and layers are subsequently stable at elevated temperatures. The doping can be introduced during the deposition of the poly-Si layers, or afterwards by ion implantation [243], or diffusion [244]. The SiO₂ layer provides chemical passivation at the c-Si/SiO₂ interface, ensuring a low defect density at the interface. Additionally, it functions as a barrier to dopant diffusion from poly-Si layers. Thus, the quality, thickness and stoichiometry of the SiO₂ are crucial for final device performance. The implemented thickness of SiO₂ layers in devices varies from 1.4 nm [240] up to 3.6 nm [244]. There are still uncertainties regarding the main charge carrier transport mechanism for poly-Si cells. It is commonly assumed that, for SiO₂ thicknesses below 2 nm, tunneling is the main transport mechanism. However, for thicker layers the probability of tunneling is highly reduced, thus, another proposed transport process is through pinholes in SiO₂ layers [245], [246].

The poly-Si approach is attractive for further developments, but it has some drawbacks. The main issue is that poly-Si has a bandgap similar to c-Si. Thus, a doped poly-Si layer on the front side of the device would result in high absorption losses. Additionally, heavy doping of poly-Si results in free-carrier absorption [247]. Thus, poly-Si layers are most suitable for the rear side of the solar cell.

6.2.2 Metal oxide layers as electron-selective contacts

The main topic of this thesis is the investigation of metal oxide layers as electron-selective contacts. It is thus important to have an idea of the larger context. A rapidly increasing interest in various metal-oxide layers for electron-selective contacts has been observed in recent years. The most promising results, so far, have been achieved with TiO_x layers. These layers do not passivate c-Si surfaces and so a buffer SiO_x tunnel layer is used to ensure passivation. By improving cell processing and the TiO_x contact structure, an improvement from efficiencies of 19.8 % [225] to 22.1 % [10] was achieved in a short span of time. Another important parameter is the choice of deposition method. The electron selectivity of TiO_x layers is strongly affected by film growth. It has been shown that TiO_x layers grown by plasma and thermal ALD resulted in reversed band bending, which creates the additional transport barrier and thus hinders band alignment [248]. Furthermore, the choice of metal contact is also important, in order to ensure minimal contact losses through a suitable band alignment. Thus, metal contacts with low work functions, such as Al, Mg, or Ca should be used.

<i>Metal oxide</i>	<i>Deposition method</i>	<i>Buffer layer</i>	<i>V_{oc}</i> <i>(mV)</i>	<i>FF</i> <i>(%)</i>	<i>Efficiency</i> <i>(%)</i>
<i>TiO₂</i> [10]	ALD	SiO_x	674.0	82.5	22.1
<i>MgO</i> [60]	Thermal evaporation	-	628.8	80.6	20.0
<i>AZO</i> [249]	Spin-coating	i-aSi:H	672.1	72.0	18.5
<i>SnO₂</i> [250]	Sol-gel	i-aSi:H/ SiO_x	685	71.5	18.4
<i>Ta₂O₅</i> [251]	ALD	-	638	79.3	19.1

Table 6.1: Best c-Si based solar cell devices, using metal oxide layers as electron-selective contacts.

However, TiO_x layers are not the only ones to have been investigated over the last years. More promising materials have been developed and introduced to the solar cell structure, such as Ta_2O_5 [251], MgO and Nb_2O_5 [11]. These materials can provide passivation by themselves, or be deposited atop a buffer layer (such as SiO_2 or $i\text{-aSi:H}$), and provide high electron selectivity. Another option is doped ZnO . There are already works that implement boron-doped ZnO layers as a full-area rear electron selective contact [252], yielding reduced absorption and series resistance. Another possibility is aluminum doped ZnO (AZO). AZO layers are commonly used as TCOs, but it has been shown that these layers can serve also as an electron-selective contacts [249]. However, the FF for such cells is low in comparison to other metal oxide materials, as shown in table 6.1.

The use of metal oxides as an electron-selective contacts is a relatively new topic in comparison to high work function TMOs. Most results regarding c-Si based solar cells with such electron-selective contacts have been published in the last 2-3 years, as of the writing of this thesis. These devices have so far shown promising results (table 6.1). Nevertheless, there is still a way to go for the further development of these layers, and issues that have to be addressed. One of the main concerns is thermal stability. Depending on the deposition method and temperature, the morphology and layer properties drastically differ. For the ALD MgO layers that were investigated in this thesis, the MgO/Al stack in the solar cell exhibited a degradation in passivation and fill factor already at annealing temperatures below $200\text{ }^\circ\text{C}$, whereas a similar stack with an evaporated MgO layer was shown to be stable up to $300\text{ }^\circ\text{C}$ [60]. Additionally, so far all metal oxide layers used as electron-selective contacts in c-Si based solar cells, have been implemented as rear side full area contacts. However, there is an opportunity for these layers to be implemented at the front side, due to their transparency. However, this would require either high lateral conductivities, or a suitable TCO with low work function on top of the metal oxide layer to ensure lateral conductivity and to cap the layers. Currently this has been not yet been investigated.

6.2.3 TMO layers as hole-selective contacts

So far in this thesis, only electron-selective contacts for SHJ solar cells have been discussed. However, regarding hole-selective contact development, it is challenging to have a conductive, transparent p-type material. In classical SHJ solar cells, p-aSi:H layers are used. However, these layers have low thermal stability, low electrical conductivity and high optical absorption [31],

[47]. Another option is employing p-type layers using materials with wider bandgaps, including metal oxides such as NiO_x , Cr_2O_3 or Co_3O_4 [253]. As of the writing of this thesis, only NiO_x layers have been investigated for c-Si based devices. However, these layers can be detrimental to wafer passivation, due to the large number of defects formed at $\text{NiO}_x/\text{c-Si}$ interface [254]. So far, no reports on SHJ devices implementing these layers have been published.

An alternative way is to use TMO materials, such as MoO_x , WO_x , or VO_x . These are n-type materials that exhibit wide bandgaps and work functions higher than the ionization potential of c-Si. Due to their high work function, they can induce a high degree of band bending at the interface with the c-Si wafer. Therefore, hole collection can be enhanced, and the electron concentration reduced at this interface. The schematic band diagram in fig 6.1 shows a comparison between the classical p-aSi:H/c-Si interface and the TMO/c-Si interface. These layers can be deposited directly atop c-Si wafers, as passivating hole-selective contacts. However, in such cases the V_{OC} in solar cell devices is reduced [255]. Consequently, to ensure high quality wafer passivation, an additional i-aSi:H buffer layer [8], or ultrathin tunnel oxide layer (SiO_2) [256], are commonly used.

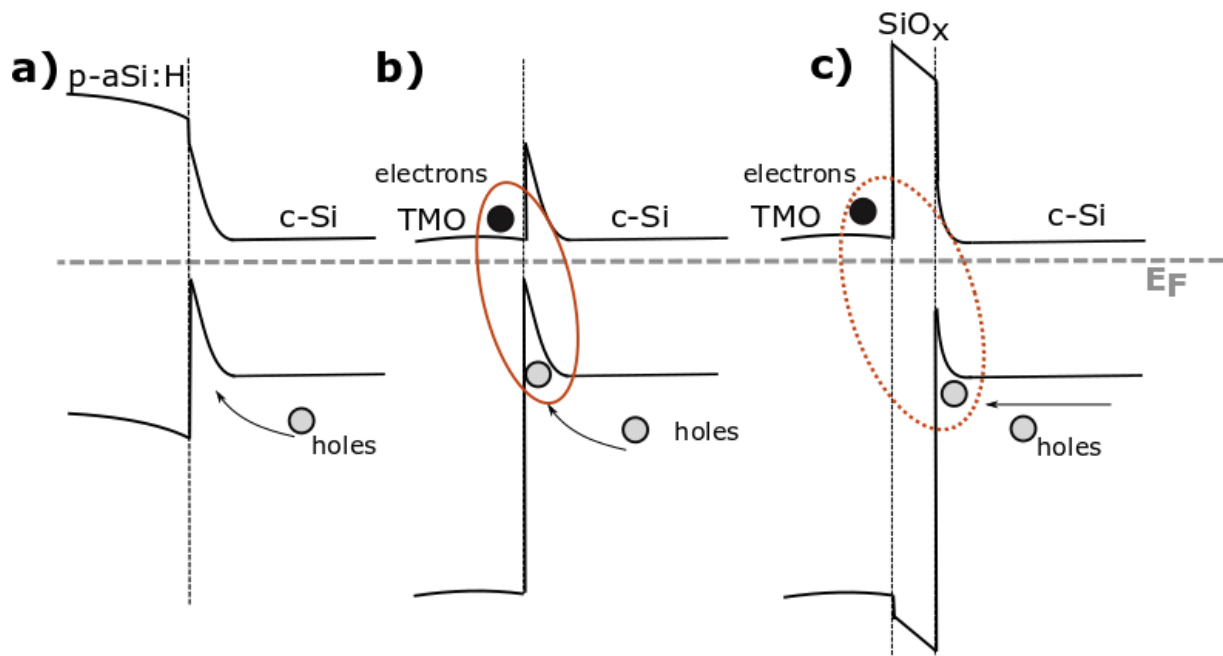


Figure 6.1: Schematic band diagram for a) p-aSi:H/c-Si heterojunction, b) ideal case of TMO/c-Si heterojunction, c) TMO/c-Si heterojunction with formation of intermediate SiO_x at the interface. The tunnel recombination at the TMO/c-Si interface is marked in orange.

These layers have potential for further development. However, there are various issues that should be addressed for their implementation in SHJ solar cells. The first issue is the formation of a thick SiO_x layer at the interface between the silicon-based layer and TMO [132], which creates an additional barrier for the tunnel-recombination contact, as shown in fig 6.1. This SiO_x is especially pronounced for ALD processes, and almost negligible for evaporated layers. However, even for evaporation processes, a mixing layer between the hole-selective contact and the TCO layer can sometimes be induced during TCO sputtering [257]. Therefore, these interface layers may induce additional defects which harm the passivation and create additional potential barriers for the carriers. Thus, this process should be suppressed with surface treatments, or by using a buffer layer.

Currently, the most efficient solar cells with such TMO layers have been those implementing MoO_x as the hole-selective contact, with a cell efficiency of 22.5 % [257]. Moreover, specifically MoO_x layers have been used for the further concept of dopant-free asymmetric hetero-contact cells (DASH solar cells), which are based on the substitution of classical doped amorphous silicon layers with dopant free layers. By now, an efficiency of 20.7 % for a solar cell of this type was achieved [14].

The main problem for TMO layers is the trade-off between band bending and conductivity. In these materials, one of the main types of defects that contribute to layer conductivity are oxygen vacancies. A decreased amount of oxygen vacancies leads to increased band bending and higher hole-selectivity of the layers [131]. However, at the same time, layer conductivities are drastically decreased [95].

Moreover, further research and optimization of these layers is required to achieve higher efficiencies with more temperature stable devices. The thermal instability issue is most pronounced for MoO_x layers, for which post-deposition temperatures above 130 °C should be avoided [257]. It has been shown that with annealing temperatures above 150 °C, there is a degradation in cell performance for cells with MoO_x layers. One of the reasons for this behaviour, is layer reduction to a substoichiometric state with annealing. Already by depositing a MoO_x layer on top of i-aSi:H, a slightly substoichiometric layer is formed [258]. Upon annealing, the oxidation state of MoO_x is reduced even further. As a consequence, layer conductivity increases due to the formation of oxygen vacancies and a reduction in stoichiometry [259]. At the same time, the work function decreases, which leads to a decline in band bending that results in reduced contact-selectivity. This reduction in selectivity results in

a reduced solar cell efficiency and an increasingly pronounced S-shape in the illuminated IV curve. It was shown that the S-shape can be partially mitigated by annealing pretreatments of the i-aSi:H layers, which reduces hydrogen content, which would also reduce the hole-selectivity of MoO_x layers [260], due to the formation of hydrogen donor levels. Thus, thermal stability and the formation of substoichiometric MoO_x layers are important issues that have to be considered for further developments. However, for WO_x layers, a substoichiometric phase forms during annealing steps above 400 °C [261]. Therefore, these layers are more thermally stable.

Other recently investigated TMO materials are VO_x and WO_x. VO_x is not a widely investigated material, due to its relatively low bandgap of around 2.5 eV, which leads to increased absorption in comparison to other considered TMO materials. However, there have been attempts to use these layers in SHJ solar cells, which reached efficiencies above 17 % [262]. On the other hand, WO_x can be considered as a good alternative to MoO_x layers. Out of these three materials, WO_x has the highest bandgap and is more thermally stable than MO_x. This material has not been investigated as a hole-selective contact as much as MoO_x, but its implementation in solar cells has shown similar efficiencies in comparison to MO_x [250]. At the same time WO_x conductivities are much lower in comparison to MoO_x, thus further investigations are needed to increase the conductivity of these layers while maintaining their work function [95].

6.3 Prospects for ALD for carrier-selective contacts

6.3.1 ALD for c-Si based solar cells

The main focus of this thesis has been the development of metal oxide layers as electron-selective contacts. One of the most important points is to have a precise control over the contact layer thickness, due to the trade-off between surface passivation and contact resistance. Therefore, given its monolayer-scale resolution, ALD is an ideal deposition technique. It is already commonly used for metal oxide materials research and in industry, e.g. for Al₂O₃ layers in PERC cells [4]. Moreover, ALD provides high control over processing and doping and involves a simple manufacturing process.

Currently, the most efficient solar cells with metal oxides as electron-selective contacts have been produced using thermal ALD [10]. Additionally, other ALD compatible materials, such

as Ta₂O₅ [251], and MgO (this work) have shown to be promising, and devices implementing these layers have been developed.

At the same time, thermal evaporation is the most common deposition method for high work function TMO layers, such as MoO_x and WO_x, in solar cell devices [131], [257]. Both of these materials have ongoing investigations towards the implementation of ALD layers for solar cells [263], [261]. TMO layers deposited by ALD show promising properties for implementation in solar cell devices, such as increased band bending, or enhanced effective carrier lifetime [263], [264]. However, at this moment there are almost no published results with such layers as hole-selective contacts. The only attempts at implementing ALD MoO_x layers showed a drastically decreased solar cell efficiency, due to reduced carrier selectivity [265], [266], in comparison to cells with evaporated MoO_x layers. Unfortunately, the reason for this issue remains unknown, and thus, further investigations are needed.

One of the most common uses of ALD for c-Si based solar cells is for growing Al₂O₃, due to its excellent passivation of c-Si substrates. These layers are already an industry standard for PERC solar cells [4]. Moreover, ALD Al₂O₃ layers are often used as a hydrogen source for the hydrogenation of the surface, e.g. in POLO solar cells [267]. These layers can also be used as capping layers for annealing treatments of layers, such as for SiO_x and ZnO:B [268]. Besides Al₂O₃, high quality SiO₂ layers are very important for further device developments. The first attempts at SiO₂ growth by ALD involved relatively high deposition temperatures (>300 °C) and no results are yet published that compare ALD SiO₂ layers with other deposition methods. However, there is a rapidly growing list of possible precursors with decreasing required deposition temperatures [269]. Further development in this direction is yet to be explored.

6.3.2 ALD for perovskite solar cells

Poor uniformity and conformality can lead to the formation of pinholes and cracks, thus reducing the carrier-selectivity of the layers and increasing the likelihood of shunts [270]. Thus, ALD has great potential for implementation in perovskite solar cells, as it provides uniform and conformal layers. Perovskite solar cells with layers deposited by ALD commonly show higher PCE and cell stability, compared to those by other deposition methods [52].

Electron-selective contacts are especially crucial for perovskite solar cells. One of the biggest problems for perovskite solar cells is a hysteresis behaviour in the cell output. If the electron-

selective contact leads to an accumulation of charge, there is a drastic increase in hysteresis. However, if the charge can be easily extracted at the interface, the hysteresis can be decreased or even eliminated [205]. Thus further development of electron-selective contacts for perovskite solar cells is crucial. Initially, TiO₂ was the dominant metal oxide material for the investigation, as an electron-selective contact for perovskite solar cells. Perovskite solar cells implementing ALD TiO₂ layers showed drastically higher PCE in comparison to spin-coated layers [271]. However, it was observed that due to the conduction band misalignment between the ALD TiO₂ and perovskite layer leads to PCE limitation and increased hysteresis behaviour. Another possible material for the electron-selective contact is ZnO, due to its high conductivity and optimal conduction band offset to the perovskite. ALD ZnO was successfully employed in the solar cell and showed potential for further implementation [272]. At the same time, considerable work has been dedicated to the implementation of ALD SnO₂ layers as electron-selective contacts for perovskite solar cells. The ALD SnO₂ layers have been shown to yield not only improved cell efficiencies [49], but also enhanced device stability [52]. These improvements could be achieved due to a good band alignment to the perovskite layer due to low conduction band offset, high bulk electron mobility and low deposition temperature for SnO₂. However, these layers require the inclusion of a buffer layer for passivation, tuning of the deposition temperature and annealing post-treatments (e.g. in water vapor). Otherwise, the final devices have a lower PCE, high hysteresis and low stability, as compared to the direct deposition on top of perovskite layer [273].

Hole-selective layers can also be deposited through ALD processes. There are different ways to approach this topic. Similar to SHJ solar cells, TMO layers with high work functions can be employed as hole-selective contacts. The most commonly used TMO material is thermally evaporated MoO_x. However, it has been shown that the MoO_x layers react with the perovskite, which negatively impacts device efficiency and stability [274]. Additionally, there has been a successful implementation of ALD VO_x layers, which have shown to be stable when deposited on top of the perovskite layer [275]. Moreover, for perovskite solar cells, there is a higher degree of freedom when choosing p-type materials, with options such as NiO_x [276] or CuCrO₂ [277], which are not fully suitable for silicon based solar cells due to the detrimental effect of these materials on the wafer passivation [254], [278]. Another possible route is to deposit ultra-thin passivating insulator layers, such as AlO_x, which if deposited between the perovskite and metal contact, would create a metal-insulator-semiconductor hole-transporting contact. Ultra-thin

ALD AlO_x layers have been shown to improve the V_{OC} and PCE of perovskite solar cells [279], [280].

Another possible consideration for ALD is for tandem solar cell applications, as a deposition method for recombination layers and TCOs. There are two most common configurations for tandem solar cells: 4-terminal [281] and 2-terminal [282]. A 4-terminal tandem solar cell consists of two individual solar cells that are deposited separately and afterwards mechanically stacked, but still remain electrically independent

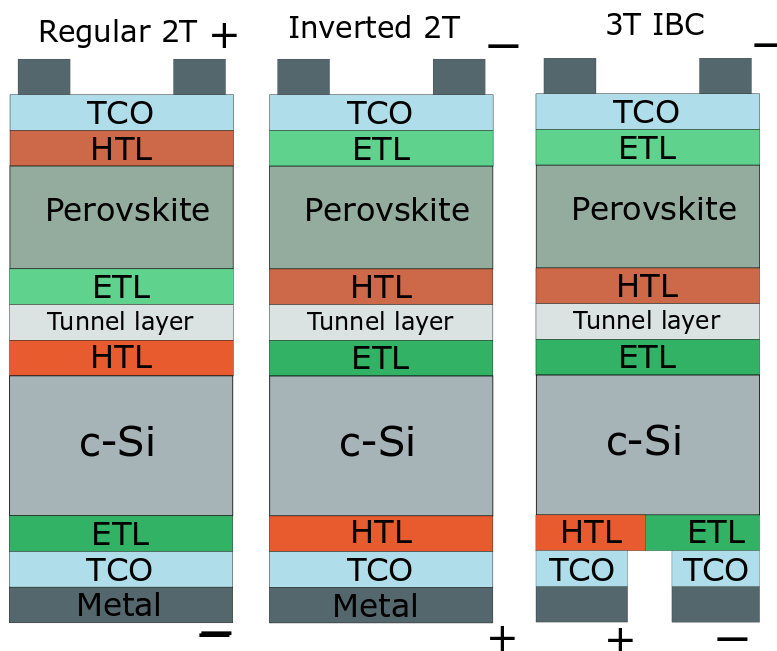


Figure 6.2: schematic representation of possible configuration of 2-terminal and 3-terminal perovskite/c-Si tandem solar cells with inclusion of recombination layer.

For a 2-terminal solar cell, the perovskite solar cell is deposited directly on top of the bottom cell, and both cells are monolithically connected. In this case, the engineering of a tunnel-recombination layer between the cells is required that electrically connects two cells [275]. Another potential tandem architecture is the 3-terminal solar cell, which combines a perovskite solar cell with an IBC solar cell. This concept is not commonly explored, however it is very promising for further development. Such a structure does not require current matching, and can operate as a 4-terminal device, while being compatible with a monolithic design [283]. This is a promising approach, however no experimental results have yet been published.

Fig 6.2 illustrates the possible configurations for 2-terminal and 3-terminal solar cells, for which the tunnel recombination layer is required. If the bottom cell is a SHJ solar cell, then, in order to avoid the degradation of the aSi layers, low temperature deposition processes below 200 °C should be considered. Moreover, the conventional sputtering of TCOs induces sputter damage, which can be avoided with a soft deposition method, such as ALD. Currently, there are promising results regarding ALD $\text{In}_2\text{O}_3\text{:H}$ [220] and AZO [284], which have similar electrical properties to the sputtered versions.

Despite ALD already being prominent in perovskite solar cell developments, there are still issues with processing that have to be considered. Most perovskite devices have perovskite layers deposited on top of ALD layers. This allows a higher degree of freedom to choose the substrate, deposition temperature, or type of oxidizer for the ALD process. However, it is attractive to grow metal oxide layers directly on top of the perovskite. If the ALD layer is deposited on top of the perovskite, then there is a direct exposure of the perovskite to oxygen, elevated temperature stresses or high levels of moisture, which can all lead to perovskite degradation during the deposition [285]. Additionally, depending on the choice of precursor, there is a possibility of organic cation interaction with the metal-organic precursor during layer growth [286]. Thus, deposition conditions should be chosen carefully, with limited thermal budget and with the choice of a “soft” oxidizer, such as water.

Chapter 7

Conclusions and outlook

The main focus of this thesis is on metal oxide layers and their possible implementation as carrier selective contacts in SHJ solar cells. The dominant topics in this work are the development of deposition processes for such metal oxide layers and their further analysis, covering layer composition, layer properties and their interface with perovskite, c-Si, or aSi:H. Their implementation in solar cell devices, as well as their impact on output performance, were also assessed. Chapters 4 and 5 focus on electron-transport layers for SHJ solar cells deposited by ALD. Additionally, a discussion of a post-treatment process for spin-coated SnO₂ layers for perovskite solar cells was presented in chapter 4. Chapter 6 gave a brief overview of metal oxides as electron-selective contacts and discussed the possibilities and issues of implementing high work function TMO layers in SHJ devices. Furthermore, it presented a general outlook for ALD in SHJ and perovskite solar cells.

Chapter 4 summarizes an investigation of PEALD SnO₂ layers. This chapter covers the development of the deposition process, and the correlation of deposition parameters and layer composition to the opto-electrical properties of SnO₂ layers. It was shown that, for SnO₂ layers deposited by PEALD, residuals from the precursor, such as carbon and nitrogen species, are present at the surface and in the bulk. These residuals are especially prominent for low temperature depositions and have a direct influence on the refractive index and optical band gap of SnO₂ layers. Moreover, this chapter discusses the evolution of the interface between n-aSi:H and SnO₂ layers at different stages of SnO₂ layer growth. The formation of intermediate SiO_x and SnO_x phases was observed during the first stages of the deposition. Additionally, the apparent conduction band offset for this interface was calculated to be 0.55 ± 0.15 eV. However, this value represents not only the offset between the fully formed SnO₂ layer and the n-aSi:H bulk, but also includes the band bending in the SnO₂ film towards the interface, and not the direct interface. Such offset is higher than for comparable metal oxides that can be used as electron-transport layers. This was reflected in the performance of solar cells with implemented PEALD SnO₂ layers, which exhibited a drop in fill factor in comparison to reference SHJ solar cells. This demonstrated that PEALD SnO₂ layers are not suitable as electron-selective contacts in SHJ solar cells.

Furthermore, in a broader overview of SnO₂ layer and surface properties, a post-treatment with oxygen plasma for spin-coated SnO₂ layers was investigated with a focus on implementation in perovskite solar cells. It was demonstrated that, with oxygen plasma exposure, it is feasible to eliminate reduced surface states and contamination at the SnO₂ film surface. Moreover, by introducing the oxygen plasma treatment, an improvement in the band alignment between SnO₂ and perovskite layer can be achieved. This was mirrored by the improved efficiency and decreased hysteresis behaviour of such perovskite solar cells.

Chapter 5 describes the layer properties and device implementation of ALD MgO layers as passivating electron-selective contacts for SHJ solar cells. It was observed that MgO layers do not provide good passivation by themselves on c-Si wafers. Therefore, an intermediate passivation layer was needed to maintain a high V_{OC} in solar cells with MgO layers. In this work, i-aSi:H layers were considered as a passivating buffer layer. The low MgO deposition temperatures (< 200 °C) ensured compatibility with i-aSi:H layers. Regarding layer and interface properties, such as passivation and layer stoichiometry, the main varied parameters in this chapter were: MgO layer thickness, the metallization scheme for the rear side at the MgO layer interface, and the deposition temperature for the MgO layers. Using flat wafers with rear side MgO layers, it was possible to achieve efficiencies of 16.4 % for solar cells with a c-Si/MgO interface, and 17.3 % with an i-aSi:H/MgO interface. Therefore, the ALD MgO layers, presented in this thesis, can be considered as a suitable building block for further development in c-Si based devices.

Finally, chapter 6 discusses current and future topics for research in relation to the results of this thesis. Perspectives and issues regarding implementation are discussed for TMO high work function layers as hole-selective contacts, and low work function metal oxides as electron-selective contacts, for SHJ solar cells. Moreover, an overview of the prospects for metal oxides and ALD in the context of SHJ and perovskite solar cells is presented.

Outlook

In recent years, silicon-based solar cell devices have achieved great success of reaching high efficiencies and reduction of production costs. However, further development is still required in order to minimize recombination and resistance losses at the contacts. To this end, passivating contacts, which allow simultaneously to provide carrier-selectivity and surface

passivation, have become a focus of research. One possible development pathway is the further investigation of dopant-free materials, such as metal oxides, as possible carrier-selective contacts. These layers are attractive for further investigation due to their high transparency and low contact resistance. In the scope of five years, it was possible for the fully dopant-free asymmetric hetero-contact (DASH) solar cells to achieve efficiencies above 20.7 % and for cells with substitution of one of the carrier-selective layer above 22 %, which are not fully comparable in terms of efficiency to mainstream SHJ cells based on doped amorphous silicon layers. They, however, show the promising for the development, due to their simplified deposition processes, in comparison to doped layers. Additionally, these layers have been implemented in integrated back contact solar cells (IBC) and show drastic progress regarding ease of production and efficiency today. Despite these significant improvements and developments, there are many remaining challenges for the further application of these layers in silicon-based devices. These include thermal stability and suitable band alignment, which must be achieved for both electron- and hole-selective contacts. However, there are increasingly more new materials that have been shown to be suitable for further development of solar cells. These include not only oxides, but also sulfides, nitrides and fluorides. Moreover, with further developments of other types of solar cells, such as perovskite devices, there is a possibility of further development of these layers in tandem devices that may surpass existing efficiencies.

With regard to deposition techniques, it can be assumed that ALD will be increasingly more common for PV research and production. By now, CVD and PVD dominate in the field of thin film deposition. However, with the further development of layers, and general trend of layer thickness minimization and precise control over layer properties on large substrates the demands for layer deposition become higher. ALD allows to have high level of control over the thickness and uniformity of the layers with high scalability for thin layers, and simultaneously allows for decreased deposition temperature, while being “soft” damage-free deposition.

Chapter 8

Appendix

8.1 Abbreviations and symbols

Al	Aluminum
ALD	Atomic layer deposition
E_g	Bandgap
$Mg(CpEt)_2$	Bis(ethylcyclopentadienyl)magnesium
Q_i	Carrier concentration at the interface
n	Charge carrier density
c-Si	Crystalline silicon
E_C	Conduction band
ΔE_C	Conduction band offset
CSM	Cox and Strack method
D_{it}	Defect density at the interface
τ_{eff}	Effective charge carrier lifetime
χ	Electron affinity
E_F	Fermi level
FF	Fill factor
GPC	Growth per cycle
HF	Hydrofluoric acid
aSi:H	Hydrogenated amorphous silicon
i-aSi:H	Hydrogenated intrinsic amorphous silicon
IBC	Integrated back contact
iFF	Implied fill factor
iVoc	Implied open circuit voltage
ITO	Indium tin oxide
I	Ionization potential
MgO	Magnesium oxide
n-aSi:H	n-type amorphous silicon

PERC	Passivated emitter and rear cell
j_{ph}	Photocurrent
PL	Photoluminescence
PV	Photovoltaic
PVD	Physical vapor deposition
PEALD	Plasma-enhanced atomic layer deposition
PECVD	Plasma enhanced chemical vapor deposition
PCE	Power conversion efficiency
p-aSi:H	p-type hydrogenated amorphous silicon
RPS	Remote plasma source
R_s	Series resistance
J_{sc}	Short-circuit current density
SHJ	Silicon heterojunction
SiO_x	Silicon oxide with stoichiometry x
V_{oc}	Solar cell open circuit voltage
SPV	Surface photovoltage
TDMASn	Tetrakis(dimethylamino)tin
SnO_2	Tin oxide
TiO_2	Titanium dioxide
Ti-Ag	Titanium-silver
TLM	Transfer length method
TrPCD	Transient photoconductance
TMO	Transition metal oxide
TCO	Transparent conductive oxide
UPS	Ultraviolet electron spectroscopy
E_{vac}	Vacuum level
E_v	Valence band
ΔE_v	Valence band offset
ϕ	Work function
XPS	X-ray photoelectron spectroscopy
ZnO	Zinc oxide

8.2 Publications

Published peer-reviewed articles:

Ganna Chistiakova, Bart Macco, Lars Korte

Low temperature atomic layer deposited magnesium oxide as a passivating electron contact for c-Si based solar cells

IEEE Journal of Photovoltaics 10.2, 398-406 (2020)

Ganna Chistiakova, Mathias Mews, Regan Wilks, Marcus Bär and Lars Korte

In-system photoelectron spectroscopy study of tin oxide layers produced from tetrakis(dimethylamino)tin by plasma enhanced atomic layer deposition

Journal of Vacuum Science & Technology A: Vacuum, Surfaces, and Films 36, 02D401 (2018)

Diego Di Girolamo, Fabio Matteocci, Felix Utama Kosasih, Ganna Chistiakova, Weiwei Zuo, Giorgio Divitini, Lars Korte, Caterina Ducati, Aldo Di Carlo, Danilo Dini and Antonio Abate

Stability and Dark Hysteresis Correlate in NiO-Based Perovskite Solar Cells

Advanced Energy Materials (2019)

Amran Al-Ashouri, Artiom Magomedov, Marcel Roß, Marko Jošt, Martynas Talaikis, Ganna Chistiakova, Tobias Bertram, José A. Márquez, Eike Köhnen, Ernestas Kasparavičius, Sergiu Levcenco, Lidón Gil-Escrig, Charles J. Hages, Rutger Schlatmann, Bernd Rech, Tadas Malinauskas, Thomas Unold, Christian A. Kaufmann, Lars Korte, Gediminas Niaura, Vytautas Getautis and Steve Albrecht

Conformal monolayer contacts with lossless interfaces for perovskite single junction and monolithic tandem solar cells

Energy & Environmental Science 12, 3356 (2018)

Diego Di Girolamo, Nga Phung, Marko Jošt, Amran Al-Ashouri, Ganna Chistiakova, Junming Li, José A. Márquez, Thomas Unold, Lars Korte, Steve Albrecht, Aldo Di Carlo, Danilo Dini, and Antonio Abate

From Bulk to Surface: Sodium Treatment Reduces Recombination at the Nickel Oxide/Perovskite Interface

Advanced Materials Interfaces 6, no. 17 (2019)

César Omar Ramírez Quiroz, George D. Spyropoulos, Michael Salvador, Loïc M. Roch, Marvin Berlinghof, José Darío Perea, Karen Forberich, Laura-Isabelle Dion-Bertrand, Nadine J. Schrenker, Andrej Classen, Nicola Gasparini, Ganna Chistiakova, Mathias Mews, Lars Korte,

Bernd Rech, Ning Li, Frank Hauke, Erdmann Spiecker, Tayebah Ameri, Steve Albrecht, Gonzalo Abellán, Salvador León, Tobias Unruh, Andreas Hirsch, Alán Aspuru-Guzik, and Christoph J. Brabec

Interface Molecular Engineering for Laminated Monolithic Perovskite/Silicon Tandem Solar Cells with 80.4% Fill Factor.

Advanced Functional Materials (2019)

Oral presentations at international conferences:

Ganna Chistiakova, Mathias Mews, Regan Wilks, Lars Korte, Marcus Bär, Bernd Rech

PEALD of Tin Oxide using Tetrakis(Dimethylamino)Tin for photovoltaic applications

E-MRS 2017 Fall, Warsaw – September 19th, 2017

Ganna Chistiakova, Mathias Mews, Lars Korte

Band offset of the heterojunction between plasma enhanced atomic layer deposited SnO₂ and hydrogenated amorphous silicon

MRS 2018 Fall, Boston – November 26th, 2018

Poster presentation at international conferences:

G. Chistiakova, B. Rech, L. Korte

ALD-grown magnesium oxide as a material for silicon heterojunction solar cells

9th International conference on crystalline silicon photovoltaics “Silicon PV”, Leuven, Belgium,
8th April 2019

8.3 Acknowledgments

I would like to thank Prof. Dr. Bernd Rech for the opportunity to work and write my thesis at the institute of silicon photovoltaic.

I would like to thank Prof. Dr. Uwe Rau, Prof. Dr. Klaus Lips and Prof. Dr. Steve Albrecht for being the co-examiners of this doctoral thesis..

I am grateful to Dr. Lars Korte for his excellent and positive supervision, and especially for availability to discuss and answer even minor things and enormous patience, while doing so.

A special thank you to Mathias Mews for the humongous support and plethora of discussions during the experimental work, writing and in general. I also appreciate the patience of reading my first drafts of text and the dose of the healthy sarcasm.

I am grateful to Bart Macco for the help and great discussions about the ALD topic and in general. Moreover, for sharing my enthusiasm about the deposition tool.

I would like to thank Regan Wilks for the help with XPS, UPS measurements and for the assistance with the analysis of the data. Furthermore, Marcus Bär is thanked for the proofreading and fruitful discussions about XPS and UPS.

Many thanks to Johannes Frisch for the assistance and maintaining XPS setup, and occasional help and patience with fallen samples and other problems; Kerstin Jacobs and Mona Wittig for cleaning wafers; Hagen Heinz and Carola Ferber for great support and help in the Hysprint lab. Martin Reiche and Florian Ruske are thanked for the support and maintenance of the AltaCVD tool.

Additional thanks to Philipp Tockhorn for the partnership in tin oxide topic; Amran Al-Ashouri, Diego Di Girolamo and César Omar Ramírez Quiroz for including me in their research projects;

Many thanks to my office roommates Philipp, Nathan and Alvaro for admirable discussions and conversations regarding work and not only. Also I am grateful to Alvaro for the help and discussions about ellipsometry, and, especially, for thorough proofreading of this thesis, and Philipp for help with samples and my occasional stupid questions.

Finally, thanks also to Dorothee, Christoph, Lukas, Claudia, Oleksandra, Martina, Cham, and other colleagues and friends for help, discussions and much more.

Bibliography

- [1] D. Feldman and R. Margolis, “Q4 2018 / Q1 2019 Solar Industry Update,” no. May, 2018.
- [2] Solar Power Europe, “Global Market Outlook: 2019-2023,” p. 92, 2019.
- [3] Fraunhofer, “Photovoltaics Report©Fraunhofer ISE: Photovoltaics Report,” ©*Fraunhofer ISE Photovoltaics Rep.*, vol. 2013, no. March, pp. 1–18, 2016.
- [4] T. Dullweber and J. Schmidt, “Industrial Silicon Solar Cells Applying the Passivated Emitter and Rear Cell (PERC) Concept-A Review,” *IEEE J. Photovoltaics*, vol. 6, no. 5, pp. 1366–1381, 2016.
- [5] F. Feldmann, M. Bivour, C. Reichel, H. Steinkemper, M. Hermle, and S. W. Glunz, “Tunnel oxide passivated contacts as an alternative to partial rear contacts,” *Sol. Energy Mater. Sol. Cells*, vol. 131, pp. 46–50, 2014.
- [6] K. U. Ritzau *et al.*, “TCO work function related transport losses at the a-Si:H/TCO-contact in SHJ solar cells,” *Sol. Energy Mater. Sol. Cells*, vol. 131, pp. 9–13, 2014.
- [7] J. Melskens, B. W. H. Van De Loo, B. Macco, L. E. Black, S. Smit, and W. M. M. Kessels, “Passivating Contacts for Crystalline Silicon Solar Cells: From Concepts and Materials to Prospects,” *IEEE J. Photovoltaics*, vol. 8, no. 2, pp. 373–388, 2018.
- [8] M. Bivour, J. Temmler, H. Steinkemper, and M. Hermle, “Molybdenum and tungsten oxide: High work function wide band gap contact materials for hole selective contacts of silicon solar cells,” *Sol. Energy Mater. Sol. Cells*, vol. 142, pp. 34–41, 2015.
- [9] D. Adachi, J. L. Hernández, and K. Yamamoto, “Impact of carrier recombination on fill factor for large area heterojunction crystalline silicon solar cell with 25.1% efficiency,” *Appl. Phys. Lett.*, vol. 107, no. 23, 2015.
- [10] X. Yang, K. Weber, Z. Hameiri, and S. De Wolf, “Industrially feasible, dopant-free, carrier-selective contacts for high-efficiency silicon solar cells,” *Prog. Photovoltaics Res. Appl.*, vol. 25, no. 11, pp. 896–904, 2017.
- [11] B. Macco *et al.*, “Effective passivation of silicon surfaces by ultrathin atomic-layer deposited niobium oxide,” *Appl. Phys. Lett.*, vol. 112, no. 24, pp. 242105–242101, 2018.
- [12] J. Yu *et al.*, “Heterojunction solar cells with asymmetrically carrier-selective contact structure of molybdenum-oxide/silicon/magnesium-oxide,” *Sol. Energy*, vol. 159, pp. 704–709, Jan. 2018.
- [13] X. Yang *et al.*, “Tantalum Nitride Electron-Selective Contact for Crystalline Silicon Solar Cells,” *Adv. Energy Mater.*, vol. 8, no. 20, p. 1800608, Jul. 2018.

- [14] J. Bullock *et al.*, “Stable Dopant-Free Asymmetric Heterocontact Silicon Solar Cells with Efficiencies above 20%,” *ACS Energy Lett.*, vol. 3, no. 3, pp. 508–513, 2018.
- [15] X. Yang, Q. Bi, H. Ali, K. Davis, W. V. Schoenfeld, and K. Weber, “High-Performance TiO₂-Based Electron-Selective Contacts for Crystalline Silicon Solar Cells,” *Adv. Mater.*, vol. 28, no. 28, pp. 5891–5897, 2016.
- [16] G. Agostinelli *et al.*, “Surface passivation of silicon by means of negative charge dielectrics,” in *Proceedings of the 19th European Photovoltaic Solar Energy Conference, Paris, France, 2004*, vol. 1, pp. 132–134.
- [17] B. W. H. Van De Loo, B. Macco, J. Melskens, M. a Verheijen, and W. M. M. E. Kessels, “Atomic-Layer Deposited Passivation Schemes for c-Si Solar Cells Atomic-Layer Deposited Passivation Schemes for c-Si Solar Cells,” *43rd IEEE Photovoltaics Spec. Conf.*, no. July, pp. 3655–3660, 2016.
- [18] G. Chistiakova, M. Mews, R. G. Wilks, M. Bär, and L. Korte, “In-system photoelectron spectroscopy study of tin oxide layers produced from tetrakis(dimethylamino)tin by plasma enhanced atomic layer deposition,” *J. Vac. Sci. Technol. A Vacuum, Surfaces, Film.*, vol. 36, no. 2, p. 02D401, 2018.
- [19] R. A. Street, *Hydrogenated amorphous silicon*. Cambridge university press, 2005.
- [20] A. H. Mahan, D. L. Williamson, B. P. Nelson, and R. S. Crandall, “Small-angle X-ray scattering studies of microvoids in a-SiC:H and a-Si:H,” *Sol. Cells*, vol. 27, no. 1–4, pp. 465–476, 1989.
- [21] A. Smets and M. van de Sanden, “Relation of the Si-H stretching frequency to the nanostructural Si-H bulk environment,” *Phys. Rev. B*, vol. 76, no. 7, p. 073202, 2007.
- [22] A. H. M. Smets, W. M. M. Kessels, and M. C. M. Van de Sanden, “Vacancies and voids in hydrogenated amorphous silicon,” *Appl. Phys. Lett.*, vol. 82, no. 10, pp. 1547–1549, 2003.
- [23] C. Manfredotti, F. Fizzotti, M. Boero, P. Pastorino, P. Polesello, and E. Vittone, “Influence of hydrogen-bonding configurations on the physical properties of hydrogenated amorphous silicon,” *Phys. Rev. B*, vol. 50, no. 24, pp. 18046–18053, 1994.
- [24] R. E. Norberg, D. J. Leopold, and P. A. Feeders, “Non-bonded hydrogen in a-Si:H,” *J. Non. Cryst. Solids*, vol. 227–230, no. PART 1, pp. 124–127, 1998.
- [25] W. G. J. H. M. van Sark, “Methods of deposition of hydrogenated amorphous silicon for device applications,” *Thin Film. Nanostructures*, vol. 30, no. C, pp. 1–215, 2002.
- [26] H. Meiling, M. J. Van Den Boogaard, R. E. I. Schropp, J. Bezemer, and W. F. Van der Weg, “Hydrogen Dilution of Silane: Correlation Between the Structure and Optical Band Gap in Gd a-Si:H Films,” *MRS Proc.*, vol. 192, pp. 645–650, 1990.

- [27] T. F. Schulze, L. Korte, F. Ruske, and B. Rech, "Band lineup in amorphous/crystalline silicon heterojunctions and the impact of hydrogen microstructure and topological disorder," *Phys. Rev. B - Condens. Matter Mater. Phys.*, vol. 83, no. 16, 2011.
- [28] W. E. Spear and P. G. Le Comber, "Substitutional doping of amorphous silicon," *Solid State Commun.*, vol. 88, no. 11/12, pp. 1015–1018, 1993.
- [29] R. A. Street, "Doping and the fermi energy in amorphous silicon," *Phys. Rev. Lett.*, vol. 49, no. 16, pp. 1187–1190, 1982.
- [30] M. Stutzmann, D. K. Biegelsen, and R. A. Street, "detailed investigation of doping in hydrogenated amorphous silicon and germanium," *Phys. Rev. B*, vol. 35, no. 11, 1987.
- [31] S. De Wolf and M. Kondo, "Nature of doped a-Si:H/c-Si interface recombination," *J. Appl. Phys.*, vol. 105, no. 10, 2009.
- [32] R. W. Collins, "In situ study of p-type amorphous silicon growth from B₂H₆:SiH₄ mixtures: Surface reactivity and interface effects," *Appl. Phys. Lett.*, vol. 53, no. 12, pp. 1086–1088, 1988.
- [33] J. Huang, N. Matsunaga, K. Shimano, N. Yamazoe, and T. Kunitake, "Nanotubular SnO₂ templated by cellulose fibers: Synthesis and gas sensing," *Chem. Mater.*, vol. 17, no. 13, pp. 3513–3518, 2005.
- [34] P. Meduri, C. Pendyala, V. Kumar, G. U. Sumanasekera, and M. K. Sunkara, "Hybrid Tin Oxide Nanowires as Stable and High Capacity Anodes for Li-Ion Batteries," *Nano Lett.*, vol. 9, no. 2, pp. 612–616, 2009.
- [35] L. Zheng *et al.*, "Network structured SnO₂/ZnO heterojunction nanocatalyst with high photocatalytic activity," *Inorg. Chem.*, vol. 48, no. 5, pp. 1819–1825, 2009.
- [36] S. Trost, K. Zilberberg, A. Behrendt, and T. Riedl, "Room-temperature solution processed SnO_x as an electron extraction layer for inverted organic solar cells with superior thermal stability," *J. Mater. Chem.*, vol. 22, no. 32, p. 16224, 2012.
- [37] Ç. Kılıç and A. Zunger, "Origins of coexistence of conductivity and transparency in SnO₂," *Phys. Rev. Lett.*, vol. 88, no. 9, pp. 955011–955014, 2002.
- [38] M. Batzill and U. Diebold, "The surface and materials science of tin oxide," *Prog. Surf. Sci.*, vol. 79, no. 2–4, pp. 47–154, 2005.
- [39] J. A. Caraveo-Frescas, P. K. Nayak, H. A. Al-Jawhari, D. B. Granato, U. Schwingenschlögl, and H. N. Alshareef, "Record mobility in transparent p-type tin monoxide films and devices by phase engineering," *ACS Nano*, vol. 7, no. 6, pp. 5160–5167, 2013.
- [40] J. Tupala *et al.*, "Atomic layer deposition of tin oxide thin films from bis[bis(trimethylsilyl)amino]tin(II) with ozone and water," *J. Vac. Sci. Technol. A Vacuum, Surfaces, Film.*, vol. 35, no. 4, p. 041506, 2017.

- [41] C. Wright *et al.*, “Tin Oxides: Insights into Chemical States from a Nanoparticle Study,” *J. Phys. Chem. C*, vol. 121, no. 35, pp. 19414–19419, 2017.
- [42] J. M. Themlin, M. Chtaïb, L. Henrard, P. Lambin, J. Darville, and J. M. Gilles, “Characterization of tin oxides by x-ray-photoemission spectroscopy,” *Phys. Rev. B*, vol. 46, no. 4, pp. 2460–2466, 1992.
- [43] P. Ágoston, K. Albe, R. M. Nieminen, and M. J. Puska, “Intrinsic n-type behavior in transparent conducting oxides: A comparative hybrid-functional study of In₂O₃, SnO₂, and ZnO,” *Phys. Rev. Lett.*, vol. 103, no. 24, p. 245501, 2009.
- [44] S. Samson and C. G. Fonstad, “Defect structure and electronic donor levels in stannic oxide crystals,” *J. Appl. Phys.*, vol. 44, no. 10, pp. 4618–4621, 1973.
- [45] W. M. Hlaing Oo, S. Tabatabaei, M. D. McCluskey, J. B. Varley, A. Janotti, and C. G. Van De Walle, “Hydrogen donors in SnO₂ studied by infrared spectroscopy and first-principles calculations,” *Phys. Rev. B - Condens. Matter Mater. Phys.*, vol. 82, no. 19, p. 193201, 2010.
- [46] C. Zhang *et al.*, “Influence of interface textures on light management in thin-film silicon solar cells with intermediate reflector,” *IEEE J. Photovoltaics*, vol. 5, no. 1, pp. 33–39, 2015.
- [47] Z. C. Holman *et al.*, “Current losses at the front of silicon heterojunction solar cells,” *IEEE J. Photovoltaics*, vol. 2, no. 1, pp. 7–15, 2012.
- [48] M. Tadatsugu, “New n-Type transparent conducting oxides,” *MRS Bull.*, vol. 25, no. 8, pp. 38–44, 2000.
- [49] J. P. Correa Baena *et al.*, “Highly efficient planar perovskite solar cells through band alignment engineering,” *Energy Environ. Sci.*, vol. 8, no. 10, pp. 2928–2934, 2015.
- [50] Y. Lee *et al.*, “Enhanced charge collection with passivation of the tin oxide layer in planar perovskite solar cells,” *J. Mater. Chem. A*, vol. 5, no. 25, pp. 12729–12734, 2017.
- [51] T. Hu *et al.*, “Indium-Free Perovskite Solar Cells Enabled by Impermeable Tin-Oxide Electron Extraction Layers,” *Adv. Mater.*, vol. 29, no. 27, p. 1606656, Jul. 2017.
- [52] C. Wang *et al.*, “Low-temperature plasma-enhanced atomic layer deposition of tin oxide electron selective layers for highly efficient planar perovskite solar cells,” *J. Mater. Chem. A*, vol. 4, no. 31, pp. 12080–12087, 2016.
- [53] K. a. Bush *et al.*, “23.6%-Efficient Monolithic Perovskite/Silicon Tandem Solar Cells With Improved Stability,” *Nat. Energy*, vol. 2, no. 4, p. 17009, 2017.
- [54] S. Albrecht *et al.*, “Monolithic perovskite/silicon-heterojunction tandem solar cells processed at low temperature,” *Energy Environ. Sci.*, vol. 9, no. 1, pp. 81–88, 2016.

- [55] T. Jüstel and H. Nikol, "Optimization of luminescent materials for plasma display panels," *Adv. Mater.*, vol. 12, no. 7, pp. 527–530, 2000.
- [56] H. Kubota *et al.*, "Quantitative measurement of voltage dependence of spin-transfer torque in MgO-based magnetic tunnel junctions," *Nat. Phys.*, vol. 4, no. 1, pp. 37–41, 2008.
- [57] O. E. Taurian, M. Springborg, and N. E. Christensen, "Self-consistent electronic structures of MgO and SrO," *Solid State Commun.*, vol. 55, no. 4, pp. 351–355, Jul. 1985.
- [58] A. N. M. Green, E. Palomares, S. A. Haque, J. M. Kroon, and J. R. Durrant, "Charge Transport versus Recombination in Dye-Sensitized Solar Cells Employing Nanocrystalline TiO₂ and SnO₂ Films," *J. Phys. Chem. B*, vol. 109, no. 25, pp. 12525–12533, 2005.
- [59] A. Kay and M. Grätzel, "Dye-sensitized core-shell nanocrystals: Improved efficiency of mesoporous tin oxide electrodes coated with a thin layer of an insulating oxide," *Chem. Mater.*, vol. 14, no. 7, pp. 2930–2935, 2002.
- [60] Y. Wan *et al.*, "Conductive and Stable Magnesium Oxide Electron-Selective Contacts for Efficient Silicon Solar Cells," *Adv. Energy Mater.*, vol. 7, no. 5, p. 1601863, Mar. 2017.
- [61] J. Yu *et al.*, "Activating and optimizing evaporation-processed magnesium oxide passivating contact for silicon solar cells," *Nano Energy*, vol. 62, pp. 181–188, 2019.
- [62] H. Lee, T. Kamioka, D. Zhang, N. Iwata, and Y. Ohshita, "Excellent Surface Passivation of Crystalline Silicon by Ternary Al_xMg_{1-x}O_y Thin Films," *IEEE 43rd Photovolt. Spec. Conf.*, pp. 2931–2934, 2016.
- [63] S. G. Kim, J. Y. Kim, and H. J. Kim, "Deposition of MgO thin films by modified electrostatic spray pyrolysis method," *Thin Solid Films*, vol. 376, no. 1–2, pp. 110–114, 2000.
- [64] M. Foster, M. Furse, and D. Passno, "An FTIR study of water thin films on magnesium oxide," *Surf. Sci.*, vol. 502–503, pp. 102–108, 2002.
- [65] P. Liu, T. Kendelewicz, G. E. Brown, and G. A. Parks, "Reaction of water with MgO(100) surfaces. Part I: Synchrotron X-ray photoemission studies of low-defect surfaces," *Surf. Sci.*, vol. 412, pp. 287–314, 1998.
- [66] J. H. Lee, J. H. Eun, S. Y. Park, S. G. Kim, and H. J. Kim, "Hydration of r.f. magnetron sputtered MgO thin films for a protective layer in AC plasma display panel," *Thin Solid Films*, vol. 435, no. 1–2, pp. 95–101, 2003.
- [67] P. Würfel, *Physics of Solar Cells*. Wiley, 2005.
- [68] A. Klein, "Energy band alignment at interfaces of semiconducting oxides: A review of experimental determination using photoelectron spectroscopy and comparison with

- theoretical predictions by the electron affinity rule, charge neutrality levels, and the common anion,” in *Thin Solid Films*, 2012, vol. 520, no. 10, pp. 3721–3728.
- [69] M. Mews, M. Liebhaber, B. Rech, and L. Korte, “Valence band alignment and hole transport in amorphous/crystalline silicon heterojunction solar cells,” *Appl. Phys. Lett.*, vol. 107, no. 013902, 2015.
- [70] R. L. Anderson, “Experiments on Ge-GaAs Heterojunctions,” in *Electronic Structure of Semiconductor Heterojunctions Springer, Dordrecht*, vol. 5, 1988, pp. 35–48.
- [71] O. Lang, A. Klein, C. Pettenkofer, W. Jaegermann, and A. Chevy, “Band lineup of lattice mismatched InSe/GaSe quantum well structures prepared by van der Waals epitaxy: Absence of interfacial dipoles,” *J. Appl. Phys.*, vol. 80, no. 7, pp. 3817–3821, 1996.
- [72] J. Tersoff, “Theory of semiconductor heterojunctions: The role of quantum dipoles,” *Phys. Rev. B*, vol. 30, no. 8, pp. 4874–4877, 1984.
- [73] J. Tersoff, “Band lineups at II-VI heterojunctions: Failure of the common-anion rule,” *Phys. Rev. Lett.*, vol. 56, no. 25, pp. 2755–2758, 1986.
- [74] Y. C. Ruan, N. Wu, X. Jiang, and W. Y. Ching, “An improved effective dipole theory for band lineups in semiconductor heterojunctions,” *J. Appl. Phys.*, vol. 64, no. 3, pp. 1271–1273, 1988.
- [75] S. Miyazaki, J. Schäfer, J. Ristein, and L. Ley, “Surface Fermi level position of hydrogen passivated Si(111) surfaces,” *Appl. Phys. Lett.*, vol. 68, no. 9, pp. 1247–1249, 1996.
- [76] S. J. Baik and K. S. Lim, “Nitrogen plasma treatment of fluorine-doped tin oxide for enhancement of photo-carrier collection in amorphous Si solar cells,” *J. Appl. Phys.*, vol. 109, no. 8, p. 84506, 2011.
- [77] S. Rein, *Lifetime Spectroscopy*, vol. 85. Berlin/Heidelberg: Springer-Verlag, 2005.
- [78] W. Shockley, “The Theory of p-n Junctions in Semiconductors and p-n Junction Transistors,” *Bell Syst. Tech. J.*, vol. 28, no. 3, pp. 435–489, 1949.
- [79] A. Richter, M. Hermle, and S. W. Glunz, “Reassessment of the limiting efficiency for crystalline silicon solar cells,” *IEEE J. Photovoltaics*, vol. 3, no. 4, pp. 1184–1191, 2013.
- [80] K. Yoshikawa *et al.*, “Silicon heterojunction solar cell with interdigitated back contacts for a photoconversion efficiency over 26%,” *Nat. Energy*, vol. 2, no. 5, pp. 1–8, 2017.
- [81] M. A. Green, “Limits on the Open-circuit Voltage and Efficiency of Silicon Solar Cells Imposed by Intrinsic Auger Processes,” *IEEE Trans. Electron Devices*, no. 5, p. 611, 1984.

- [82] R. V. K. Chavali, S. De Wolf, and M. A. Alam, "Device physics underlying silicon heterojunction and passivating-contact solar cells: A topical review," *Prog. Photovoltaics Res. Appl.*, vol. 26, no. 4, pp. 241–260, 2018.
- [83] R. Saive, "S-Shaped Current–Voltage Characteristics in Solar Cells: A Review," *IEEE J. Photovoltaics*, vol. 9, no. 6, pp. 1477–1484, Nov. 2019.
- [84] R. Röler, C. Leendertz, L. Korte, N. Mingirulli, and B. Rech, "Impact of the transparent conductive oxide work function on injection-dependent a-Si:H/c-Si band bending and solar cell parameters," *J. Appl. Phys.*, vol. 113, no. 14, 2013.
- [85] M. A. Green, "Solar cells: operating principles, technology, and system applications," *Englewood Cliffs, NJ, Prentice-Hall, Inc., 1982. 288 p.*, 1982.
- [86] S. DeWolf, A. Descoedres, Z. C. Holman, and C. Ballif, "High-efficiency silicon heterojunction solar cells: A review," *Green*, vol. 2, no. 1, pp. 7–24, 2012.
- [87] A. Descoedres, Z. C. Holman, L. Barraud, S. Morel, S. De Wolf, and C. Ballif, ">21% efficient silicon heterojunction solar cells on n-and p-type wafers compared," *IEEE J. Photovoltaics*, vol. 3, no. 1, pp. 83–89, 2013.
- [88] J. Haschke, O. Dupré, M. Boccard, and C. Ballif, "Silicon heterojunction solar cells: Recent technological development and practical aspects - from lab to industry," *Sol. Energy Mater. Sol. Cells*, vol. 187, pp. 140–153, 2018.
- [89] Y. Tsunomura *et al.*, "Twenty-two percent efficiency HIT solar cell," *Sol. Energy Mater. Sol. Cells*, vol. 93, no. 6–7, pp. 670–673, 2009.
- [90] M. R. Page *et al.*, "Amorphous/crystalline silicon heterojunction solar cells with varying i-layer thickness," *Thin Solid Films*, vol. 519, no. 14, pp. 4527–4530, 2011.
- [91] A. Kanevce and W. K. Metzger, "The role of amorphous silicon and tunneling in heterojunction with intrinsic thin layer (HIT) solar cells," *J. Appl. Phys.*, vol. 105, no. 9, 2009.
- [92] J. Pla *et al.*, "Optimization of ITO layers for applications in a-Si_{1-x}Ge_x-Si heterojunction solar cells," *Thin Solid Films*, vol. 425, pp. 185–192, 2003.
- [93] Z. C. Holman *et al.*, "Infrared light management in high-efficiency silicon heterojunction and rear-passivated solar cells," *J. Appl. Phys.*, vol. 113, no. 1, 2013.
- [94] T. Mishima, M. Taguchi, H. Sakata, and E. Maruyama, "Development status of high-efficiency HIT solar cells," *Sol. Energy Mater. Sol. Cells*, vol. 95, no. 1, pp. 18–21, Jan. 2011.
- [95] M. Mews, A. Lemaire, and L. Korte, "Sputtered Tungsten Oxide as Hole Contact for Silicon Heterojunction Solar Cells," *IEEE J. Photovoltaics*, vol. 7, no. 5, pp. 1209–1215, 2017.

- [96] J. Bullock, A. Cuevas, T. Allen, and C. Battaglia, "Molybdenum oxide MoO_x: A versatile hole contact for silicon solar cells," *Appl. Phys. Lett.*, vol. 105, no. 23, 2014.
- [97] X. Yang and K. Weber, "N-type silicon solar cells featuring an electron-selective TiO₂ contact," in *2015 IEEE 42nd Photovoltaic Specialist Conference, PVSC 2015*, 2015.
- [98] W. Kern, "The Evolution of Silicon Wafer Cleaning Technology," *J. Electrochem. Soc.*, vol. 137, no. 6, p. 1887, 1990.
- [99] A. Descoedres *et al.*, "The silane depletion fraction as an indicator for the amorphous/crystalline silicon interface passivation quality," *Appl. Phys. Lett.*, vol. 97, no. 18, 2010.
- [100] J. Damon-Lacoste and P. Roca I Cabarrocas, "Toward a better physical understanding of a-Si:H/c-Si heterojunction solar cells," *J. Appl. Phys.*, vol. 105, no. 6, 2009.
- [101] A. Descoedres *et al.*, "Improved amorphous/crystalline silicon interface passivation by hydrogen plasma treatment," *Appl. Phys. Lett.*, vol. 99, no. 12, p. 123506, 2011.
- [102] M. Mews, T. F. Schulze, N. Mingirulli, and L. Korte, "Hydrogen plasma treatments for passivation of amorphous-crystalline silicon-heterojunctions on surfaces promoting epitaxy," *Appl. Phys. Lett.*, vol. 102, no. 12, pp. 1–4, 2013.
- [103] R. L. Puurunen, "Growth per cycle in atomic layer deposition: A theoretical model," *Chem. Vap. Depos.*, vol. 9, no. 5, pp. 249–257, 2003.
- [104] G. Dingemans and W. M. M. Kessels, "Status and prospects of Al₂O₃-based surface passivation schemes for silicon solar cells," *J. Vac. Sci. Technol. A Vacuum, Surfaces, Film.*, vol. 30, no. 4, p. 040802, 2012.
- [105] M. Leskelä and M. Ritala, "Atomic Layer Deposition Chemistry: Recent Developments and Future Challenges," *Angew. Chemie - Int. Ed.*, vol. 42, no. 45, pp. 5548–5554, 2003.
- [106] R. L. Puurunen, "Surface chemistry of atomic layer deposition: A case study for the trimethylaluminum/water process," *J. Appl. Phys.*, vol. 97, no. 12, pp. 1–52, 2005.
- [107] S. M. George, "Atomic layer deposition: An overview," *Chem. Rev.*, vol. 110, no. 1, pp. 111–131, 2010.
- [108] M. Leskelä and M. Ritala, "Atomic layer deposition (ALD): From precursors to thin film structures," *Thin Solid Films*, vol. 409, no. 1, pp. 138–146, 2002.
- [109] Q. Xie *et al.*, "Growth kinetics and crystallization behavior of TiO₂ films prepared by plasma enhanced atomic layer deposition," *J. Electrochem. Soc.*, vol. 155, no. 9, pp. 688–692, 2008.
- [110] M. D. Groner, F. H. Fabreguette, J. W. Elam, and S. M. George, "Low-Temperature Al₂O₃ Atomic Layer Deposition," *Chem. Mater.*, vol. 16, no. 4, pp. 639–645, 2004.

- [111] M. Ylilammi, "Monolayer thickness in atomic layer deposition," *Thin Solid Films*, vol. 279, no. 1–2, pp. 124–130, 1996.
- [112] M. B. M. Mousa, C. J. Oldham, J. S. Jur, and G. N. Parsons, "Effect of temperature and gas velocity on growth per cycle during Al₂O₃ and ZnO atomic layer deposition at atmospheric pressure," *J. Vac. Sci. Technol. A Vacuum, Surfaces, Film.*, vol. 30, no. 1, p. 01A155, 2012.
- [113] V. Vandalon and W. M. M. Kessels, "What is limiting low-temperature atomic layer deposition of Al₂O₃? A vibrational sum-frequency generation study," *Appl. Phys. Lett.*, vol. 108, no. 1, pp. 1–6, 2016.
- [114] H. B. Profijt, S. E. Potts, M. C. M. van de Sanden, and W. M. M. Kessels, "Plasma-Assisted Atomic Layer Deposition: Basics, Opportunities, and Challenges," *J. Vac. Sci. Technol. A Vacuum, Surfaces, Film.*, vol. 29, no. 5, p. 050801, 2011.
- [115] S. Sioncke *et al.*, "Thermal and plasma enhanced atomic layer deposition of Al₂O₃ on GaAs substrates," *J. Electrochem. Soc.*, vol. 156, no. 4, 2009.
- [116] J. W. Lim and J. S. Yun, "Electrical properties of alumina films by plasma-enhanced atomic layer deposition," *Electrochem. Solid-State Lett.*, vol. 7, no. 8, pp. 45–48, 2004.
- [117] J. L. Van Hemmen *et al.*, "Plasma and Thermal ALD of Al₂O₃ in a Commercial 200 mm ALD Reactor," *J. Electrochem. Soc.*, vol. 154, no. 7, pp. G165–G169, 2007.
- [118] T. O. Kääriäinen and D. C. Cameron, "Plasma-Assisted Atomic Layer Deposition of Al₂O₃ at Room Temperature," *Plasma Process. Polym.*, vol. 6, no. S1, pp. S237–S241, Jun. 2009.
- [119] H. C. M. Knoops, a. J. M. Mackus, M. E. Donders, M. C. M. Van De Sanden, P. H. L. Notten, and W. M. M. Kessels, "Remote plasma and thermal ALD of platinum and platinum oxide films," *ECS Trans.*, vol. 16, no. 4, pp. 209–218, 2008.
- [120] Y. Lee *et al.*, "Effect of nitrogen incorporation in HfO₂ films deposited by plasma-enhanced atomic layer deposition," *J. Electrochem. Soc.*, vol. 153, no. 4, pp. 353–357, 2006.
- [121] B. H. Kim, W. S. Jeon, S. H. Jung, and B. T. Ahn, "Interstitial oxygen incorporation into silicon substrate during plasma enhanced atomic layer deposition of Al₂O₃," *Electrochem. Solid-State Lett.*, vol. 8, no. 10, pp. 294–296, 2005.
- [122] H. B. Profijt, P. Kudlacek, M. C. M. van de Sanden, and W. M. M. Kessels, "Ion and Photon Surface Interaction during Remote Plasma ALD of Metal Oxides," *J. Electrochem. Soc.*, vol. 158, no. 4, pp. 88–91, 2011.
- [123] B. Demarex, S. De Wolf, A. Descoeurdes, Z. Charles Holman, and C. Ballif, "Damage at hydrogenated amorphous/crystalline silicon interfaces by indium tin oxide overlayer sputtering," *Appl. Phys. Lett.*, vol. 101, no. 17, 2012.

- [124] J. F. Moulder, W. F. Stickle, P. E. Sobol, and K. D. Bomben, *Handbook of X-ray photoelectron spectroscopy: a reference book of standard spectra for identification and interpretation of XPS data*. 1992.
- [125] J. F. Watts and J. Wolstenholme, *An Introduction to Surface Analysis by XPS and AES*. 2003.
- [126] M. P. Seah and W. A. Dench, “Quantitative electron spectroscopy of surfaces: A standard data base for electron inelastic mean free paths in solids,” *Surf. Interface Anal.*, vol. 1, no. 1, pp. 2–11, 1979.
- [127] J. C. Dupin, D. Gonbeau, P. Vinatier, and A. Levasseur, “Systematic XPS studies of metal oxides, hydroxides and peroxides,” *Phys. Chem. Chem. Phys.*, vol. 2, no. 6, pp. 1319–1324, 2000.
- [128] A. G. Shard, “Detection limits in XPS for more than 6000 binary systems using Al and Mg K α X-rays,” *Surf. Interface Anal.*, vol. 46, no. 3, pp. 175–185, 2014.
- [129] M. Wojdyr, “Fityk: A general-purpose peak fitting program,” *J. Appl. Crystallogr.*, vol. 43, no. 5 PART 1, pp. 1126–1128, 2010.
- [130] S. a. Chambers, T. Droubay, T. C. Kaspar, and M. Gutowski, “Experimental determination of valence band maxima for SrTiO₃, TiO₂, and SrO and the associated valence band offsets with Si(001),” *J. Vac. Sci. Technol. B Microelectron. Nanom. Struct.*, vol. 22, no. 4, p. 2205, 2004.
- [131] M. Mews, L. Korte, and B. Rech, “Oxygen vacancies in tungsten oxide and their influence on tungsten oxide/silicon heterojunction solar cells,” *Sol. Energy Mater. Sol. Cells*, vol. 158, pp. 77–83, 2016.
- [132] L. G. Gerling, C. Voz, R. Alcubilla, and J. Puigdollers, “Origin of passivation in hole-selective transition metal oxides for crystalline silicon heterojunction solar cells,” *J. Mater. Res.*, vol. 32, no. 2, pp. 260–268, 2017.
- [133] M. T. Nichols *et al.*, “Measurement of bandgap energies in low-k organosilicates,” *J. Appl. Phys.*, vol. 115, no. 9, 2014.
- [134] J. Shewchun, R. Singh, and M. A. Green, “Theory of metal-insulator-semiconductor solar cells,” *J. Appl. Phys.*, vol. 48, no. 2, pp. 765–770, 1977.
- [135] M. P. Seah, “The quantitative analysis of surfaces by XPS: A review,” *Surf. Interface Anal.*, vol. 2, no. 6, pp. 222–239, 1980.
- [136] M. P. Seah and S. J. Spencer, “Ultrathin SiO₂ on Si IV. Intensity measurement in XPS and deduced thickness linearity,” *Surf. Interface Anal.*, vol. 35, no. 6, pp. 515–524, 2003.
- [137] E. A. Kraut, R. W. Grant, J. R. Waldrop, and S. P. Kowalczyk, “Semiconductor core-level to valence-band maximum binding-energy differences: precise determination by x-ray photoelectron spectroscopy,” *Phys. Rev. B*, vol. 28, no. 4, 1983.

- [138] E. A. Kraut, R. W. Grant, J. R. Waldrop, and S. P. Kowalczyk, "Precise Determination of the Valence-Band Edge in X-Ray Photoemission Spectra: Application to Measurement of Semiconductor Interface Potentials," *Phys. Rev. Lett.*, vol. 44, no. 24, pp. 1620–1623, 1980.
- [139] K. Heilig, "Determination of doping factor, mobility ratio and excess concentration using photovoltages at extreme band bendings," *Solid State Electron.*, vol. 21, no. 7, pp. 975–980, 1978.
- [140] L. Kronik, M. Leibovitch, E. Fefer, L. Burstein, and Y. Shapira, "Quantitative surface photovoltage spectroscopy of semiconductor interfaces," *J. Electron. Mater.*, vol. 24, no. 4, pp. 379–385, 1995.
- [141] L. Korte, A. Laades, K. Lauer, R. Stangl, D. Schaffarzik, and M. Schmidt, "Surface photovoltage investigation of recombination at the a-Si/c-Si heterojunction," *Thin Solid Films*, vol. 517, no. 23, pp. 6396–6400, 2009.
- [142] D. K. Schroder, "Surface voltage and surface photovoltage: history, theory and applications," *Meas. Sci. Technol.*, vol. 12, no. 3, pp. R16–R31, 2001.
- [143] R. A. Sinton and A. Cuevas, "Contactless determination of current-voltage characteristics and minority-carrier lifetimes in semiconductors from quasi-steady-state photoconductance data," *Appl. Phys. Lett.*, vol. 69, no. 17, pp. 2510–2512, 1996.
- [144] M. Leilaouioun and Z. C. Holman, "Accuracy of expressions for the fill factor of a solar cell in terms of open-circuit voltage and ideality factor," *J. Appl. Phys.*, vol. 120, no. 12, p. 123111, 2016.
- [145] Y. Y. Chen *et al.*, "Field-effect passivation and degradation analyzed with photoconductance decay measurements," *Appl. Phys. Lett.*, vol. 104, no. 19, 2014.
- [146] C. Leendertz, N. Mingirulli, T. F. Schulze, J. P. Kleider, B. Rech, and L. Korte, "Physical insight into interface passivation of a-Si:H/c-Si heterostructures by analysis of injection-dependent lifetime and band bending," in *25th European Photovoltaic Solar Energy Conference and Exhibition*, 2010, p. 1377.
- [147] C. Leendertz, N. Mingirulli, T. F. Schulze, J. P. Kleider, B. Rech, and L. Korte, "Discerning passivation mechanisms at a-Si:H/c-Si interfaces by means of photoconductance measurements," *Appl. Phys. Lett.*, vol. 98, no. 20, 2011.
- [148] R. A. Sinton and A. Cuevas, "A quasi-steady-state open-circuit voltage method for solar cell characterization," in *16th European Photovoltaic Solar Energy Conference*, 2000, no. May, pp. 1–4.
- [149] D. Pysch, A. Mette, and S. W. Glunz, "A review and comparison of different methods to determine the series resistance of solar cells," *Sol. Energy Mater. Sol. Cells*, vol. 91, no. 18, pp. 1698–1706, 2007.

- [150] T. Trupke, B. Mitchell, J. W. Weber, W. McMillan, R. a. Bardos, and R. Kroeze, "Photoluminescence imaging for photovoltaic applications," *Energy Procedia*, vol. 15, no. 2011, pp. 135–146, 2012.
- [151] G. Abowitz and E. Arnold, "Simple mercury drop electrode for MOS measurements," *Review of Scientific Instruments*, vol. 38, no. 4, pp. 564–565, 1967.
- [152] J. W. Elam, D. Routkevitch, and S. M. Goerge, "Properties of ZnO/Al₂O₃ alloy films grown using atomic layer deposition techniques," *J. Electrochem. Soc.*, vol. 150, no. 6, pp. 339–347, 2003.
- [153] C. R. Barriers, "Contact Resistance and Schottky Barriers," *Semicond. Mater. Device Charact.*, pp. 127–184, 2005.
- [154] S. S. Cohen, "Contact resistance and methods for its determination," *Thin Solid Films*, vol. 104, no. 3–4, pp. 361–379, 1983.
- [155] D. K. Schroder and D. L. Meier, "Contact resistance: Its measurement and relative importance to power loss in a solar cell," *IEEE Trans. Electron Devices*, vol. 31, no. 5, pp. 647–653, 1984.
- [156] H. Schade and Z. E. Smith, "Contact resistance measurements for hydrogenated amorphous silicon solar cell structures," *J. Appl. Phys.*, vol. 59, no. 5, pp. 1682–1687, 1986.
- [157] R. H. Cox and H. Strack, "Ohmic contacts for GaAs devices," *Solid. State. Electron.*, vol. 10, no. 12, pp. 1213–1218, 1967.
- [158] J. Jung, J. Bork, T. Holmgaard, and N. a. Kortbek, "Ellipsometry," *Aalborg Univ. Proj.*, p. 132, 2004.
- [159] H. Fujiwara and R. W. Collins, *Spectroscopic Ellipsometry for Photovoltaics - volume 1: Fundamental Principles and Solar Cell Characterization*, vol. 212. 2018.
- [160] E. Langereis, S. B. S. Heil, H. C. M. Knoops, W. Keuning, M. C. M. van de Sanden, and W. M. M. Kessels, "In situ spectroscopic ellipsometry as a versatile tool for studying atomic layer deposition," *J. Phys. D. Appl. Phys.*, vol. 42, no. 7, p. 073001, 2009.
- [161] E. Langereis, J. Keijmel, M. C. M. Van De Sanden, and W. M. M. Kessels, "Surface chemistry of plasma-assisted atomic layer deposition of Al₂O₃ studied by infrared spectroscopy," *Appl. Phys. Lett.*, vol. 92, no. 23, pp. 231904–131505, 2008.
- [162] J. T. Gudmundsson and E. G. Thorsteinsson, "Oxygen discharges diluted with argon: dissociation processes," *Plasma Sources Sci. Technol.*, vol. 16, pp. 399–412, 2007.
- [163] J. W. Elam, D. a. Baker, A. J. Hryn, A. B. F. Martinson, M. J. Pellin, and J. T. Hupp, "Atomic layer deposition of tin oxide films using tetrakis(dimethylamino) tin," *J. Vac. Sci. Technol. A Vacuum, Surfaces, Film.*, vol. 26, no. 2008, p. 244, 2008.

- [164] D. W. Choi and J. S. Park, "Highly conductive SnO₂ thin films deposited by atomic layer deposition using tetrakis-dimethyl-amine-tin precursor and ozone reactant," *Surf. Coatings Technol.*, vol. 259, pp. 238–243, 2014.
- [165] M. N. Mullings, C. Hägglund, and S. F. Bent, "Tin oxide atomic layer deposition from tetrakis(dimethylamino)tin and water," *J. Vac. Sci. Technol. A Vacuum, Surfaces, Film.*, vol. 31, no. 6, p. 061503, 2013.
- [166] E. Shanthi, a. Banerjee, V. Dutta, and K. L. Chopra, "Annealing characteristics of tin oxide films prepared by spray pyrolysis," *Thin Solid Films*, vol. 71, no. 2, pp. 237–244, 1980.
- [167] B. Alterkop, N. Parkansky, S. Goldsmith, and R. L. Boxman, "Effect of air annealing on opto-electrical properties of amorphous tin oxide films," *J. Phys. D. Appl. Phys.*, vol. 36, no. 5, pp. 552–558, 2003.
- [168] J. J. Chance and W. C. Purdy, "Fabrication of Carboxylic Acid-Terminated Thin Films Using Poly(ethyleneimine) on a Gold Surface," *Langmuir*, vol. 7463, no. 21, pp. 4487–4489, 1997.
- [169] E. L. Bruner, A. R. Span, S. L. Bernasek, and J. Schwartz, "The reaction between tetrakis(diethylamino)tin and indium tin oxide," *Langmuir*, vol. 17, no. 18, pp. 5696–5702, 2001.
- [170] D. Choi, W. J. Maeng, and J.-S. Park, "The conducting tin oxide thin films deposited via atomic layer deposition using Tetrakis-dimethylamino tin and peroxide for transparent flexible electronics," *Appl. Surf. Sci.*, vol. 313, pp. 585–590, 2014.
- [171] Y. Pan, F. Inam, M. Zhang, and D. A. Drabold, "Atomistic origin of Urbach tails in amorphous silicon," *Phys. Rev. Lett.*, vol. 100, no. 20, p. 206403, 2008.
- [172] W. Liu, X. Cao, Y. Zhu, and L. Cao, "Effect of dopants on the electronic structure of SnO₂ thin film," *Sensors Actuators, B Chem.*, vol. 66, no. 1, pp. 219–221, 2000.
- [173] S. Franke *et al.*, "Alumina films as gas barrier layers grown by spatial atomic layer deposition with trimethylaluminum and different oxygen sources," *J. Vac. Sci. Technol. A Vacuum, Surfaces, Film.*, vol. 35, no. 1, p. 01B117, 2017.
- [174] W.-K. Choi, H.-J. Jung, and S.-K. Koh, "Chemical shifts and optical properties of tin oxide films grown by a reactive ion assisted deposition," *J. Vac. Sci. Technol. A Vacuum, Surfaces, Film.*, vol. 14, no. 2, pp. 359–366, 1996.
- [175] R. Matero, a Rahtu, M. Ritala, M. Leskelä, and T. Sajavaara, "Effect of water dose on the atomic layer deposition rate of oxide thin films," *Thin Solid Films*, vol. 368, no. 2000, pp. 1–7, 2000.
- [176] M. Fondell, M. Gorgoi, M. Boman, and a. Lindblad, "An HAXPES study of Sn, SnS, SnO and SnO₂," *J. Electron Spectros. Relat. Phenomena*, vol. 195, pp. 195–199, 2014.

- [177] J. Werner *et al.*, “Parasitic Absorption Reduction in Metal Oxide-Based Transparent Electrodes: Application in Perovskite Solar Cells,” *ACS Appl. Mater. Interfaces*, vol. 8, no. 27, pp. 17260–17267, 2016.
- [178] H. Cachet, J. Bruneaux, G. Folcher, C. Lévy-Clément, C. Vard, and M. Neumann-Spallart, “n-Si/SnO₂ junctions based on macroporous silicon for photoconversion,” *Sol. Energy Mater. Sol. Cells*, vol. 46, no. 2, pp. 101–114, 1997.
- [179] M. Kwoka, L. Ottaviano, M. Passacantando, S. Santucci, and J. Szuber, “XPS depth profiling studies of L-CVD SnO₂ thin films,” *Appl. Surf. Sci.*, vol. 252, no. 21, pp. 7730–7733, 2006.
- [180] B. Drevillon, S. Kumar, P. Roca Cabarrocas, and J. M. Siefert, “In situ investigation of the optoelectronic properties of transparent conducting oxide/ amorphous silicon interfaces,” *Appl. Phys. Lett. J. Appl. Phys.*, vol. 54, no. 21, p. 2088, 1989.
- [181] V. M. Jiménez, J. A. Mejías, J. P. Espinós, and A. R. González-Elipe, “Interface effects for metal oxide thin films deposited on another metal oxide II. SnO₂ deposited on SiO₂,” *Surf. Sci.*, vol. 366, no. 3, pp. 545–555, 1996.
- [182] J. W. a Schüttauf, C. H. M. Van Der Werf, I. M. Kielen, W. G. J. H. M. Van Sark, J. K. Rath, and R. E. I. Schropp, “Improving the performance of amorphous and crystalline silicon heterojunction solar cells by monitoring surface passivation,” *J. Non. Cryst. Solids*, vol. 358, no. 17, pp. 2245–2248, 2012.
- [183] R. Edy, X. Huang, Y. Guo, J. Zhang, and J. Shi, “Influence of argon plasma on the deposition of Al₂O₃ film onto the PET surfaces by atomic layer deposition.,” *Nanoscale Res. Lett.*, vol. 8, no. 1, p. 79, 2013.
- [184] F. J. Himpsel, F. R. McFeely, A. Taleb-Ibrahimi, J. A. Yarmoff, and G. Hollinger, “Microscopic structure of the SiO₂/Si interface,” *Phys. Rev. B*, vol. 38, no. 9, pp. 6084–6096, 1988.
- [185] J. M. Hill, D. G. Royce, C. S. Fadley, L. F. Wagner, and F. J. Grunthaner, “Properties of oxidized silicon as determined by angular-dependent X-ray photoelectron spectroscopy,” *Chem. Phys. Lett.*, vol. 44, no. 2, pp. 225–231, 1976.
- [186] K. Joong Kim, K. T. Park, and J. W. Lee, “Thickness measurement of SiO₂ films thinner than 1 nm by X-ray photoelectron spectroscopy,” *Thin Solid Films*, vol. 500, no. 1–2, pp. 356–359, 2006.
- [187] I. Wagner, H. Stasiewski, B. Abeles, and W. A. Lanford, “Surface states in P- and B-doped amorphous hydrogenated silicon,” *Phys. Rev. B*, vol. 28, no. 12, pp. 7080–7086, 1983.
- [188] P. De Padova, M. Fanfoni, and R. Larciprete, “A synchrotron radiation photoemission study of the oxidation of tin,” *Surf. Sci.*, vol. 313, pp. 379–391, 1994.

- [189] R. Félix *et al.*, “Preparation and in-system study of SnCl₂ precursor layers: Towards vacuum-based synthesis of Pb-free perovskites,” *RSC Adv.*, vol. 8, no. 1, pp. 67–73, 2018.
- [190] S. Major, S. Kumar, M. Bhatnagar, and K. L. Chopra, “Effect of hydrogen plasma treatment on transparent conducting oxides,” *Appl. Phys. Lett.*, vol. 49, no. 7, pp. 394–396, 1986.
- [191] A. Klein *et al.*, “Surface potentials of magnetron sputtered transparent conducting oxides,” *Thin Solid Films*, vol. 518, no. 4, pp. 1197–1203, 2009.
- [192] L. Korte, R. Röbber, and C. Pettenkofer, “Direct determination of the band offset in atomic layer deposited ZnO/hydrogenated amorphous silicon heterojunctions from X-ray photoelectron spectroscopy valence band spectra,” *J. Appl. Phys.*, vol. 115, no. 20, p. 203715, 2014.
- [193] A. Imanishi, E. Tsuji, and Y. Nakato, “Dependence of the work function of TiO₂ (Rutile) on crystal faces, studied by a scanning auger microprobe,” *J. Phys. Chem. C*, vol. 111, no. 5, pp. 2128–2132, 2007.
- [194] L. Yang, B. Abeles, W. Eberhardt, H. Stasiewski, and D. Sondericker, “Photoemission spectroscopy of heterojunctions of hydrogenated amorphous silicon with silicon oxide and nitride,” *Physical review. B, Condensed matter*, vol. 39, no. 6, pp. 3801–3816, 1989.
- [195] M. Yamaguchi, K. H. Lee, K. Araki, and N. Kojima, “A review of recent progress in heterogeneous silicon tandem solar cells,” *J. Phys. D: Appl. Phys.*, vol. 51, no. 13, 2018.
- [196] M. Saliba *et al.*, “How to Make over 20% Efficient Perovskite Solar Cells in Regular (n-i-p) and Inverted (p-i-n) Architectures,” *Chem. Mater.*, vol. 30, no. 13, pp. 4193–4201, 2018.
- [197] M. a. Green, E. D. Dunlop, D. H. Levi, J. Hohl-Ebinger, M. Yoshita, and A. W. Y. Ho-Baillie, “Solar cell efficiency tables (version 54),” *Prog. Photovoltaics Res. Appl.*, vol. 27, no. 7, pp. 565–575, 2019.
- [198] M. Jošt *et al.*, “Textured interfaces in monolithic perovskite/silicon tandem solar cells: Advanced light management for improved efficiency and energy yield,” *Energy Environ. Sci.*, vol. 11, no. 12, pp. 3511–3523, 2018.
- [199] A. Al-Ashouri *et al.*, “Conformal monolayer contacts with lossless interfaces for perovskite single junction and monolithic tandem solar cells,” *Energy Environ. Sci.*, vol. 12, no. 11, pp. 3356–3369, 2019.
- [200] N. Phung and A. Abate, “The Impact of Nano- and Microstructure on the Stability of Perovskite Solar Cells,” *Small*, vol. 14, no. 46, pp. 1–11, 2018.
- [201] A. Abate, “Perovskite Solar Cells Go Lead Free,” *Joule*, vol. 1, no. 4, pp. 1–6, 2017.

- [202] A. B. Huang *et al.*, “Achieving high-performance planar perovskite solar cells with co-sputtered Co-doping NiO x hole transport layers by efficient extraction and enhanced mobility,” *J. Mater. Chem. C*, vol. 4, no. 46, pp. 10839–10846, 2016.
- [203] A. Magomedov *et al.*, “Self-Assembled Hole Transporting Monolayer for Highly Efficient Perovskite Solar Cells,” *Adv. Energy Mater.*, vol. 8, no. 32, 2018.
- [204] A. Fakharuddin, L. Schmidt-Mende, G. Garcia-Belmonte, R. Jose, and I. Mora-Sero, “Interfaces in Perovskite Solar Cells,” *Adv. Energy Mater.*, vol. 7, no. 22, p. 1700623, Nov. 2017.
- [205] K. Wojciechowski *et al.*, “C 60 as an Efficient n-Type Compact Layer in Perovskite Solar Cells,” *J. Phys. Chem. Lett.*, vol. 6, no. 12, pp. 2399–2405, Jun. 2015.
- [206] Q. Jiang *et al.*, “Enhanced electron extraction using SnO₂ for high-efficiency planar-structure HC(NH₂)₂ PbI₃-based perovskite solar cells,” *Nat. Energy*, vol. 2, no. 1, 2017.
- [207] M. F. Aygü *et al.*, “Influence of Fermi Level Alignment with Tin Oxide on the Hysteresis of Perovskite Solar Cells,” *ACS Appl. Mater. Interfaces*, vol. 10, p. 22, 2018.
- [208] J. H. Lee *et al.*, “Band Alignment Engineering between Planar SnO₂ and Halide Perovskites via Two-Step Annealing,” *J. Phys. Chem. Lett.*, vol. 10, no. 21, pp. 6545–6550, Nov. 2019.
- [209] Q. Dong *et al.*, “Improved SnO₂ Electron Transport Layers Solution-Deposited at Near Room Temperature for Rigid or Flexible Perovskite Solar Cells with High Efficiencies,” *Adv. Energy Mater.*, vol. 1900834, pp. 1–9, May 2019.
- [210] Y. Lee *et al.*, “Efficient Planar Perovskite Solar Cells Using Passivated Tin Oxide as an Electron Transport Layer,” *Adv. Sci.*, vol. 5, no. 6, pp. 1–6, 2018.
- [211] F. Lebreton, S. N. Abolmasov, F. Silva, and P. Roca I Cabarrocas, “In situ photoluminescence study of plasma-induced damage at the a-Si:H/c-Si interface,” *Appl. Phys. Lett.*, vol. 108, no. 5, 2016.
- [212] H. Tan *et al.*, “Efficient and stable solution-processed planar perovskite solar cells via contact passivation,” *Science (80-.)*, vol. 355, no. 6326, pp. 722–726, Feb. 2017.
- [213] X. Ren *et al.*, “Chlorine-modified SnO₂ electron transport layer for high-efficiency perovskite solar cells,” *InfoMat*, no. August, p. inf2.12059, Dec. 2019.
- [214] J. Y. Lim *et al.*, “Work function of MgO single crystals from ion-induced secondary electron emission coefficient,” *J. Appl. Phys.*, vol. 94, no. 1, pp. 764–769, 2003.
- [215] M. M. Sung, C. G. Kim, J. Kim, and Y. Kim, “Chemical beam deposition of MgO films on Si substrates using methylmagnesium tert-butoxide,” *Chem. Mater.*, vol. 14, no. 2, pp. 826–831, 2002.

- [216] W. Fan, P. R. Markworth, T. J. Marks, and R. P. H. Chang, "Growth of atomically flat homoepitaxial magnesium oxide thin films by metal-organic chemical vapor deposition," *Mater. Chem. Phys.*, vol. 70, no. 2, pp. 191–196, 2001.
- [217] M. Manin, S. Thollon, F. Emieux, G. Berthome, M. Pons, and H. Guillon, "Deposition of MgO thin film by liquid pulsed injection MOCVD," *Surf. Coatings Technol.*, vol. 200, no. 5–6, pp. 1424–1429, 2005.
- [218] W. B. Wang, Y. Yang, A. Yanguas-Gil, N. N. Chang, G. S. Girolami, and J. R. Abelson, "Highly conformal magnesium oxide thin films by low-temperature chemical vapor deposition from Mg(H₃BNMe₂BH₃)₂ and water," *Appl. Phys. Lett.*, vol. 102, no. 10, p. 101605, 2013.
- [219] B. B. Burton, D. N. Goldstein, and S. M. George, "Atomic layer deposition of MgO using bis(ethylcyclopentadienyl)magnesium and H₂O," *J. Phys. Chem. C*, vol. 113, no. 5, pp. 1939–1946, 2009.
- [220] Y. Kuang *et al.*, "Towards the implementation of atomic layer deposited In₂O₃:H in silicon heterojunction solar cells," *Sol. Energy Mater. Sol. Cells*, vol. 163, pp. 43–50, Apr. 2017.
- [221] J. T. Newberg *et al.*, "Autocatalytic surface hydroxylation of MgO(100) terrace sites observed under ambient conditions," *J. Phys. Chem. C*, vol. 115, no. 26, pp. 12864–12872, 2011.
- [222] M. Santamaria, F. Di Quarto, S. Zanna, and P. Marcus, "Initial surface film on magnesium metal: A characterization by X-ray photoelectron spectroscopy (XPS) and photocurrent spectroscopy (PCS)," *Electrochim. Acta*, vol. 53, no. 3, pp. 1314–1324, Dec. 2007.
- [223] V. Fournier, P. Marcus, and I. Olefjord, "Oxidation of magnesium," *Surf. Interface Anal.*, vol. 34, no. 1, pp. 494–497, 2002.
- [224] C. Leendertz, R. Stangl, T. F. Schulze, M. Schmidt, and L. Korte, "A recombination model for a-Si:H/c-Si heterostructures," *Phys. Status Solidi Curr. Top. Solid State Phys.*, vol. 7, no. 3–4, pp. 1005–1010, 2010.
- [225] X. Yang, P. Zheng, Q. Bi, and K. Weber, "Silicon heterojunction solar cells with electron selective TiO_x contact," *Sol. Energy Mater. Sol. Cells*, vol. 150, pp. 32–38, 2016.
- [226] X. Cheng, E. S. Marstein, H. Haug, C. C. You, and M. Di Sabatino, "Thermal stability of hydrogenated amorphous silicon passivation for p-type crystalline silicon," *Phys. Status Solidi Appl. Mater. Sci.*, vol. 213, no. 1, pp. 91–95, 2016.
- [227] H. Thoms, M. Epple, and A. Reller, "The thermal decomposition of magnesium alcoholates to magnesia (MgO): studies by IR and thermal analysis," *Solid State Ionics*, vol. 101–103, no. Part 1, pp. 79–84, 1997.

- [228] B. Brennan, S. McDonnell, and G. Hughes, "Photoemission studies of the initial interface formation of ultrathin MgO dielectric layers on the Si(111) surface," *Thin Solid Films*, vol. 518, no. 8, pp. 1980–1984, 2010.
- [229] A. D. Katnani and R. S. Bauer, "Commutativity and transitivity of GaAs-AlAs-Ge(100) band offsets," *Phys. Rev. B*, vol. 33, no. 2, pp. 1106–1109, Jan. 1986.
- [230] J. Hu, A. Nainani, Y. Sun, K. C. Saraswat, and H. S. Philip Wong, "Impact of fixed charge on metal-insulator-semiconductor barrier height reduction," *Appl. Phys. Lett.*, vol. 99, no. 25, pp. 252104–23702, 2011.
- [231] J. Kanicki, "Contact resistance to undoped and phosphorus-doped hydrogenated amorphous silicon films," *Appl. Phys. Lett.*, vol. 53, no. 20, pp. 1943–1945, 1988.
- [232] M. S. Haque, H. A. Naseem, and W. D. Brown, "Interaction of aluminum with hydrogenated amorphous silicon at low temperatures," *J. Appl. Phys.*, vol. 75, no. 8, pp. 3928–3935, 1994.
- [233] Y. Wan *et al.*, "A magnesium/amorphous silicon passivating contact for n-type crystalline silicon solar cells," *Appl. Phys. Lett.*, vol. 109, no. 11, p. 113901, 2016.
- [234] T. L. Barr, "An XPS study of Si as it occurs in adsorbents, catalysts, and thin films," *Appl. Surf. Sci.*, vol. 15, no. 1–4, pp. 1–35, 1983.
- [235] J. S. Corneille, J. W. He, and D. W. Goodman, "XPS characterization of ultra-thin MgO films on a Mo(100) surface," *Surf. Sci.*, vol. 306, no. 3, pp. 269–278, 1994.
- [236] Ç. Kiliç and A. Zunger, "N-type doping of oxides by hydrogen," *Appl. Phys. Lett.*, vol. 81, no. 1, pp. 73–75, 2002.
- [237] J. C. Stang *et al.*, "Aluminium metallisation for interdigitated back-contact silicon heterojunction solar cells," *Jpn. J. Appl. Phys.*, vol. 56, no. 8, p. 08MB22, 2017.
- [238] M. S. Haque, H. A. Naseem, and W. D. Brown, "Aluminum-induced degradation and failure mechanisms of a-Si:H solar cells," *Sol. Energy Mater. Sol. Cells*, vol. 41–42, pp. 543–555, 1996.
- [239] K. Yoshikawa *et al.*, "Exceeding conversion efficiency of 26% by heterojunction interdigitated back contact solar cell with thin film Si technology," *Sol. Energy Mater. Sol. Cells*, no. April, pp. 0–1, 2017.
- [240] A. Richter, J. Benick, F. Feldmann, A. Fell, M. Hermle, and S. W. Glunz, "n-Type Si solar cells with passivating electron contact: Identifying sources for efficiency limitations by wafer thickness and resistivity variation," *Sol. Energy Mater. Sol. Cells*, vol. 173, no. May, pp. 96–105, 2017.
- [241] S. Schäfer *et al.*, "26%-Efficient and 2 Cm Narrow Interdigitated Back Contact Silicon Solar Cells With Passivated Slits on Two Edges," *Sol. Energy Mater. Sol. Cells*, vol. 200, no. April, p. 110021, 2019.

- [242] D. Chen *et al.*, “24.58% total area efficiency of screen-printed, large area industrial silicon solar cells with the tunnel oxide passivated contacts (i-TOPCon) design,” *Sol. Energy Mater. Sol. Cells*, vol. 206, no. October 2019, pp. 1–8, 2020.
- [243] U. Römer *et al.*, “Ion implantation for poly-Si passivated back-junction back-contacted solar cells,” *IEEE J. Photovoltaics*, vol. 5, no. 2, pp. 507–514, 2015.
- [244] U. Römer *et al.*, “Recombination behavior and contact resistance of n+ and p+ polycrystalline Si/mono-crystalline Si junctions,” *Sol. Energy Mater. Sol. Cells*, vol. 131, pp. 85–91, 2014.
- [245] A. S. Kale *et al.*, “Understanding the charge transport mechanisms through ultrathin SiO_x layers in passivated contacts for high-efficiency silicon solar cells,” *Appl. Phys. Lett.*, vol. 114, no. 8, p. 83902, 2019.
- [246] R. Peibst *et al.*, “Working principle of carrier selective poly-Si/c-Si junctions: Is tunnelling the whole story?,” *Sol. Energy Mater. Sol. Cells*, vol. 158, pp. 60–67, 2016.
- [247] F. Feldmann, C. Reichel, R. Müller, and M. Hermle, “The application of poly-Si/SiO_x contacts as passivated top/rear contacts in Si solar cells,” *Sol. Energy Mater. Sol. Cells*, vol. 159, pp. 265–271, 2017.
- [248] T. Matsui, M. Bivour, P. Ndione, P. Hettich, and M. Hermle, “Investigation of atomic-layer-deposited TiO_x as selective electron and hole contacts to crystalline silicon,” *Energy Procedia*, vol. 124, pp. 628–634, 2017.
- [249] J. Ding, Y. Zhou, G. Dong, M. Liu, D. Yu, and F. Liu, “Solution-processed ZnO as the efficient passivation and electron selective layer of silicon solar cells,” *Prog. Photovoltaics Res. Appl.*, vol. 26, no. 12, pp. 974–980, 2018.
- [250] M. Liu *et al.*, “SnO₂/Mg combination electron selective transport layer for Si heterojunction solar cells,” *Sol. Energy Mater. Sol. Cells*, vol. 200, no. January, p. 109996, 2019.
- [251] Y. Wan *et al.*, “Tantalum Oxide Electron-Selective Heterocontacts for Silicon Photovoltaics and Photoelectrochemical Water Reduction,” *ACS Energy Lett.*, vol. 3, no. 1, pp. 125–131, 2018.
- [252] F. Wang *et al.*, “Silicon solar cells with bifacial metal oxides carrier selective layers,” *Nano Energy*, vol. 39, pp. 437–443, 2017.
- [253] M. T. Greiner, M. G. Helander, W. M. Tang, Z. Bin Wang, J. Qiu, and Z. H. Lu, “Universal energy-level alignment of molecules on metal oxides,” *Nat. Mater.*, vol. 11, no. 1, pp. 76–81, 2012.
- [254] F. Menchini *et al.*, “Application of NiO_x thin films as p-type emitter layer in heterojunction solar cells,” *Phys. Status Solidi Curr. Top. Solid State Phys.*, vol. 13, no. 10–12, pp. 1006–1010, 2016.

- [255] L. G. Gerling *et al.*, “Transition metal oxides as hole-selective contacts in silicon heterojunctions solar cells,” *Sol. Energy Mater. Sol. Cells*, vol. 145, pp. 109–115, 2016.
- [256] J. Bullock, D. Yan, A. Cuevas, Y. Wan, and C. Samundsett, “N- and p-typesilicon Solar Cells with Molybdenum Oxide Hole Contacts,” in *Energy Procedia*, 2015, vol. 77, pp. 446–450.
- [257] J. Geissbühler *et al.*, “22.5% Efficient Silicon Heterojunction Solar Cell With Molybdenum Oxide Hole Collector,” *Appl. Phys. Lett.*, vol. 107, no. 8, 2015.
- [258] D. Sacchetto *et al.*, “ITO/MoO_x/a-Si:H(i) Hole-Selective Contacts for Silicon Heterojunction Solar Cells: Degradation Mechanisms and Cell Integration,” *IEEE J. Photovoltaics*, vol. 7, no. 6, pp. 1584–1590, 2017.
- [259] M. A. Khilla, Z. M. Hanafi, B. S. Farag, and A. Abu-el Saud, “Transport properties of molybdenum trioxide and its suboxides,” *Thermochim. Acta*, vol. 54, no. 1–2, pp. 35–45, Apr. 1982.
- [260] S. Essig *et al.*, “Toward Annealing-Stable Molybdenum-Oxide-Based Hole-Selective Contacts For Silicon Photovoltaics,” *Sol. RRL*, vol. 2, no. 4, p. 1700227, 2018.
- [261] T. Zhang, C.-Y. Lee, B. Gong, S. Lim, S. Wenham, and B. Hoex, “*In situ* x-ray photoelectron emission analysis of the thermal stability of atomic layer deposited WO_x as hole-selective contacts for Si solar cells,” *J. Vac. Sci. Technol. A Vacuum, Surfaces, Film.*, vol. 36, no. 3, p. 031601, 2018.
- [262] M. Bivour, J. Temmler, F. Zahringer, S. Glunz, and M. Hermle, “High work function metal oxides for the hole contact of silicon solar Cells,” *Conf. Rec. IEEE Photovolt. Spec. Conf.*, vol. 2016-Novem, pp. 215–220, 2016.
- [263] B. Macco, M. F. J. Vos, N. F. W. Thissen, A. A. Bol, and W. M. M. Kessels, “Low-temperature atomic layer deposition of MoO_x for silicon heterojunction solar cells,” *Phys. status solidi - Rapid Res. Lett.*, vol. 9, no. 7, pp. 393–396, 2015.
- [264] T. Zhang, C.-Y. Lee, B. Gong, S. Lim, S. Wenham, and B. Hoex, “*In situ* x-ray photoelectron emission analysis of the thermal stability of atomic layer deposited WO_x as hole-selective contacts for Si solar cells,” *J. Vac. Sci. Technol. A Vacuum, Surfaces, Film.*, vol. 36, no. 3, p. 031601, 2018.
- [265] J. Ziegler *et al.*, “Plasma-enhanced atomic-layer-deposited MoO_x emitters for silicon heterojunction solar cells,” *Appl. Phys. A*, vol. 120, no. 3, pp. 811–816, 2015.
- [266] B. Macco, B. W. H. Van De Loo, J. Melskens, S. Smit, and W. M. M. E. Kessels, “Status and prospects for atomic layer Deposited metal oxide thin films in passivating contacts for c-Si photovoltaics,” *2017 IEEE 44th Photovolt. Spec. Conf. PVSC 2017*, pp. 1–6, 2017.
- [267] M. Schnabel, W. Nemeth, P. Stradins, D. L. Young, B. W. H. Van De Loo, and B. Macco, “Hydrogen passivation of poly-Si/SiO_x contacts for Si solar cells using Al₂O₃ studied with deuterium,” *Appl. Phys. Lett.*, vol. 112, no. 20, 2018.

- [268] L. E. Black, B. W. H. van de Loo, B. Macco, J. Melskens, W. J. H. Berghuis, and W. M. M. Kessels, “Explorative studies of novel silicon surface passivation materials: Considerations and lessons learned,” *Sol. Energy Mater. Sol. Cells*, vol. 188, no. February, pp. 182–189, 2018.
- [269] G. Dingemans, C. a. a. Van Helvoirt, D. Pierreux, W. Keuning, and W. M. M. Kessels, “Plasma-assisted ALD for the conformal deposition of SiO₂: Process, material and electronic properties,” *J. Electrochem. Soc.*, vol. 159, no. 3, 2012.
- [270] V. Zardetto *et al.*, “Atomic layer deposition for perovskite solar cells: research status, opportunities and challenges,” *Sustain. Energy Fuels*, vol. 1, no. 1, pp. 30–55, 2017.
- [271] Y. Wu *et al.*, “Highly compact TiO₂ layer for efficient hole-blocking in perovskite solar cells,” *Appl. Phys. Express*, vol. 7, no. 5, 2014.
- [272] C. Y. Chang, K. T. Lee, W. K. Huang, H. Y. Siao, and Y. C. Chang, “High-Performance, Air-Stable, Low-Temperature Processed Semitransparent Perovskite Solar Cells Enabled by Atomic Layer Deposition,” *Chem. Mater.*, vol. 27, no. 14, pp. 5122–5130, 2015.
- [273] Y. Kuang *et al.*, “Low-Temperature Plasma-Assisted Atomic-Layer-Deposited SnO₂ as an Electron Transport Layer in Planar Perovskite Solar Cells,” *ACS Appl. Mater. Interfaces*, vol. 10, no. 36, pp. 30367–30378, 2018.
- [274] P. Schulz *et al.*, “High-work-function molybdenum oxide hole extraction contacts in hybrid organic-inorganic perovskite solar cells,” *ACS Appl. Mater. Interfaces*, vol. 8, no. 46, pp. 31491–31499, 2016.
- [275] J. a. Raiford *et al.*, “Atomic layer deposition of vanadium oxide to reduce parasitic absorption and improve stability in n-i-p perovskite solar cells for tandems,” *Sustain. Energy Fuels*, vol. 3, no. 6, pp. 1517–1525, 2019.
- [276] S. Seo *et al.*, “An ultra-thin, un-doped NiO hole transporting layer of highly efficient (16.4%) organic-inorganic hybrid perovskite solar cells,” *Nanoscale*, vol. 8, no. 22, pp. 11403–11412, 2016.
- [277] T. S. Tripathi, J.-P. Niemelä, and M. Karppinen, “Atomic layer deposition of transparent semiconducting oxide CuCrO₂ thin films,” *J. Mater. Chem. C*, vol. 3, no. 32, pp. 8364–8371, 2015.
- [278] A. a. Istratov and E. R. Weber, “Physics of Copper in Silicon,” *J. Electrochem. Soc.*, vol. 149, no. 1, p. G21, 2002.
- [279] H. Wei *et al.*, “Enhanced charge collection with ultrathin AlO_x electron blocking layer for hole-transporting material-free perovskite solar cell,” *Phys. Chem. Chem. Phys.*, vol. 17, no. 7, pp. 4937–4944, 2015.
- [280] D. Koushik *et al.*, “High-efficiency humidity-stable planar perovskite solar cells based on atomic layer architecture,” *Energy Environ. Sci.*, vol. 10, no. 1, pp. 91–100, 2017.

- [281] M. Jaysankar *et al.*, “Perovskite-silicon tandem solar modules with optimised light harvesting,” *Energy Environ. Sci.*, vol. 11, no. 6, pp. 1489–1498, 2018.
- [282] E. Köhnen *et al.*, “Highly efficient monolithic perovskite silicon tandem solar cells: analyzing the influence of current mismatch on device performance,” *Sustain. Energy Fuels*, vol. 1, pp. 2017–2018, 2019.
- [283] M. Rienäcker *et al.*, “Back-contacted bottom cells with three terminals: Maximizing power extraction from current-mismatched tandem cells,” *Prog. Photovoltaics Res. Appl.*, vol. 27, no. 5, pp. 410–423, 2019.
- [284] J. P. Niemelä *et al.*, “Rear-emitter silicon heterojunction solar cells with atomic layer deposited ZnO:Al serving as an alternative transparent conducting oxide to In₂O₃:Sn,” *Sol. Energy Mater. Sol. Cells*, vol. 200, no. April, p. 109953, 2019.
- [285] B. Conings *et al.*, “Intrinsic Thermal Instability of Methylammonium Lead Trihalide Perovskite,” *Adv. Energy Mater.*, vol. 5, no. 15, pp. 1–8, 2015.
- [286] A. F. Palmstrom *et al.*, “Interfacial Effects of Tin Oxide Atomic Layer Deposition in Metal Halide Perovskite Photovoltaics,” *Adv. Energy Mater.*, vol. 8, no. 23, pp. 1–10, 2018.